Starvation in Oscillating Rolling Element Bearings

Von der Fakultät für Maschinenbau

der Gottfried Wilhelm Leibniz Universität Hannover

zur Erlangung des akademischen Grades

Doktor-Ingenieur

Dr.-Ing.

genehmigte Dissertation

von

Sebastian Wandel, M.Sc.

2024

Abstract

Oscillating rolling element bearings are part of a wide range of industrial applications. In addition to applications in which the oscillations occur as unwanted vibrations, in other applications they are used intentionally. One application that has gained particular importance in recent times is the use of rotor blade bearings in wind turbines. New control concepts such as individual pitch control (IPC) expose them to a high number of oscillations under varying operating parameters. Continuously rotating bearings are well understood in most cases and can usually be operated under lubrication conditions that avoid early bearing failure due to wear. In oscillating bearings, especially under grease lubrication, the lubrication mechanisms are insufficiently understood, so early bearing damage due to starvation and resulting wear phenomena such as false brinelling cannot be predicted. The present work addresses this point and investigates the lubrication mechanisms in oscillating rolling contacts by means of component tests on angular contact ball bearings of type 7208 and model tests on an optical EHL tribometer. The focus of these investigations is primarily on the influence of the base oil re-flow as well as on the influence of the rolling bearing cage on the lubricant supply to the oscillating contact. Based on the identified lubrication mechanisms, a starvation model is proposed, which allows to assess, based on the operating and lubricant parameters, whether the bearing is at risk of early damage due to starvation. This model is validated and discussed on the basis of component tests. These tests are executed in the frequency range of $f = 0.2 - 5\,\text{Hz}$ and small oscillation angles $(2-60°)$ under contact pressures of $p_{\max} = 1.5-2.5\,\text{GPa}$. In general, the oscillation angles are small enough that the rolling element pitch is not exceeded, but large enough that $\frac{x}{2b} > 1$ applies to the amplitude ratio. Smallest vibrations, which could lead to standstill marks, are therefore not examined.

Kurzfassung

Oszillierende Wälzlager sind Teil eines breiten Spektrums industrieller Anwendungen. Neben Anwendungen in denen Oszillationen als unerwünschte Vibrationen auftreten, sind sie in anderen Anwendungen funktionsrelevant. Besonders der Einsatz von Rotorblattlagern in Windenergieanlagen hat in letzter Zeit an Bedeutung gewonnen. Durch neue Regelungskonzepte wie *Individual Pitch Control* (IPC) sind die Lager einer hohen Anzahl von Oszillationen bei variierenden Betriebsparametern ausgesetzt. In kontinuierlich rotierender Anwendung ist der Einsatz von Wälzlagern tiefgehend erforscht, sodass diese in der Regel bei Schmierungsbedingungen betrieben werden können, unter denen ein frühzeitiger Ausfall aufgrund von Verschleiß unwahrscheinlich ist. In oszillierenden Lagern, insbesondere unter Fettschmierung, sind die Schmierungsmechanismen nur unzureichend verstanden, sodass frühzeitige Lagerschäden durch Mangelschmierung und daraus resultierende Verschleißerscheinungen wie *False Brinelling* nicht vorhergesagt werden können. Die vorliegende Arbeit setzt an diesem Punkt an. Die Schmierungsmechanismen in oszillierenden Wälzkontakten werden anhand von Bauteilversuchen an Schrägkugellagern des Typs 7208 und Modellversuchen auf einem optischen EHL-Tribometer analysiert. Der Fokus der Untersuchungen liegt auf dem Einfluss des Grundölrückflusses sowie der Wälzkörper-Käfig-Interaktion auf die Schmierstoffversorgung des Kontaktes. Auf Grundlage der identifizierten Schmierungsmechanismen wird ein Mangelschmierungsmodell entwickelt, das es erlaubt, anhand der Betriebs- und Schmierstoffparameter zu beurteilen, ob das Lager Gefahr läuft, frühzeitig Schaden aufgrund von Mangelschmierung zu nehmen. Das Modell wird anhand von Bauteilversuchen validiert und diskutiert. Die Versuche werden im Frequenzbereich von $f = 0.2 - 5\,\text{Hz}$ und kleinen Oszillationswinkeln ($2 - 60°$) unter maximalen Kontaktpressungen von $p_{\max} = 1.5 - 2.5\,\text{GPa}$ durchgeführt. In der Regel sind die Oszillationswinkel klein genug, sodass die Wälzkörperteilung nicht überschritten wird, jedoch so groß, dass das Amplitudenverhältnis kleiner eins ist ($\frac{x}{2b} > 1$). Kleinste Schwingungen, die zu Stillstandsmarkierungen führen könnten, werden nicht untersucht.

Acknowledgements

Special thanks go to my colleagues from other research institutes, whose collaboration in projects and scientific publications has added substantial value to this work. Particularly noteworthy are Prof. Dr. Johan Leckner, Roman de la Presilla, Arne Bartschat, Dr. Markus Grebe, and Prof. Dr. Sergei Glavatskih.

Finally, I thank my family for their unwavering support, without which I would not have reached this point. A special thanks to my girlfriend, Charlotte Wiemann, who supported me daily during my time as a doctoral candidate and stood by me during challenging times.

Sebastian Wandel
Hannover, December 2023

Contents

List of Figures

List of Tables

Nomenclature

A	Contact Area	m^2
a	Long Hertzian Half Axis	m
b	Short Hertzian Half Axis	m
d	Diameter	m
d'	Diameter after Deformation	m
E	Young's Modulus	Pa
E'	Equivalent Young's Modulus	Pa
E_d	Dissipated Energy	J
e	Amplitude Ratio $e = x/2b$	-
F_{diff}	Friction due to Relative Motion	N
F_{roll}	Hydrodynamic Rolling Friction	N
G	Dimensionless Material Parameter	-
h	Film thickness	m
h_c	Central Film Thickness	m
I	Moment of Inertia	$Kg{\cdot}m^2$
I_i	Intensity	$kg{\cdot}s^{-3}$
i	Transmission Ratio	-
k	Ellipticity Parameter	-
$\bar{k}$	Approximated Ellipticity Parameter	-
k_p	Permeability	m^2
N	Cycle Number	-
N_u	Uninterrupted Base Oscillations Cycles	-
O_{sr}	Oil Separation Rate	-
P	Dissipated Friction Power	J/s
p	Pressure	N/m^2
Q	Normal Rolling Element Load	N
r	Radius	m
r'	Radius after Deformation	m
S_N	Starvation Number	-
T	Torque	Nm
t	time	s

U	Dimensionless Speed Parameter	-
u	Circumferential Speed	m/s
u_e	Entrainment Speed	m/s
u_f	Flow Velocity	m/s
V	Volume	m^3
v	Relative Speed	m/s
W	Dimensionless Load Parameter	-
W_1	Carrier Signal	-
W_2	Signal	-
x	Distance travelled during Oscillation	m
Z	Number of Rolling Elements	-
α	Contact Angle	rad
α_p	Pressure Viscosity Coefficient	m^2/N
β	Tilting Angle of ω_{re}	rad
γ	Angle of Rotation of the Rolling Element	rad
$\gamma_{l,Im}$	Rolling Element/Cage Immersion Angle	rad
δ	Deformation	m
η_0	Dynamic Base Oil Viscosity	Pa·s
θ_e	Angle of Incidence	rad
θ_l	Oscillation Angle of Lubrication Cycle	rad
$\theta_{overlap}$	Overlapping Angle of Adjacent Contact Areas	rad
θ_s	Contact Angle Solid/Liquid	-
ϑ	Temperature	C°
κ	Osculation	-
κ_d	Damping Constant	-
λ_i	Wave Length	m
μ	Coefficient of Friction	-
ν	Poisson's Ratio	-
ρ	Curvature	1/m
ρ_d	Density	Kg/m^3
σ_s	Surface Tension	N/m
τ	Shear Stress	N/m^2
ϕ_{sep}	Pitch Angle Between Adjacent Rolling Elements	rad
ϕ_0	Phase Shift	rad
ψ	Angle in Crank/Lever Calculation	rad
Ω	Rotational Speed in Space Fixed System	rad/s
ω	Rotational Speed in Cage Fixed System	rad/s
$\mathcal{E}$	Elliptical Integral of Second Order	-
$\bar{\mathcal{E}}$	Approximated Elliptical Integral of Second Order	-

$\mathcal{F}$	Elliptical Integral of First Order	-
$\bar{\mathcal{F}}$	Approximated Elliptical Integral of Second Order	-

Indexes

acc	Acceleration
b	Base Cycle
c	Cage/Central
ch	Characteristic
diff	Relative Motion
eq	Equivalent
ff	Fully Flooded
fric	Friction
g	Green
Hertz	Hertzian
i	Inner Ring
ir	Inner Raceway
max	Maximum
o	Outer Ring
or	Outer Raceway
p	Pitch
r	Red
re	Rolling Element
red	Reduced
res	Resulting
spin	Rotation Around The Axis Perpendicular to the Contact
wear	Wear
0	Nominal

Abbreviations

CAD	Computer-Aided Design
CCD	Charge-Coupled Device
Ca	Calcium
DIIM	Dichromatic Interference Intensity Modulation
EHL	Elasto-Hydrodynamic Lubrication
EST	Ester
FC	Full Rolling Element Set With Cage
FNC	Full Rolling Element Set Without Cage
HC	Half Rolling Element Set With Cage
HNC	Half Rolling Element Set Without Cage
IPC	Individual Pitch Control
Li	Lithium
LiX	Lithium-Complex
MoDTC	Molybdenum Dialkyl Dithiocarbamate
OEM	Original Equipment Manufacturer
PAO	Polyalphaolefin
ZDDP	Zinc Dialkyl Dithiophosphate
ZrO_2	Zirconium Dioxide

Part I.

Introduction

As early as 1100 BC, the Assyrians discovered that rolling elements under their load carriages were an effective means of significantly reducing frictional resistance to carriages sliding on the ground. Later in 1452-1519 AD, Leonardo Da Vinci included the principle of rolling elements in his Codex Madrid and used it to develop concepts of rolling element bearings that are very similar in form to the rolling bearings used today [91]. However, it took until the Industrial Revolution (1760-1840 AD) for the use and development of rolling bearings to receive a huge boost and lead to rolling bearings in many different designs being one of the most widely used machine elements today. In most traditional applications, rolling bearings are operated reliably under continuous rotation over a long operating life. However, when the bearings are subjected to oscillating motion early failure of the bearing can be the consequence.

The history of investigations into oscillating bearings goes back to 1937 when Almen was describing the wear phenomenon False Brinelling in automotive wheel bearings due to vibrations during the shipping of cars and was carrying out the first research on that topic [3]. In the study conducted by Almen, it was observed that the wheel bearings of the stationary vehicles suffered damage as a result of inadvertent vibrations generated by the diesel engine of the transport vessel. Unintended vibrations occur in all industrial applications and can lead to damage, especially in stationary rolling element bearings. Wind turbines subjected to vibrations due to elastic deformation of the components caused by wind excitation while at a standstill can result in damage to the rolling element bearings within the drive train.

In various modern industrial applications, rolling element bearings are also deliberately subjected to smaller oscillating movements. Examples include bearings found in robotic arms, azimuth bearings utilized in applications like construction cranes, and rotor blade bearings within wind turbines that enable power control by rotating the rotor blades around their longitudinal axis. The implementation of advanced control concepts, like Individual Pitch Control (IPC), in wind turbines has led to a substantial rise in pitch activity [12]. As a result, the issue of wear in oscillating bearings has become an important area of research, as evidenced by the increasing number of recent publications [90].

Over 90 % of rolling element bearings are grease lubricated [73]. The global efforts to utilize rolling bearings in an environmentally sustainable manner will persist, driving the trend towards minimizing the usage of lubricants

in the future. In combination with high cost efficiency and low maintenance, lifetime lubrication with grease is key for the future. But especially in grease-lubricated rolling element bearings, starvation phenomena play a crucial role. Starvation of lubricant becomes particularly critical in situations where prevailing oscillations exhibit small amplitudes. These oscillations impede the adequate redistribution of lubricant within the bearing, resulting in insufficient lubrication of the contact points and subsequently leading to wear.

Wear damage in rolling element bearings caused by oscillations can be critical for different reasons depending on the application. In precision mechanical applications, where achieving high positioning accuracy and precise predictability of frictional torque during adjustment movements is crucial, wear can significantly compromise the system's performance. In space applications, for example, where weight-saving measures prohibit regular bearing maintenance and the use of oversized motors, torque increments resulting from wear can lead to the bearing becoming blocked and subsequently cause a loss of function in the system.

Even in more robust applications where torque increments can be offset by increased motor power and positioning accuracy is less critical, initial wear damage in rolling element bearings can still result in secondary damage, such as fatigue, leading to a substantial reduction in the bearing's service life.

Preventing wear damage in grease lubricated oscillating rolling element bearings holds significant importance for numerous industrial applications. This motivation forms the basis of the research focus in this thesis, which revolves around two overarching questions:

- Which mechanisms lead to wear initiation in grease lubricated oscillating rolling element bearings?

- How to prevent wear initiation in grease lubricated oscillating rolling element bearings?

Part II.

Contents

3.   State of the art

This chapter first deals with the basics of rolling element bearings, in particular angular contact ball bearings, as this design is used in the experimental part of this thesis. Following that, the chapter delves into the field of tribology, with a specific focus on grease lubrication of rolling bearings. Each topic is explained in principle to provide a comprehensive understanding. Finally, the last chapter brings together the previous sections, contextualizes the information, and presents the current research findings in the realm of oscillating grease-lubricated rolling element bearings.

3.1.   Bearing Kinematics

The primary purpose of a rolling element bearing is to facilitate relative movement between two components, such as a shaft and a housing, with minimal resistance. The minimisation of resistance is achieved through rolling motion of the rolling elements, which generally causes less frictional losses compared to pure sliding movement. In the following, the kinematic conditions of the rolling element raceway system are explained on the basis of a specific design of a rolling element bearing, the angular contact ball bearing. As the name suggests, angular contact ball bearings belong to the group of ball bearings. In contrast to deep grove ball bearings, angular contact ball bearings have a contact angle α between the normal to the bearing's axis of rotation and the connecting line between the contact points of the rolling element and the raceway and the rolling element center point, which is not equal to zero in the unloaded state. They are available in both single-row and double-row designs. Single-row angular contact ball bearings can support radial loads as well as axial loads in one direction.

For the interpretation of the experimental results in this paper, it is necessary to understand the kinematics of an angular contact ball bearing. In the tests

carried out here, the bearing is operated with a stationary outer ring and a moving inner ring, which is why the following derivation of the kinematics is carried out for this case. The kinematics in the angular contact ball bearing result from the geometrical conditions in the ball-raceway system. Figure 3.1 provides a schematic representation of the geometrical parameters and the resultant velocity components.
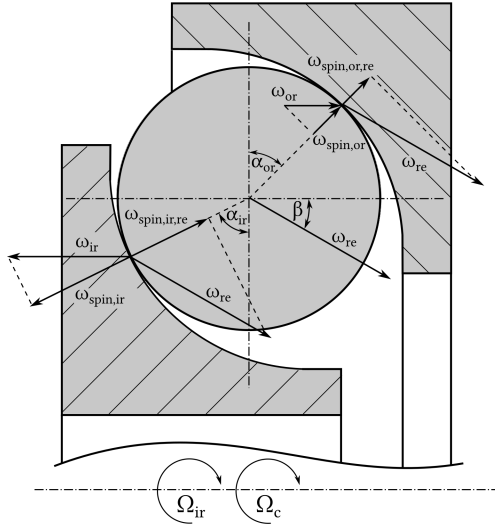
Figure 3.1.: Geometric parameters and speed vectors in an angular contact ball bearing.

The essential geometric parameters include the inner and outer raceway diameters d_{ir} and d_{or}, the rolling element diameter d_{re}, and the contact angle α. The contact angle is formed between the straight line connecting the contact points on the raceways and the perpendicular to the bearing axis of rotation passing through the center of the rolling element. For the stationary case, the contact angles on the inner and outer ring are equal $\alpha = \alpha_{ir} = \alpha_{or}$. For high rotational speeds, they are unequal $\alpha_{ir} \neq \alpha_{or}$.

The inner ring rotates at a speed of Ω_{ir} in the global coordinate system or ω_{ir} in the cage-relative system. It is assumed that the circumferential speeds u of the raceway and the rolling element are the same in the contact points $u_{ir} = u_{ir,re}$, $u_{or} = u_{or,re}$. The resulting rotational speed of the rolling element

set and the cage is denoted by Ω_c. The rolling element rotates at a speed of ω_{re} around the resulting axis of rotation, which is tilted at an angle β with respect to the plane parallel to the bearing rotation axis and passing through the center of the rolling element.

$$\omega_{re} = \frac{-\Omega_{ir}}{d_{ir} \cdot \left[\frac{\cos\alpha_{ir} - \beta}{d_{p'} - d_{re}\cdot\cos\alpha_{ir}} + \frac{\cos\alpha_{or} - \beta}{d_{p'} + d_{re}\cdot\cos\alpha_{or}} \right]} \tag{3.1}$$

$$\Omega_c = \frac{\Omega_{ir}}{1 + \left(\frac{d_{p'} + d_{re}\cdot\cos\alpha_{or}}{d_{p'} - d_{re}\cdot\cos\alpha_{ir}} \right) \cdot \frac{\cos\alpha_{ir} - \beta}{\cos\alpha_{or} - \beta}} \tag{3.2}$$

$$\Delta\omega_{spin,ir} = \omega_{ir} \cdot \sin\alpha_{ir} - \omega_{re} \cdot \sin\alpha_{ir} - \beta \tag{3.3}$$

$$\Delta\omega_{spin,or} = -\omega_{or} \cdot \sin\alpha_{or} + \omega_{re} \cdot \sin\alpha_{or} - \beta \tag{3.4}$$

To be able to determine the angle β, there is a well-known simplification according to Jones [57]. The hypothesis assumes that the contact which has a higher resistance against spin does not allow any relative motion by spin causing the relativ spin motion to be entirely concentrated on the other contact. At low velocities, the inner ring contact is usually the guiding or in other words controlling contact due to the longer contact ellipse. For the case of a controlling inner ring contact and for the case of a controlling outer ring contact, following simplifications are used to calculate the angle β: For inner race control

$$\beta = \arctan\left(\frac{d_{p'} \cdot \sin\alpha_{ir}}{d_{p'} \cdot \cos\alpha_{ir} - d_{re}} \right) \tag{3.5}$$

For outer race control

$$\beta = \arctan\left(\frac{d_{p'} \cdot \sin\alpha_{or}}{d_{p'} \cdot \cos\alpha_{or} + d_{re}} \right) \tag{3.6}$$

With $d_{p'}$ being the pitch diameter after deformation.

To assess whether the inner ring or outer ring contact is guiding, Hamrock considers the torque T_{spin} necessary to induce spinning, [40]:

$$T_{\text{spin}} = \frac{3}{8} \cdot \mu \cdot Q \cdot a \cdot \bar{\mathcal{E}} \qquad (3.7)$$

Outer-race control is present when the required torque for spin at the outer ring contact $T_{\text{spin,or}}$ is greater or equal than the torque at the inner ring contact $T_{\text{spin,ir}}$ ($T_{\text{spin,or}} \geq T_{\text{spin,ir}}$). Conversely, if $T_{\text{spin,or}} < T_{\text{spin,ir}}$, inner-race control is present. The aforementioned equations enable a simplified calculation of the kinematics in an angular contact ball bearing given the angular velocity of the inner ring and the geometric parameters. An alternative approach to determine the resulting rotational axis β of the rolling element is by employing the principle of virtual work and minimizing the dissipated frictional power P in the rolling element-raceway contacts. This method seeks to find the angle β for which the sum of the frictional power at the inner ring contact $P_{\text{ir}}(\beta)$ and outer ring contact $P_{\text{or}}(\beta)$ is minimized:

$$\beta = \arg\min P(\hat{\beta}) = \arg\min \left(P_{\text{ir}}(\hat{\beta}) + P_{\text{or}}(\hat{\beta})\right) \qquad (3.8)$$

This method aligns with the simplified approach proposed by Jones when assuming either inner or outer race control. The procedure for calculating the frictional power is elaborated in Section 3.2.4.

3.2. Contact Mechanics

This section aims to provide a detailed description of the contact mechanics in oscillating rolling bearings. It begins by examining the steady-state scenario for a continuously rotating bearing. Emphasis will be placed on a more in-depth discussion of the numerical calculation of slip ratios, as they serve as essential inputs for torque calculations within this thesis. Subsequently, the contact mechanics in the transient case, especially in the range of small oscillation angles during the transition from partial sliding to fully developed rolling, will be discussed in more detail.

3.2.1. Hᴇʀᴛzian Theory

In the loaded contact between the rolling element and raceway of an angular contact ball bearing, an elliptical contact area is formed due to the elastic deformation of the contact partners under a normal load Q. When dealing with the contact of two non-conforming elliptical contact partners, an analytical solution was provided by Hᴇʀᴛz in 1881 [49]. Hᴇʀᴛz assumes the contact of two linearly elastic half-spaces with smooth surfaces and homogeneous material properties. Furthermore, the dimensions of the contact area should be small compared to the dimensions of the contact partners and the relative contact radii. Under these assumptions, the Hᴇʀᴛzian contact area can be expressed as a function of the lengths of the semi-axes of the contact ellipse.
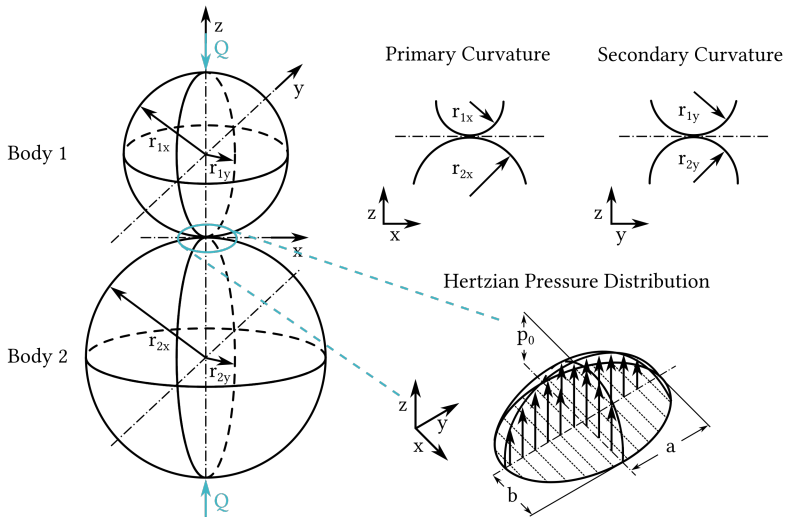
Figure 3.2.: Schematic of the Hᴇʀᴛzian contact between two ellipsoids

$$A = \pi ab \tag{3.9}$$

The semi-axis lengths a and b and the ellipticity parameter k are determined using the following equations:

$$a = \sqrt[3]{\frac{6k\mathcal{E}Q}{\pi \sum \rho E'}} \tag{3.10}$$

$$b = \sqrt[3]{\frac{6\mathcal{E}Q}{\pi k \sum \rho E'}} \tag{3.11}$$

$$k = \frac{a}{b} \tag{3.12}$$

For the calculation of the parameters, the normal load Q, the curvature of the bodies $\sum \rho$, the equivalent Young's modulus and the solution of the elliptic integrals $\mathcal{E}$ and $\mathcal{F}$ are required.

The equivalent Young's modulus is composed of the Young's moduli and the Poisson's ratios of the materials of the contact partners:

$$\frac{1}{E'} = \frac{1}{2}\left(\frac{1-v_1^2}{E_1} + \frac{1-v_2^2}{E_2}\right) \tag{3.13}$$

The curvature of the body is defined as follows:

$$\sum \rho = \frac{1}{R} = \frac{1}{R_x} + \frac{1}{R_y} = \frac{1}{r_{1x}} + \frac{1}{r_{2x}} + \frac{1}{r_{1y}} + \frac{1}{r_{2y}} \tag{3.14}$$

Due to the time-consuming nature of solving elliptic integrals, various approaches have been proposed to approximate their solutions. Brewe and Hamrock have proposed the following fits $\bar{k}$, $\bar{\mathcal{E}}$ and $\bar{\mathcal{F}}$ for k, $\mathcal{E}$ and $\mathcal{F}$, respectively [14].

$$\bar{k} = 1.0339 \cdot \left(\frac{R_y}{R_x}\right)^{0.6360} \tag{3.15}$$

$$\bar{\mathcal{E}} = 1.0003 + \frac{0.5968}{R_y/R_x} \tag{3.16}$$

$$\bar{\mathcal{F}} = 1.5277 + 0.6023 \cdot \ln\frac{R_y}{R_x} \tag{3.17}$$

These parameters can then be used to calculate the mutual approach of the contacting bodies:

$$\delta = \mathcal{F} \sqrt[3]{\frac{9 \sum \rho}{2\mathcal{E}} \cdot \left(\frac{Q}{\pi k E'}\right)^2}$$

(3.18)

The pressure distribution for each point in the contact area can also be determined:

$$p(x, y) = p_0 \cdot \sqrt{1 - \left(\frac{x}{a}\right)^2 - \left(\frac{y}{b}\right)^2}$$

(3.19)

Here, the nominal pressure p_0 is defined as:

$$p_0 = \bar{p} = \frac{Q}{A_{\text{Hertz}}} = \frac{Q}{\pi a b}$$

(3.20)

The maximum contact pressure $p_{\max}$ can be calculated as follows:

$$p_{\text{Hertz}} = p_{\max} = \frac{3}{2} \cdot p_0$$

(3.21)

3.2.2. Slip Between Contacting Surfaces

In angular contact ball bearings, a relative movement between the surfaces of the rolling element and the bearing raceway occurs under load due to the geometric conditions and the elastic deformation of the contact partners, which is referred to as slip. The total slip in the contact between rolling element and raceway in an angular contact ball bearing is composed of three components which are explained in more detail below. The statements and calculations in the following paragraphs pertain to the steady state case of fully developed rolling.

Heathcote Slip

In loaded ball bearings, the contact partners come into contact in a curved ellipse due to elastic deformation. Pure rolling along the contact ellipse is theoretically only possible in two bands with the same radius to the rolling

element's rolling axis. This effect is called HEATHCOTE effect. Figure 3.3 illustrates an example of a radial ball bearing with a contact angle $\alpha = 0$ [47]. By examining the relative speed along the centerline of the contact ellipse, it becomes apparent that only at two points symmetric to the y-axis, there is no relative speed. Between these points, slip occurs as the rolling element moves ahead of the raceway, whereas outside these points, the rolling element lags behind the raceway. The slip resulting from this effect is termed Heathcote slip.

Approximate formulas are available to calculate the position of the lines of pure rolling. One simple approximation, proposed by BISSON, places the lines at a distance a^* from the center of the contact [10].

$$a^* = 0.347 \cdot a \tag{3.22}$$

The z-position of the points on the undeformed surface of the rolling element and raceway can be described by the following formulas:

$$z_{\mathrm{re}}(x, y) = \frac{x^2}{d_{\mathrm{re}}} + \frac{y^2}{d_{\mathrm{re}}} \tag{3.23}$$

$$z_{\mathrm{ir}}(x, y) = \frac{x^2}{2 \cdot d_{\mathrm{re}} \cdot \kappa_{\mathrm{ir}}} + \frac{y^2}{d_{\mathrm{p}} - d_{\mathrm{re}}} \tag{3.24}$$

$$z_{\mathrm{or}}(x, y) = \frac{x^2}{-2 \cdot d_{\mathrm{re}} \cdot \kappa_{\mathrm{or}}} + \frac{y^2}{-d_{\mathrm{p}} - d_{\mathrm{re}}} \tag{3.25}$$

with κ being the osculation between rolling element and raceway. The displacement in the z-direction due to the elastic deformation of the bodies can be described using the BOUSSINESQ integral [39].

$$\delta(x, y) = \frac{1 - v^2}{\pi E} \cdot \iint_A \frac{p(x', y')}{\sqrt{(x - x')^2 + (y - y')^2}} \, \mathrm{d}x \, \mathrm{d}y \tag{3.26}$$

From this, the resulting radii r_{re} and r_{ir} with which each point on the deformed surface rotates about the axis of rotation can be calculated:

$$r_{\text{re}'}(x, y) = \frac{d_{\text{re}}}{2} - z_{\text{re}}(x, y) - \delta_{\text{re}}(x, y) \tag{3.27}$$

$$r_{\text{ir}'}(x, y) = \frac{d_{\text{p}} - d_{\text{re}}}{2} + z_{\text{ir}}(x, y) - \delta_{\text{ir}}(x, y) \tag{3.28}$$

$$r_{\text{or}'}(x, y) = \frac{d_{\text{p}} + d_{\text{re}}}{2} + z_{\text{or}}(x, y) - \delta_{\text{or}}(x, y) \tag{3.29}$$

The relative speed of each point within the contact zone can be expressed as the difference between the respective surface speeds, which can be calculated using the angular velocities and the radii of the deformed surfaces.

$$\Delta v_{\text{ir}}(x, y) = r_{\text{re}'}(x, y) \cdot \omega_{\text{re}} + r_{\text{ir}'}(x, y) \cdot \omega_{\text{ir}}' \tag{3.30}$$

$$\Delta v_{\text{or}}(x, y) = r_{\text{re}'}(x, y) \cdot \omega_{\text{re}} + r_{\text{or}'}(x, y) \cdot \omega_{\text{c}} \tag{3.31}$$
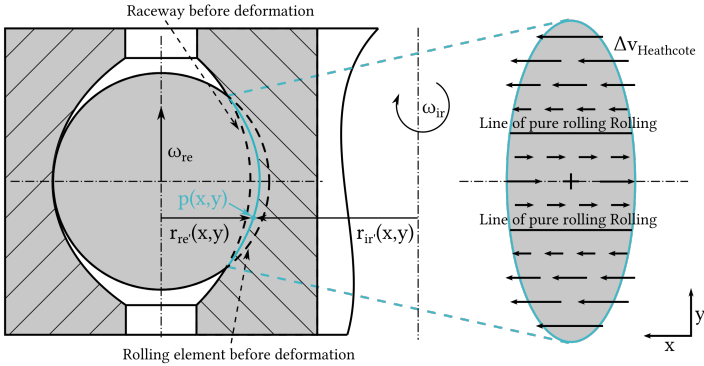
Figure 3.3.: Illustration of the Heathcote-slip for a ball bearing with contact angle $\alpha = 0$.

Spin Slip

When the contact angle α in a ball bearing is not zero, a spin component ω_{spin} arises, with an axis coinciding with the contact normal. It can be calculated

according to equation 3.32. This spin component results in a relative speed between the rolling element and the raceway, the magnitude of which depends on the distance to the center of the contact surface. Figure 3.4 shows a schematic of the relative speed components $\vec{v}_{\text{spin}}$ resulting from ω_{spin}. The spin, as well as the Heathcote component of the slip are inseparably superimposed.
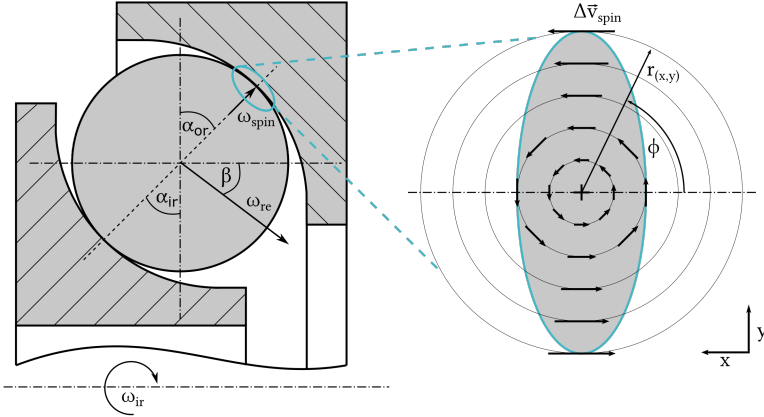
Figure 3.4.: Illustration of the slip component due to spin in a ball bearing with a contact angle $\alpha \neq 0$.

$$\Delta\vec{v}_{\text{spin}} = \begin{pmatrix} \Delta v_{\text{spin,x}} \\ \Delta v_{\text{spin,y}} \end{pmatrix} = \begin{pmatrix} -\Delta\omega_{\text{spin}} \cdot r(x,y) \cdot \sin(\phi) \\ \Delta\omega_{\text{spin}} \cdot r(x,y) \cdot \cos(\phi) \end{pmatrix} \qquad (3.32)$$

Reynolds Slip

Slip can also arise in the rolling contact due to different Young's moduli of the contact partners, as these materials deform differently under the acting tangential stresses. This occurs because the contact partners experience varying degrees of deformation under the tangential stresses. However, in the bearings studied within this work, this mechanism is not of significant importance, as the Young's moduli of the contact partners do not significantly differ.

During the operation of an angular contact ball bearing, the mentioned slip components are inevitably superimposed. Slip in the rolling element-raceway

contact is one of the main contributors to the torque required to rotate the bearing, especially in highly loaded rolling bearings. Additionally, it is a significant cause of wear between the contact partners. The torque calculation and tribological processes in contact will be discussed in the next chapters.

3.2.3. EHL Contacts

In a lubricated rolling contact, the lubricant adhering to the contact partners is drawn into a converging gap. This causes hydrodynamic pressure build-up, leading to the formation of a load-carrying lubricant film between the contact partners. In the case of a non-conforming rolling bearing contact, high pressures occur in the contact, resulting in elastic deformation of the surfaces of the contact partners. Additionally, the pressure causes a significant change in the viscosity of the lubricant. This regime is referred to as piezoviscous elastic, according to Johnson [55], and is known as full elastohydrodynamic lubrication (EHL). The pressure distribution for a given gap geometry in the contact can be approximated by the Reynolds equation [92]:

$$\frac{\partial}{\partial x}\left(h^3\frac{\partial p}{\partial x}\right) + \frac{\partial}{\partial y}\left(h^3\frac{\partial p}{\partial y}\right) = 6\eta(u_1 + u_2)\frac{\partial h}{\partial x} + 12\eta\frac{\partial h}{\partial t} \tag{3.33}$$

To fully solve the EHL contact problem, the local deformations, the lubricant film thickness equation, and the force balance equation must also be considered. The local deformations can be calculated according to Boussinesq, see Equation 3.26. The equation for the lubricant film thickness considering the local deformation can be written as [74]:

$$h(x, y) = h_0 + \frac{x^2}{2R_x} + \frac{y^2}{2R_y} + \delta(x, y) \tag{3.34}$$

The mutual distance h_0 can be calculated using the force balance equation:

$$m\frac{\partial h_0}{\partial t^2} + \iint_S p(x, y)\,dx\,dy = F(t) \tag{3.35}$$

The complete solution of the problem of coupled equations can be calculated using various numerical methods [42, 71]. In Figure 3.5 the cross section of

an EHL contact between the rolling element and raceway is illustrated. This shows both the pressure profile and the lubricant film height profile through the center of the contact.
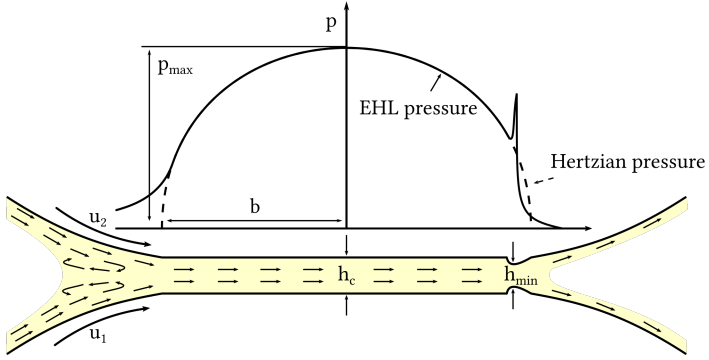
Figure 3.5.: Visualization depicting the contour of the gap geometry and the corresponding pressure distribution within an EHL contact.

Based on the numerical calculations, HAMROCK and DOWSON derived analytical formulas for the calculation of the central and minimum lubricant film height, assuming a parallel inflow of the fluid to the short HERTZian semi-axis [44].

$$H_{\min} = \frac{h_{\min}}{R_{\mathrm{x}}} = 3.63 U^{0.68} G^{0.49} W^{-0.073} \cdot \left(1 - e^{-0.68k}\right) \tag{3.36}$$

$$H_{\mathrm{c}} = \frac{h_{\mathrm{c}}}{R_{\mathrm{x}}} = 2.69 U^{0.67} G^{0.53} W^{-0.067} \cdot \left(1 - 0.61 e^{-0.73k}\right) \tag{3.37}$$

For the determination of the lubricant film heights, the dimensionless parameters U (speed parameter), G (material parameter), and W (load parameter) are necessary.

$$U = \frac{\eta_0 \sqrt{u_1^2 + u_2^2}}{E'R} \tag{3.38}$$

$$G = \alpha_\text{p} E' \tag{3.39}$$

$$W = \frac{Q}{E' R_\text{x}^2} \tag{3.40}$$

3.2.4. Friction Torque

The frictional torque T_res of an angular contact ball bearing is composed of several components, as shown in Equation 3.41. The individual components are discussed in more detail below.

$$T_\text{res} = T_\text{def} + T_\text{roll} + T_\text{diff} + T_\text{chur} \tag{3.41}$$

The friction torque due to irreversible deformation work of the whole bearing T_def can be calculated as suggested by Steinert [104]:

$$T_\text{def} = \sum_{n=1}^{Z} \left| \frac{\omega_\text{re}}{\omega_\text{ir}} \right| \cdot \left(T_\text{def,ir,i} + T_\text{def,or,i} \right) \tag{3.42}$$

The torque due to irreversible work of deformation of a single contact can be calculated according to the principle of Johnson [56]:

$$T_\text{def,i} = \frac{3}{16} \cdot \kappa_\text{d} \cdot b_\text{i} \cdot Q_\text{i} \tag{3.43}$$

With the material specific damping constant κ_d.

The hydrodynamic rolling friction of the bearing can be determined according to Steinert using the following equation:

$$T_\text{roll} = \frac{d_\text{re}}{2} \cdot \sum_{n=1}^{Z} \left| \frac{\omega_\text{re}}{\omega_\text{ir}} \right| \left(\cdot F_\text{roll,ir,i} + F_\text{roll,or,i} \right) \tag{3.44}$$

The hydrodynamic rolling friction of a single contact can be calculated according to Gohar [35]:

$$F_{\text{roll}} = 8.6 \cdot \left(\frac{2 \cdot U}{W} \cdot G^{-0.2} \right) \tag{3.45}$$

The frictional torque due to the relative motion of the surfaces in contact, T_{diff}, for the bearing can be calculated from the frictional power, P_{diff}, and the rotational speed of the inner ring, ω_{ir}:

$$T_{\text{diff}} = \sum_{n=1}^{Z} \left| \frac{1}{\omega_{\text{ir}}} \right| \cdot \left(P_{\text{diff,ir,i}} + P_{\text{diff,or,i}} \right) \tag{3.46}$$

The friction power results from the friction forces in the contacts i on the inner ring and on the outer ring, $F_{\text{diff,ir,i}}$ and $F_{\text{diff,or,i}}$, respectively:

$$P_{\text{diff,ir,i}} = \sum_{x_{\text{ir,i}}, y_{\text{ir,i}} \in A_{\text{ir,i}}} F_{\text{diff,ir,i}}(x_{\text{ir,i}}, y_{\text{ir,i}}) \cdot \Delta v_{\text{ir,i}}(x_{\text{ir,i}}, y_{\text{ir,i}}) \tag{3.47}$$

$$P_{\text{diff,or,i}} = \sum_{x_{\text{or,i}}, y_{\text{or,i}} \in A_{\text{or,i}}} F_{\text{diff,or,i}}(x_{\text{or,i}}, y_{\text{or,i}}) \cdot \Delta v_{\text{or,i}}(x_{\text{or,i}}, y_{\text{or,i}}) \tag{3.48}$$

The associated frictional forces $F_{\text{diff,ir,i}}$ and $F_{\text{diff,or,i}}$ are obtained by integrating the shear stress τ across the contact area A_i:

$$F_{\text{diff,ir,i}}(x_{\text{ir,i}}, y_{\text{ir,i}}) = \sum_{x_{\text{ir,i}}, y_{\text{ir,i}} \in A_{\text{ir,i}}} \tau(x_{\text{ir,i}}, y_{\text{ir,i}}) \cdot dx_{\text{ir,i}} \cdot dy_{\text{ir,i}} \tag{3.49}$$

$$F_{\text{diff,or,i}}(x_{\text{or,i}}, y_{\text{or,i}}) = \sum_{x_{\text{or,i}}, y_{\text{or,i}} \in A_{\text{or,i}}} \tau(x_{\text{or,i}}, y_{\text{or,i}}) \cdot dx_{\text{or,i}} \cdot dy_{\text{or,i}} \tag{3.50}$$

For a constant speed-independent friction coefficient μ, the shear stress τ can be expressed as:

$$\tau(x_{\text{ir,i}}, y_{\text{ir,i}}) = \mu \cdot p(x_{\text{ir,i}}, y_{\text{ir,i}}) \tag{3.51}$$

$$\tau(x_{\text{or,i}}, y_{\text{or,i}}) = \mu \cdot p(x_{\text{or,i}}, y_{\text{or,i}}) \tag{3.52}$$

The relative velocities necessary to calculate the frictional power P_{diff} are obtained from the superposition of the relative velocity components from the Heathcote slip, $\Delta\vec{v}_{\text{Heathcote}}$, and the spin slip, $\Delta\vec{v}_{\text{spin}}$:

$$\Delta\vec{v}_{\text{ir,i}} = \Delta\vec{v}_{\text{Heathcote,ir,i}} + \Delta\vec{v}_{\text{spin,ir,i}} = \begin{pmatrix} \Delta v_{\text{Heathcote,x}} + \Delta v_{\text{spin,x}} \\ \Delta v_{\text{spin,y}} \end{pmatrix} \tag{3.53}$$

$$\Delta\vec{v}_{\text{ir,i}} = \Delta\vec{v}_{\text{Heathcote,or,i}} + \Delta\vec{v}_{\text{spin,or,i}} = \begin{pmatrix} \Delta v_{\text{Heathcote,x}} + \Delta v_{\text{spin,x}} \\ \Delta v_{\text{spin,y}} \end{pmatrix} \tag{3.54}$$

These equations are valid for the coordinate system shown in Figure 3.4. The torque from the churning losses, T_{chur}, can be determined experimentally. For oil-lubricated angular contact ball bearings there are calculation approaches according to SKF [1]. However, since unsealed bearings operated under very low speeds and small oscillation angles are used in this work, it can be assumed that the churning losses are negligible.

3.2.5. Slip in the transient case

The slip conditions described above are applicable solely to fully developed rolling motion. However, in the transient case, when the rolling motion is initiated from rest, a relative motion between the surfaces occurs primarily in the outer regions of the contact. This phenomenon was demonstrated for a sphere-disc contact by MINDLIN and CATTANEO [79]. When a tangential force is applied to an elastic contact under constant normal load, JOHNSON has mathematically shown that infinitely high tangential forces would theoretically occur in the edge regions of the contact zone if slip was not allowed ($\mu = \infty$) [56]. In reality, slip occurs as soon as a traction limit is exceeded ($\tau > \mu \cdot p$). This limit is exceeded first in the outer areas of the rolling contact, since the pressure $p(x, y)$ is low and the tangential stress is high due to the large center distance. In the areas where the traction limit is not reached, the contact partners adhere. For the case of an angular contact ball bearing, numerical contact simulations have been utilized to demonstrate the formation of sliding and adhesion regions [96, 100].

Amplitude Ratio

The amplitude ratio $e = \frac{x}{2b}$ is a parameter employed to categorize the operating conditions of oscillating rolling bearings. When the oscillation angles are very small, such that a portion of the contact surface remains in continuous contact during the oscillation, the amplitude ratio is $e < 1$. Such conditions arise, for example, when bearings are exposed to unwanted vibrations. Conversely, when the oscillation angles are large enough that no surface element remains in continuous contact with the contact partner, the amplitude ratios are $e > 1$. These oscillations are often induced intentionally during operation for specific purposes.
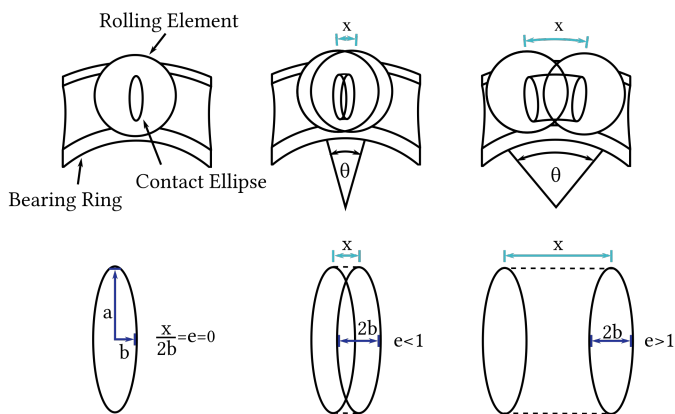
Figure 3.6.: Visual representation showcasing distinct amplitude ratios: e=0 on the left, e<1 in the center, and e>1 on the right.

The amplitude ratio plays a significant role both from a contact mechanical and lubrication standpoint. For amplitude ratios $e < 1$, the kinematics in the contact may not fully develop, resulting in partial slip areas and sticking zones, as discussed in section 3.2.5. Additionally, relubrication of the contact area becomes challenging as certain parts of the contacting surfaces remain in constant contact. For amplitude ratios $e > 1$, complete rolling (no sticking zones) typically occurs during oscillation, and relubrication of the contact area is possible. Moreover, Maruyama has demonstrated that a lubricating film buildup for an oil-lubricated rolling contact is feasible only when the amplitude ratio exceeds $e > 1.6$ [75].
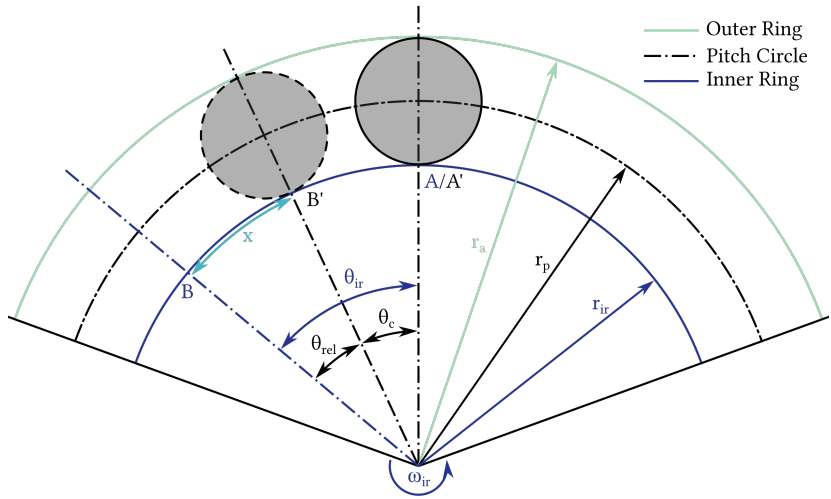
Figure 3.7.: Schematic outlining of the procedure for calculating the amplitude ratio denoted as $e = \frac{x}{2b}$.

To calculate the amplitude ratio e for an angular contact ball bearing, we are interested in the relative displacement of the center of the contact surface with respect to the raceway surface. In Figure 3.7, a two-dimensional sketch depicts the rolling element positioned between the two raceways. When the inner ring is rotated counterclockwise by an angle θ_{ir}, the original contact point A moves to point B. Simultaneously, the center of the rolling element moves with the cage, resulting in the ball-side contact point A' shifting to B'. The distance traveled by the contact midpoint x can thus be described as the difference in the distances covered by the raceway contact point and the ball center point:

$$x = \overline{AB} - \overline{A'B'} \tag{3.55}$$

$$\overline{AB} = \theta_{ir} \cdot r_{ir} \tag{3.56}$$

$$\overline{A'B'} = \theta_c \cdot r_{ir} \tag{3.57}$$

Thus, for the over-rolled path x, the following relationship is obtained:

$$x = (\theta_{ir} - \theta_c) \cdot \frac{d_{ir}}{2} \tag{3.58}$$

Under the simplified assumption of $\alpha = \alpha_{ir} = \alpha_{or}$, which is valid as long as the rotational speeds are low, and the assumption that $d \approx d'$, Equation 3.2 can be simplified, and the following relationship is obtained for ω_c:

$$\theta_c = \frac{\theta_{ir}}{2} \cdot \left(1 - \frac{d_{re}}{d_p} \cdot \cos\alpha\right) \tag{3.59}$$

$$d_{ir} = d_p - d_{re} \cdot \cos\alpha \tag{3.60}$$

The rolling path x can be expressed as a function of the angle of rotation of the inner ring Ω_{ir} in the following form:

$$x = \theta_{ir} \cdot \left(\frac{d_p^2 - d_{re}^2 \cdot \cos\alpha^2}{4 \cdot d_p}\right) \tag{3.61}$$

The amplitude ratio can then be calculated as:

$$e = \frac{x}{2b} = \frac{\theta_{ir}}{2b} \cdot \left(\frac{d_p^2 - d_{re}^2 \cdot \cos\alpha^2}{4 \cdot d_p}\right) \tag{3.62}$$

3.3. Grease Lubrication in Rolling Element Bearings

The primary purpose of grease in rolling bearings is to establish an intermediate layer within the rolling contact to prevent premature bearing failure caused by wear or fatigue damage due to high shear stress.

The maximum service life of the bearing can only be achieved, if a fully separating lubricant film can be build up. A prerequisite for this is the supply of an adequate amount of lubricant to the inlet of the rolling contact. In the case of oil lubrication, such as oil bath or oil injection lubrication, the supply to the contacts is sufficient, allowing easy prediction of the lubricant film height and

lubrication condition using equations, such as those provided by Hamrock et al. for fully flooded conditions [41]. However, oil lubrication demands increased design and maintenance efforts. A favorable and low-maintenance alternative lies in grease lubrication. In the case of grease lubrication, the lubrication mechanisms differ from those of pure oil lubrication due to the multiphase structure of greases.

Grease is characterized as a dispersion of thickener in a liquid lubricant, which is generally mineral and/or synthetic oil. It exhibits a solid to semi-solid state and possesses a visco-elastic, semi-plastic flow behavior [51, 30]. The paste-like consistency of grease enables it to adhere to the bearing surfaces effectively, allowing it to remain in place without requiring additional retention mechanisms. This property of grease minimizes the design effort required to keep the lubricant within the bearing.

The lubricating process of rolling contacts in case of grease lubrication can be divided into two phases. Initially, there is the churning phase, in which the rolling elements and the cage have to work their way through piles of grease in the freshly filled bearing. In this phase there is a redistribution of grease through macroscopic flow, which is influenced by the operating conditions and the geometry of the bearing components. At the start of this phase, the inlets of the rolling elements are filled with grease, resulting in an increased lubricant film height compared to contacts lubricated with base oil [15]. This can be attributed to the increased viscosity due to the thickener content [80]. As the churning phase progresses, the thickener is increasingly displaced from the track, but piles of grease can be repeatedly transported into the contact area. When the redistribution of the grease is largely complete, the bleeding phase starts [95]. During the bleeding phase, the contact is primarily supplied with base oil, which may, however, contain worked thickener particles. The state of lubrication in this phase depends on feeding mechanisms that supply the track with base oil from the surrounding areas and on loss mechanisms that displace base oil from the track. Additionally, replenishment of base oil is possible, whereby displaced base oil is returned to the contact area.

These mechanisms are shown in 3.8 according to Lugt [73]. Essential for the supply of the contact is that the grease releases base oil. This can occur through simple oil bleeding or by the degradation of the thickener structure due to shear or other aging processes, which prevents the thickener from retaining the base oil [78]. Shear can take place in the rolling contact, in the vicinity of the contact, or during the interaction between the rolling element

and the cage [18, 17]. The released base oil can be driven into the contact area by various forces. One of the most important drivers is the capillary force, that draws oil into the gap between the rolling element and raceway [53]. Supporting mechanisms include surface tension-driven flow, where the oil wets the surface of the track to minimize surface energy [23, 31], and temperature gradient-driven flow, where the Marangoni effect causes oil to flow in the direction of the temperature gradient towards lower temperatures [60]. Depending on the gradient, this effect can be classified as either a feeding or a loss mechanism. With increasing rotational speed, the relevance of flow driven by centrifugal forces increases. These forces can be categorized as either feeding or loss mechanisms based on their direction of action [31]. The cage can also play an important role in supplying the contact with lubricant. Damiens has demonstrated that the cage can contribute to redistributing the lubricant on the rolling element, thus enhancing the lubricant supply to the contact [25].

The feed mechanisms are counteracted by the loss mechanisms, which cause a displacement of lubricant from the contact zone. At the beginning of the bleeding phase, or if a lot of base oil is present, simple displacement of the lubricant in front of the rolling element is a relevant loss mechanism. In most cases, however, lubrication in the bleeding phase takes place only through thin layers of oil located on the surfaces of the contact partners. The lubricant film height then results largely from an addition of the layer thicknesses on the contact partners, which is reduced as a result of the contact pressure. In this scenario, a pressure-driven flow from the contact zone due to the pressure gradient within the contact area is significant. Since the viscosity increases significantly under the high contact pressures, this flow is limited to very small quantities of oil in the peripheral areas of the contact. Only the quantities of oil that do not flow into the track of the rolling elements can be regarded as loss. Additionally, evaporation can contribute to a reduction in the amount of base oil present. This effect becomes particularly relevant at high temperatures and in bearings exposed to air-flow [63]. While a properly designed cage can have positive effects on contact lubrication by contributing to the redistribution of lubricant, a poorly designed cage could lead to stripping and loss of lubricant from the contact area.

In addition to the feed mechanisms that supply fresh base oil from the grease reservoirs surrounding the contact and the loss mechanisms that result in a permanent loss of oil components from the contact area, replenishment of oil can also occur. Replenishment refers to the process where initially displaced

oil is returned to the contact [31, 21]. This replenishment mechanism is dependent on the lubricant properties and can be influenced both positively and negatively by aging processes such as polymerization and oxidation.

In the bleeding phase, lubrication is predominantly facilitated by very thin layers of base oil present on the surfaces of the rolling elements and the raceways. Due to the limited oil supply, the formation of a lubricant film through hydrodynamic effects is restricted. This phenomenon, characterized by a reduced lubricant film height due to the limited oil supply compared to the fully flooded inlet, is known as starvation, and will be explained in more detail in the next section.

Feed Mechanisms

- Oil Bleeding
- Bleeding due to shear
- Capillary forces
- Surface tension driven flow
- Temperature gradient driven flow
- Centrifugal force driven lubricant flow
- Redistribution through the cage

Replenishment

Rolling Element - Raceway
Contact

- Polymerization
- Oxidation

- Displacement
- Pressure induced sideflow
- Temperature gradient driven flow
- Centrifugal force induced side flow
- Evaporation
- Cage scraping

Loss Mechanisms

Figure 3.8.: Feed and loss mechanisms in grease lubricated bearings according to WIKTRÖM and LUGT [116, 73].

3.4. Starvation in Rolling Element Bearings

Common formulas used to determine the lubricant film height in a rolling contact are applicable only when a completely filled inlet gap is present. According to ERTEL-GRUBIN, the hydrodynamic pressure buildup can start infinitely far before the HERTZian contact zone [26, 37]. As stated in Chapter 3.3, however, only small quantities of base oil are available in the inlet during the bleeding phase under grease lubrication. Consequently, the hydrodynamic pressure buildup begins at a finite distance from the HERTZian contact area, which is dependent on the base oil quantity in the inlet. In this situation, the lubricant film height is lower compared to the case of a fully filled inlet and is strongly influenced by the supply of base oil to the inlet. This phenomenon is referred to as starvation.

Known operating conditions in which starvation occurs in rolling bearings include grease lubrication [72], high-speed applications, lubrication with oil mist, and oil-air lubrication [82]. Additionally, low temperatures can also lead to starvation [115, 32, 64]. Starvation per se cannot be considered a negative effect, since a smaller base oil quantity in the inlet can result in reduced reverse flow and thus to lower friction losses [98]. In fact, moderate starvation can lead to reduced bearing friction, as shown by BALY [8]. On the other hand, with increasing starvation, increased traction due to mixed lubrication in the contact may prevent skidding [85]. Nevertheless, if conditions of severe starvation persist, to the extent that a sufficient lubricant film cannot be established, premature bearing failure due to wear or surface-induced fatigue is likely to occur.

To prevent the occurrence of these conditions, several methods have been employed in the past to determine the height of the lubricant film based on the inlet lubricant supply and to quantify the level of starvation with respect to the operational parameters.

Various models have been developed to quantify the degree of starvation. Initially, WEDEVEN observed the development of starved contacts and established a relationship between the reduction in lubricant film height within the contact and the distance of the oil-air meniscus from the HERTZian contact area [114]. HAMROCK ET AL. numerically determined a critical inlet distance for the onset of starvation [43]. A more advanced model using free boundary conditions was developed by CHEVALIER [22]. This model incorporates a modified Reynolds approach that considers the ratio of oil film thickness to

gap height, enabling the determination of contact conditions for various inlet layer distributions. CANN ET AL. have proposed a starvation model to account for replenishment of the contact due to surface tension effects, where SD is the degree of starvation (see 3.63) [16]. Under oil lubrication on an optical EHL test rig, the influence of the individual parameters except for the surface tension were investigated.

Under oil lubrication, the influence of several parameters, including the base oil viscosity η_0, entrainment speed u_e, length of the HERTZian contact ellipse perpendicular to the rolling direction a, and the height of the lubricant film layer in the inlet of the contact $h_{\mathrm{oil}\infty}$, on the lubricant film height in the contact was investigated on an EHL tribometer. Through this study, a relationship was established between the lubricant film height and the degree of starvation as given in Equation 3.63. The impact of surface tension (σ_{s}) was neglected in the analysis.

$$SD = \frac{\eta_0 \cdot u_e \cdot a}{h_{\mathrm{oil}\infty} \cdot \sigma_{\mathrm{s}}} \tag{3.63}$$

According to CANN, the relationship between the degree of starvation (SD) and the measured lubricant film height can be represented as follows:

$$\frac{h_{\mathrm{c}}}{h_{\mathrm{ffc}}} = \begin{cases} 1 & \text{if } SD \leq 1.5 \\ \left(\frac{1.5}{SD}\right)^{1.67} = \left(\frac{1.8e-6}{u_e \cdot \eta_0 \cdot a}\right)^{1.67} & \text{if } SD > 1.5 \end{cases} \tag{3.64}$$

Here h_{c} is the measured central lubricant film height in contact and h_{cff} the expected lubricant film height under fully flooded conditions. From $SD = 1.5$ h_{c} is thus smaller than h_{cff} and one can speak of an onset of starvation. CEN ET AL. performed continuously rotating bearing tests on deep groove ball bearings and related them to the parameters present in SD similar to the approach used by CANN ET AL. [21]. The test rig used allowed for capacitive lubricant film thickness measurement during the tests [20]. Similarly to CANN ET AL., CEN ET AL. varied the parameters of the starvation degree SD. They also examined two different cage geometries and bearings with full and half rolling element sets. The key finding of their investigation was that the normalized lubricant film thickness $\frac{h_{\mathrm{c}}}{h_{\mathrm{cff}}}$, measured in contact ($h_{\mathrm{c}}$) relative to the expected film height under fully flooded conditions (h_{cff}), for all tested bearings, greases, and number of rolling elements fell on a single curve when

Table 3.1.: Comparison of the starvation models proposed by CANN ET AL. and CEN ET AL..

Source	CANN	CEN
Onset of Starvation	$u_e \cdot \eta_0 \cdot a = 1.8e - 6\,\mathrm{N}$	$u_e \cdot \eta_0 \cdot a = 1.274e - 4\,\mathrm{N}$
$\frac{h_c}{h_{cff}}$	$\left(\frac{1.8e-6}{u_e \cdot \eta_0 \cdot a} \cdot N\right)^{1.67}$	$\left(\frac{1.274e-4}{u_e \cdot \eta_0 \cdot a} \cdot N\right)^{0.791}$

plotted against the product of base oil viscosity (η_0), entrainment speed (u_e), and the long half-axis of the contact ellipse (a). Compared to CANN ET AL. no influence of the amount of oil available could be detected. However, it is mentioned that the oil separation rate can become quite relevant at very low amounts of available oil. The investigation revealed that track replenishment between the rolling elements seemed negligible, given that the results were independent of the number of rolling elements used in the bearings. This is consistent with the theoretical studies carried out by JACOD ET AL. [53]. A comparison of the film thickness equations of CANN ET AL. and CEN ET AL. showed that starvation started significantly earlier and exhibited a higher decay rate on the EHL tribometer than in the bearing tests. This could be attributed to the lack of additional replenishment mechanisms, such as ball spin and cage replenishment. It should also be noted that the normalized lubricant film height in the bearing tests approaches a steady state value with increasing product of velocity, viscosity and contact width. For further details, Table 3.1 provides a comparison of the values according to CEN ET AL. [21].

3.5. Wear and Lubrication in Oscillating Rolling Element Bearings

The dissertation by PITROFF provides a comprehensive overview of the theories concerning causal (primary) and secondary wear mechanisms, as well as their interactions in oscillating contacts [88]. One widely accepted explanation for wear in oscillating contacts with a sliding component is based on TOMLINSON's theory, which suggests that the primary cause is the release of metallic particles due to adhesive forces between metal surfaces [108]. According to WRIGHT, these particles typically range in size from 100 Å to a few micrometers [118]. Once released, these particles and the free metallic surfaces of the contact partners undergo oxidation in the presence of oxygen,

resulting in the formation of oxide products visible as fretting corrosion, as demonstrated by Godfrey [34]. Almen also supports the idea that adhesion is root cause of wear, but specifies that the primary wear mechanism is caused by relative motion in the contact, regardless of whether rolling motion with a small amount of sliding or pure sliding is present. Wright suggests that the form of motion, i.e., whether reversing or continuous, has no effect on the primary wear mechanism, but that a significant difference in secondary wear mechanisms develops over time because the wear particles remain near the contact in the case of smaller oscillating movements and can therefore increase wear [118]. In such scenarios, mostly hard abrasive particles are generated. However, the type and properties of the wear particles can vary significantly depending on the specific tribological system, allowing for the possibility of a wear-reducing effect due to oxide formation in a tertiary phase.

In 1988, it was established that wear phenomena occurring in oscillating contacts are highly dependent on the operating conditions, with the oscillation amplitude and the resulting amplitude ratio e (see section 3.2) playing crucial roles. Broadly, two distinct ranges can be identified: oscillations with an amplitude ratio $e < 1$, where standstill marks can occur, and oscillations with an amplitude ratio $e > 1$, which can lead to false brinelling as a possible damage pattern [90]. An early study by Vingsbo et al. demonstrated that wear phenomena with different oscillation amplitudes in oscillating operation can give rise to fundamentally different damage mechanisms. Their research involved fretting experiments on a ball-on-disk tribometer under pure sliding motion. They identified three conditions: 'stick conditions', 'mixed stick-slip conditions', and 'gross slip conditions' [109]. For very small oscillation amplitudes ('stick conditions'), the deformation is realized mainly by elastic deformation of the contacting roughness peaks and plastic deformations of these contacts occur solely locally. In this region, the curve of tangential stress versus displacement corresponds to a linear shear stress-strain relationship, and no visible fretting wear is observed. As oscillation amplitudes increase ('mixed stick-slip conditions'), slip occurs in the outer areas of the contact surface where the traction limit is exceeded. This observation is qualitatively consistent with the theoretical considerations by Mindlin [79]. In the central contact zone, the contact partners continue to adhere. The transition between the adhesion zone and the annular slip zone experiences the highest stresses, leading to the formation of surface-induced cracks that propagate into the material [109]. These mixed stick-slip conditions have also been observed in

oscillating angular contact ball bearings, where the underlying kinematics involve mainly rolling motion. However, slip is also inevitable in this case, as demonstrated in contact simulations by SCHADOW and SCHWACK [96, 99]. They showed that for small oscillation amplitudes, slip occurs in the peripheral regions of the contact zone while sticking is present in the center of the contact zone. GREBE further demonstrated crack initiation in the transition region from the sticking zone to the slip zone based on focused ion beam (FIB) sections on rolling bearing raceways [36].

Once all asperity contacts are separated during an oscillation, VINGSBO refers to this stage as the 'gross slip regime'. In this regime, a scale-like surface structure is formed in which particles delaminate and detach from the surface. Under oxygen containing atmosphere this process is accelerated by oxidation of the wear particles. Severe wear occurs in this region as a result of particle delamination, but crack formation, as observed in the 'mixed stick-slip regime', is no longer evident [109].

The equivalent damage patterns for the 'large slip regime' in oscillating rolling bearings are referred to as false brinelling. False brinelling marks on the bearing raceway appear as depressions, resembling the well-known true brinelling marks caused by plastic deformation due to overloads. However, unlike the damage marks in true brinelling, there are no elevated 'shoulders' in the periphery of the depression due to plastic deformation. Moreover, the surface of the depression in true brinelling retains the original grinding marks, whereas in false brinelling marks, these grinding marks have been worn down, indicating material removal due to the wear process [33].

The development of the microscopic surface structure of a false brinelling damage was studied by PHANER-GOUTORBE ET AL. in 1997 using scanning tunneling microscopy (STM). For greases with poor performance, red-brown iron oxide residues were detected on the raceway surface after only a few minutes of testing. Subsequently, after about one hour, the oxide layer was removed, and approximately five hours later, material chippings were found on the raceway surface. However, after about 15 hours, these defects were no longer present on the surface [86]. These observations are in good agreement with the investigations on wear progress carried out in Section 6.1.1. Indeed, much of the research on false brinelling in oscillating rolling bearings has focused on investigating lubrication as a preventive measure rather than the detailed development of the damage. Early theories by HUDSON and MORTON

postulated that lubricant is displaced from the contact due to Hertzian pressure, and as a result, micro-welding (adhesion) of the roughness peaks occurs [81]. As early as 1937, Almen found that lubricants with lower viscosity can reduce false brinelling [3]. Additionally, in 1952, Herbek highlighted the crucial role of lubricant replenishment in preventing false brinelling [48]. A technical report from 1954 by Johnson provided detailed investigations into the influence of various lubricant parameters, such as consistency, shear stability, and oil separation, on false brinelling [54]. The results reaffirmed that greases with low consistency and high oil separation tend to perform better in preventing false brinelling. Furthermore, low shear stability can also help counteract false brinelling, as it leads to earlier destruction of the thickener structure, resulting in increased oil bleed, which aids in lubricant replenishment [54].

Recent studies, including those conducted by Maruyama et al., have explored the different lubrication mechanisms under oil and grease lubrication in oscillating rolling bearings. Maruyama et al. conclude that under oil lubrication, hydrodynamic lubricating film buildup can occur from an amplitude ratio greater than 1.5 ($e > 1.5$) [75]. Bearing tests revealed that wear can be effectively reduced by oil lubrication at amplitude ratios (e) exceeding 1.5, especially when using oils with high base oil viscosity [76]. Under grease lubrication, on the other hand, a low base oil viscosity and a high oil separation rate can provide effective wear protection at amplitude ratios greater than one ($e > 1$). These results under grease lubrication are consistent with the studies of Yano et al., Kita et al. and Saatchi [119, 61, 94]. However, based on their investigations, Maruyama et al. do not attribute the wear-reducing effect to the lubricating effect of the bleeding base oil, but assume that the base oil can easily escape from the contact, allowing the formation of a wear-reducing thickener film.

The effect of contact replenishment during motion halting and reversal of motion, however, was shown by Cen et al. [19]. Through electrical capacitance measurements, they could measure a quick film collapse during halting of motion, but a greater than expected increase in film height after initiating the reversing motion, which is attributed to lubricant replenishment. Also, in this work, specific investigations were made on the reflow behavior of greases in oscillating rolling bearings and in oscillating model contacts (see Section 6.2.2).

Table 3.2.: Comparison of the standard test procedures for oscillating rolling element bearings.

Test	Fafnir	SNR-FEB2
Bearing Type / -	Custom Thrust Ball Bearing	Type 51206 Thrust Ball Bearing
Outer Diameter/ mm	35.69	52
Number of rolling elements / -	9	12
Oscillation frequency f / Hz	30	25
Axial load F_a / N	2 450	8 000
Max. contact pressure p_H / GPa	1.87-2.28	2.3
Oscillation angle θ / °	12	6
Amplitude ratio e / -	5.5	3.4
Time t / h	22	50
Oscillation cycles N	2 376 000	4 500 000

Research has been carried out in the field of grease composition and additives, particularly in the context of false brinelling prevention. Roehner in 1952 and Johnson in 1954 found that additives such as MoS_2, ZnO and graphite, were ineffective or even counterproductive when it comes to grease performance [54, 93]. Johnson's work involved testing different thickeners, such as natrium-calcium, calcium, and lithium, and he concluded that wear prevention does not solely depend on the type of thickener used but is more influenced by the consistency and shear stability of the grease composition [54]. Kato et al. revealed on the basis of Fafnir-tests that the use of polyurea thickener resulted in a significant reduction of wear compared to greases with lithium thickener. However, the addition of extreme pressure (EP) additives like organic phosphate molybdenum (MoP) or other additives such as MoS_2 showed relatively small effects in comparison [59]. More recent investigations by Pape et al. demonstrated a notable reduction in friction through the addition of graphene to a barium complex grease [84].

Additional research has been done on coatings and dry lubricants, especially in the field of space applications. A valuable overview over possible coatings can be found in the work of Lince [68]. However, in the course of this work, they will not be discussed in detail.

In order to test the suitability of lubricants for use in oscillating rolling bearings, there are standard tests such as the Fafnir [6] and the SNR-FEB2 [28] test. Both tests are basically similar in structure. In a test setup, two thrust ball bearings are loaded with a constant axial force. The bearings are driven in an oscillating manner via a crank mechanism under the operating parameters listed in Table 3.2.

For both tests an amplitude ratio of $e > 1$ and a frequency of 30 Hz and 25 Hz is chosen. After a fixed number of oscillation cycles of approximately 2.4 million for the Fafnir and 4.5 million cycles for the SNR-FEB2-test, the bearing washers are cleaned and weighed again, as they were before the test, to determine the mass loss due to wear. The suitability of the grease is assessed on the basis of the mass loss, with a mass loss of less than 2 mg being considered very good for both standards [6, 28].

There is little research that has addressed the influence of operating parameters such as oscillation frequency, load, and amplitude on the occurrence of wear in the range of amplitude ratios greater than 1 ($e > 1$). In addition, there is no approach to quantify the operating conditions of oscillating bearings in terms of their tendency to cause wear. It is at this point that the present work begins.

4. Objective of the work

Institutions like the GERMAN INSTITUTE FOR STANDARDIZATION (DIN) the INTERNATIONAL ORANIZATION FOR STANDARDIZATIONS (ISO) or the AMERICAN NATIONAL STANDARDS INSTITUTE (ANSI) provide standards for rolling bearings under continuous rotation and variable operating conditions. They are mostly based on component tests by bearing manufacturers and therefore of empirical nature [46]. However, there is no standard for rolling bearings in oscillating application. In addressing this, the WIND TURBINE DESIGN GUIDELINE DG03: YAW AND PITCH ROLLING BEARING LIFE provides a method for calculating the fatigue life in oscillating application is given according to HARRIS ET AL. [45]. Other researchers such as HOUPERT ET AL., MENCK or HWANG ET AL. have also developed calculation methods for the fatigue life under oscillating operation [50, 77, 52]. However, raceway wear is not considered in any of the calculation methods. As far back as 1946, HUDSON ET AL. had already pointed out the potential reduction in bearing service life due to wear, suggesting a factor of 0.35 reduction for safe operation [81]. In the WIND TRUBINE DESIGN GUIDELINE DG03 it is mentioned that oscillations below a critical angle can lead to wear and should be avoided or at least interrupted by oscillations with large angles. However, the guideline lacks explicit methods to account for possible wear in the fatigue life calculation. Studies conducted by the German research association FORSCHUNGSVEREINIGUNG ANTRIEBSTECHNIK E.V. (FVA) have demonstrated that raceway wear resulting from oscillating bearing operation can indeed lead to a significant reduction in fatigue life [97].

Wear damage in rolling bearings can have dual implications. It not only acts as a trigger for early fatigue failures but also plays a significant role in causing malfunctions due to unpredictable torque fluctuation in precision adjustment mechanisms. These effects are particularly critical in specialized domains like space applications, where even a minor increase in rotational resistance resulting from bearing wear can lead to complete lock-up of the entire drive

train. This issue arises because motors in such applications are designed with minimal dimensions to meet strict weight limitations [11, 87, 70].

A primary goal during oscillating operation is to avoid wear, making it a fundamental objective of this study. More specifically, a model is developed on the basis of which the operating conditions in oscillating rolling bearings under grease lubrication can be assessed in terms of their tendency to cause raceway wear. In order to achieve this goal, operating parameter studies are carried out using component tests on angular contact ball bearings as well as model tests on an optical EHL-tribometer. The main emphasis is on identifying lubrication mechanisms that are specific to various operating conditions. The study will investigate the influence of oscillation frequency (f), oscillation angle (θ), and contact pressure (p) on wear, while also considering different lubricant parameters using both industrial and specially formulated model greases. Furthermore, the internal bearing geometry, with a particular focus on the impact of the bearing cage on lubrication, will be examined.

5. Material and methods

In this chapter, the test rigs employed, along with the test specimens and lubricants under investigation are presented. Furthermore, the methods utilized for assessing the test data are explained.

5.1. Oscillating Bearing Test Rig

In this study, all rolling bearing tests were conducted on a specific test rig, as depicted in Figure 5.1. The test rig is equipped with a position-controlled asynchronous servo motor (2) serving as drive unit. The motor shaft is connected to the test unit shaft through a torque transducer that includes an integrated incremental encoder (3). This configuration enables the measurement of angle synchronous torque. The test unit comprises two angular contact ball bearings (ACBB) of type 7208, positioned in a face-to-face arrangement on the test shaft (5). The bearings are axially loaded through a hydraulic axial load unit (6), which is controlled by a hydraulic control system to maintain a constant load on the bearings throughout the tests. Additionally, the bearing temperature is monitored using two PT100 sensors (4), in contact with the stationary outer ring of the bearings during the experimental trials.

5.1.1. Tested Bearings

The bearings used in this study are angular contact ball bearings manufactured by FAG, designated as 7312-B-XL-TVP. Table 5.1.1 provides the relevant bearing data essential for further analysis. It will be demonstrated that the cage geometry plays a crucial role in oscillating operations. The bearings used are equipped with a fiber-reinforced plastic cage. A more comprehensive representation of the cage geometry can be found in Section 6.3. In Figure 6.43, the upper image displays the cage (OEM) along with the contained rolling
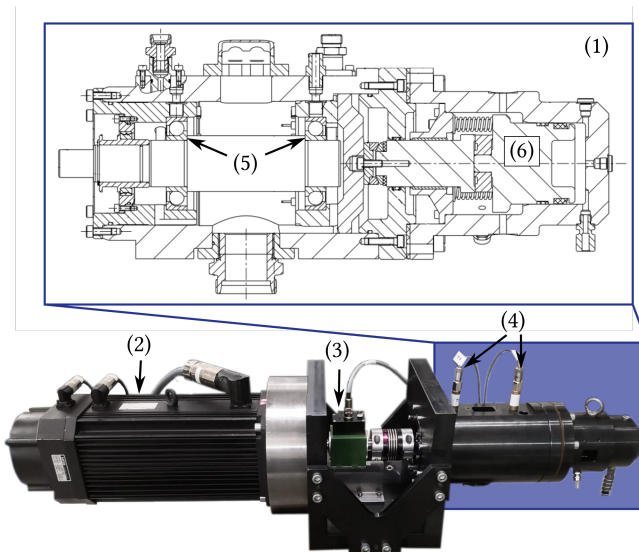
Figure 5.1.: Illustration of the test setup [111, 110]. (1) Test unit with type 7208 ACBB in face to face arrangement; (2) Position controlled asynchronous servo motor; (3) Torque transducer with integrated incremental encoder; (4) 2 PT100 temperature sensors; (5) Type 7208 ACBB in face to face arrangement; (6) Hydraulic axial load unit.

elements. The plastic cage partially encloses the rolling elements, differing from other cage types, such as stamped sheet metal cages. Figure 6.40 illustrates the cage cut perpendicular to the resulting axis of rotation of the rolling element, showing the angles formed between the lines connecting the center of the rolling element and the edges of the cage. Section 6.3 elaborates on how this angle can significantly influence the wear behavior of oscillating rolling bearings.

5.1.2. Torque Analysis

In addition to the detailed optical analysis of damage, which is explained further in Section 5.2, the evaluation of the rolling bearing tests on the oscillating bearing test rig relies on torque and temperature data. Here, we focus

Table 5.1.: Characteristics of the examined angular contact ball bearings (ACBB) of type FAG 7208-B-XL-TVP.

	Value	Unit
Bearing Type	ACBB	-
Outer Diameter d_{o}	80	mm
Number of rolling elements	14	
Inner Diameter d_{i}	40	mm
Pitch Diameter d_{p}	60	mm
Contact Angle α	40	°
Diameter Rolling Element d_{re}	11.93	mm
Osculation Inner Ring κ_{ir}[1]	0.52	-
Osculation Inner Ring κ_{or}[1]	0.54	-

[a] Osculation κ calculated according to BRÄNDLEIN ($\kappa = \frac{r_{\mathrm{ir/or}}}{d_{\mathrm{re}}}$) [13]

on describing how the assessment of the torque data is conducted. The torque is measured using a Burster 8661-5050-V2400 torque transducer, connected to both the motor shaft and the test shaft through two bellows couplings. This particular torque transducer features a 2-range measurement capability, with a maximum detectable torque of 50 Nm. The measuring range can be switched between 0-10 Nm and 0-50 Nm. Additionally, the measuring shaft is equipped with an integrated incremental encoder, offering an angular resolution of 0.02°. The recorded torque and angle data are output via LabView in .csv format, along with a time stamp. Typically, a measuring frequency of 1000 Hz is employed, ensuring that a minimum of 80 measuring points are captured per oscillation cycle. This frequency provides sufficient data resolution for reliable analysis during the tests.

In the evaluation of the tests, one of the key indicators of raceway damage is the maximum torque per oscillation cycle. Figure 5.2 presents an example of recorded torque data from a test, showcasing increasing torque over time due to severe raceway damage. The torque is plotted in three dimensions, with respect to the oscillation angle and the number of cycles on the left-hand side of the figure. The right-hand side of Figure 5.2 displays a side view, where the torque is plotted against the cycle number. The black dashed line represents the trend of the maximum torque per oscillation cycle, while the horizontal dashed line indicates the maximum torque measured during the entire test.
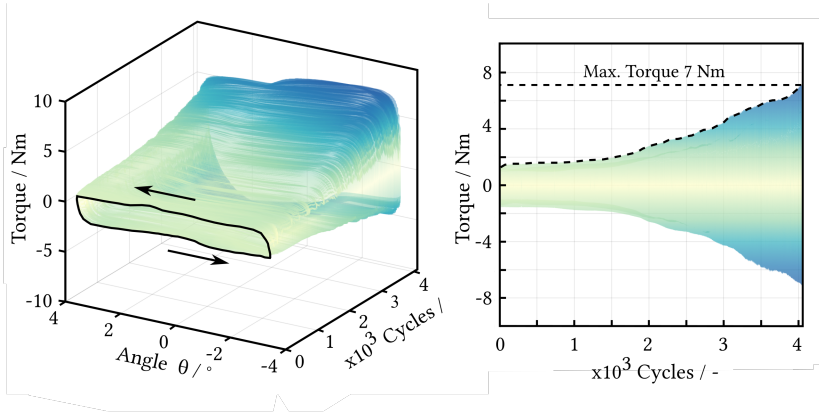
Figure 5.2.: The left graph presents the torque signal obtained after subtracting the inertia of the moving components, recorded during a test at a frequency of $f = 3\,\text{Hz}$ and an oscillation angle of $\theta = 7°$. The direction of oscillation is indicated by the black arrows. The right graph illustrates the torque signal variation across successive oscillation cycles.

This maximum torque value is critical for evaluation and comparison of the tests.

The maximum friction torque T_{fric} serves as an indicator for damage due to the increased friction coefficient. Since only the the frictional effect is of interest, the measured torque signal T_{res} is adjusted for the torque resulting from inertia T_{acc} of the oscillating components [117].

$$T_{\text{fric}} = T_{\text{res}} - T_{\text{acc}} \tag{5.1}$$

The acceleration torque T_{acc} can be computed by multiplying the moment of inertia of the oscillating components I with the angular acceleration $\ddot{\theta}$:

$$T_{\text{acc}} = I \cdot \ddot{\theta} \tag{5.2}$$

The moment of inertia of the oscillating components can be calculated by considering the individual contributions from various parts, including the moment of inertia of the measuring side of the torque measuring shaft I_{ts}, the

bellows coupling I_{bc}, the test shaft I_s, the inner rings of the bearings I_b, the cage set (including the rolling elements) I_c about the bearing axis, and the inertia of the rolling elements rotating about their own axis I_{re}. The moment of inertia for the torque measuring shaft is provided by the manufacturer, while the moment of inertia of the other components was determined using a Computer-Aided Design (CAD) tool. It is important to note that the torque measuring shaft, bellows coupling, test shaft, and inner rings experience the angular acceleration $\ddot{\theta}$. However, the cage set experiences an angular acceleration of approximately $\frac{\ddot{\theta}}{2}$, and the rolling elements experience an acceleration of $\frac{\ddot{\omega}_{re}}{2}$, where $\ddot{\omega}_{re}$ represents the angular acceleration of the rolling elements. Moreover, the contribution of each component to the main axis must be taken into account by considering their respective transmission ratios (i). The resulting moment of inertia (I) on the main axis is approximately given by the sum of the individual moments of inertia:

$$I_{\ddot{\theta}} = (i_{ts} \cdot I_{ts} + i_{bc} \cdot I_{bc} + i_s \cdot I_s + i_b \cdot I_b)_{\ddot{\theta}} \tag{5.3}$$

$$I_{\frac{\ddot{\theta}}{2}} = (i_c \cdot I_c)_{\frac{\ddot{\theta}}{2}} \tag{5.4}$$

$$I_{\ddot{\omega}_{re}} = (i_{re} \cdot I_{re})_{\ddot{\omega}_{re}} \tag{5.5}$$

Thus, the frictional torque T_{fric} can be calculated:

$$T_{fric} = T_{res} - I_{\ddot{\theta}} \cdot \ddot{\theta} + I_{\frac{\ddot{\theta}}{2}} \cdot \frac{\ddot{\theta}}{2} + I_{\ddot{\omega}_{re}} \cdot \ddot{\omega}_{re} \tag{5.6}$$

Figure 5.3 depicts the torque curve representing one complete oscillation cycle at an oscillation frequency of 5 Hz and an oscillation angle of 45°. The dark blue curve represents the measured torque T_{res}, while the green curve illustrates the friction torque T_{fric} after being adjusted by subtracting the acceleration torque T_{acc}.

Both the oscillation frequency (f) and the oscillation angle (θ), which determine the occurring accelerations, are at the upper end of the investigated parameter spectrum for the cycle shown. The difference between the maximum torques $T_{res,max}$ and $T_{fric,max}$ is approximately 0.5 Nm. However, it is worth noting that due to damage, the torque can increase significantly, as demonstrated in Figure 5.2. In some tests, as discussed in Section 6.1.1, the torque increase exceeds 20 Nm. Consequently, the impact of inertia on the
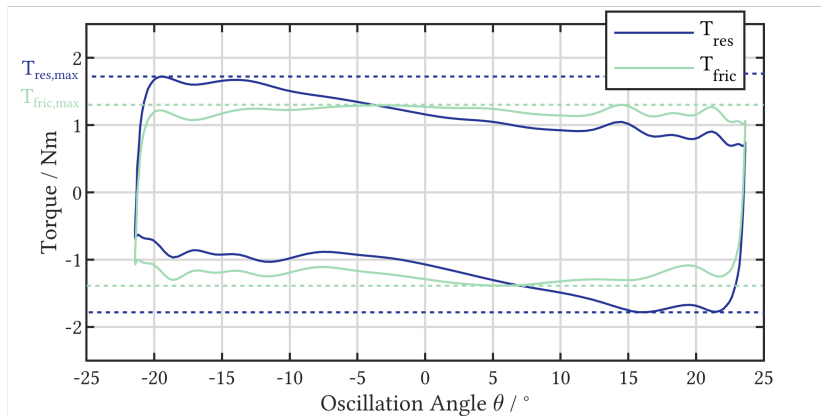
Figure 5.3.: Comparison between the recorded torque T_{res} (depicted in blue) and the friction torque T_{fric} (depicted in green), both adjusted for the acceleration torque T_{acc}, during an examination conducted at a frequency of $f = 5\,\mathrm{Hz}$ and an oscillation angle of $\theta = 45°$. The dashed lines mark the upper and lower limits of the torque achieved within the cycle.

torque increase due to damage in the rolling element raceway contact is relatively small.

The investigations in Section 6.1.1, require the calculation of the dissipated energy during the oscillation process. The dissipated energy E_d can be determined using FOUVRY's approach, considering the area enclosed by the tangential force and sliding distance curves during oscillation [27]. Although FOUVRY's approach originally applied to a ball-on-disk experiment with pure sliding, it can be equivalently used for oscillating bearings by considering the areas enclosed by the friction torque curves over the oscillation angle. In Figure 5.4, two exemplary torque curves are shown, representing the possible qualitative behaviors during a test with two 7208 angular contact ball bearings. The green curve corresponds to the ideal torque curve for an undamaged bearing, originally described by DAHL and later discussed by TODD [24, 107]. The curve initially increases linearly with a slope s due to the elastic behavior of the contact partners and then approaches the steady-state torque (T_s). In this case, the maximum torque (T_{max}) is approximately equal to the steady-state torque (T_s). For more advanced damage on the bearing raceway, curves may appear similar to the blue curve in Figure 5.4, where torque peaks are

observed at the reversal points, resulting in the maximum torque (T_{max}). The accumulated dissipated energy (E_{dn}) after n oscillation cycles is calculated as the sum of the dissipated energies per cycle ($E_{d,i}$):

$$E_{dn} = \sum_{i=1}^{n} E_{d,i} \tag{5.7}$$
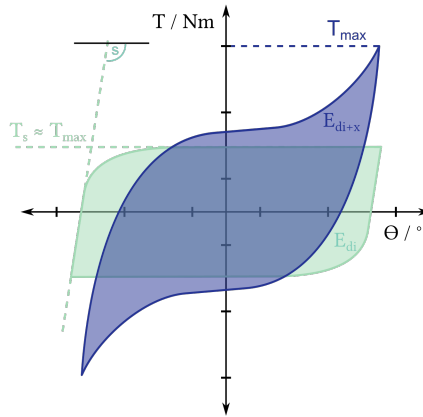
Figure 5.4.: Illustration of two exemplary torque curves. In green is the curve of an undamaged bearing, with the slope s and the steady-state torque T_s according to DAHL. The blue curve depicts the qualitative shape of a torque curve indicating significant wear damage. Transparently shaded regions signify the dissipated energy areas $E_{d,i}$ (green) and $E_{d,i+x}$ (blue), corresponding to the respective oscillation cycle.

In Section 6.1.1, the findings concerning the relationship between the dissipated energy (E_{dn}) and the wear volume (V_{wear}) are presented. The detailed description of the method used to determine the wear volume is provided in Section 5.2.

5.2. Optical Methods of Bearing Analysis

To perform a qualitative and quantitative assessment of the damage occurring in the bearings, optical analysis methods are employed. Two types of micro-

scopes are used for this purpose: a digital reflected-light microscope (Keyence VHX-600) and a confocal laser scanning microscope (Keyence VKX-250). The Keyence VHX-600 produces light microscopic images, enabling the identification of harmfull changes in the raceway surfaces. These images are compared with known damage patterns, facilitating the deduction of causal damage mechanisms. In contrast to the qualitative analysis by the reflected-light microscope, the confocal laser scanning microscope enables the recording of the surface topography. This is utilized to quantify the wear volume on the raceway surface, as described in Section 6.1.1. For this purpose, the topography of the bearing's raceway surface is captured using a 10x-objective with an aperture of 0.3, covering a defined section of size $3870 \times 4750 \, \mu m^2$. The chosen section size ensures that the resulting damage marks are fully captured, with an additional surrounding area of $500 \, \mu m$ of undamaged raceway, to which a surface representing the original undamaged state can be fitted later on. For the fitting function, a bivariate polynomial with a maximum degree of 2 is used:

$$z_{\text{fit}}(x, y) = a_0 + a_1 \cdot x + a_2 \cdot y + a_3 \cdot x^2 + a_4 \cdot y^2 + a_5 \cdot xy... \tag{5.8}$$
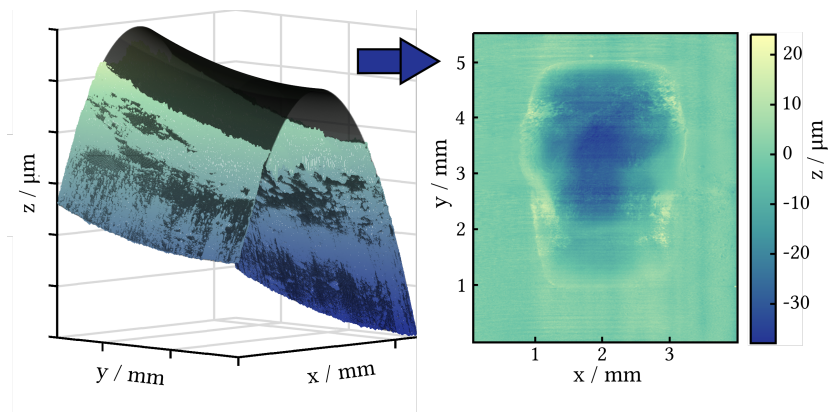
Figure 5.5.: Visual depiction of the wear volume computation process. The left-side illustration presents a 3D cross-section of a wear mark's topography, highlighted in blue/green, alongside the interpolated undamaged surface shown transparently in black. The right-side image portrays the difference image of a damaged mark, representing the outcome of the difference between the interpolated profile and the actual surface.

For each pixel, the height difference Δz between the interpolated and the real surface can be calculated. Under the settings used, a pixel of the recorded topography has a size of $p_{x,y} = 1375.075\ \frac{nm}{pixel}$ in the x and y directions. The wear volume is calculated as follows:

$$\Delta V = \sum_{i=1}^{N} (\Delta z \cdot p_x \cdot p_y) \tag{5.9}$$

In order to validate the calculation method and account for possible errors, 6 reference measurements were conducted on undamaged surfaces. Ideally, the measured differential volume on these surfaces should be zero. However, in practice, an offset volume may be measured due to deviations of the fitted function from the actual surface. The calculated volume on the undamaged inner ring is $V_{err,ir} = 5.3 \cdot 10^6 \pm 1 \cdot 10^6\ \mu m^3$, and on the outer ring, it is $V_{err,or} = 7.3 \cdot 10^6 \pm 1 \cdot 10^6\ \mu m^3$. The average values of these reference measurements are considered as an offset and are subtracted from the measured differential volume ΔV to obtain the wear volume V_{wear}.

$$V_{wear} = \Delta V - V_{err} \tag{5.10}$$

5.3. Optical EHL Test Rig

To conduct a more detailed analysis of grease lubrication mechanisms in oscillating contacts, an optical elastohydrodynamic lubrication (EHL) tribometer is utilized. Figure 5.6 illustrates the configuration of the employed tribometer. Mechanically, the system consists of a glass disk (3) driven by an electric motor. During rotating operation, the disc is driven via a timing belt, whilst for oscillation a crank mechanism is used. The rolling element (4) is positioned to rotate on two V-groove bearings. A lever mechanism, preloaded by a torsion spring, allows the rolling element to be pressed onto the glass disk with a defined normal force. When the glass disk undergoes movement under sufficient load, a rolling contact is established between the glass disk and the rolling element. This optical EHL tribometer enables precise investigation of the mechanisms involved in grease lubrication during oscillating contacts, providing valuable insights into the behavior and performance of lubricants under such conditions.
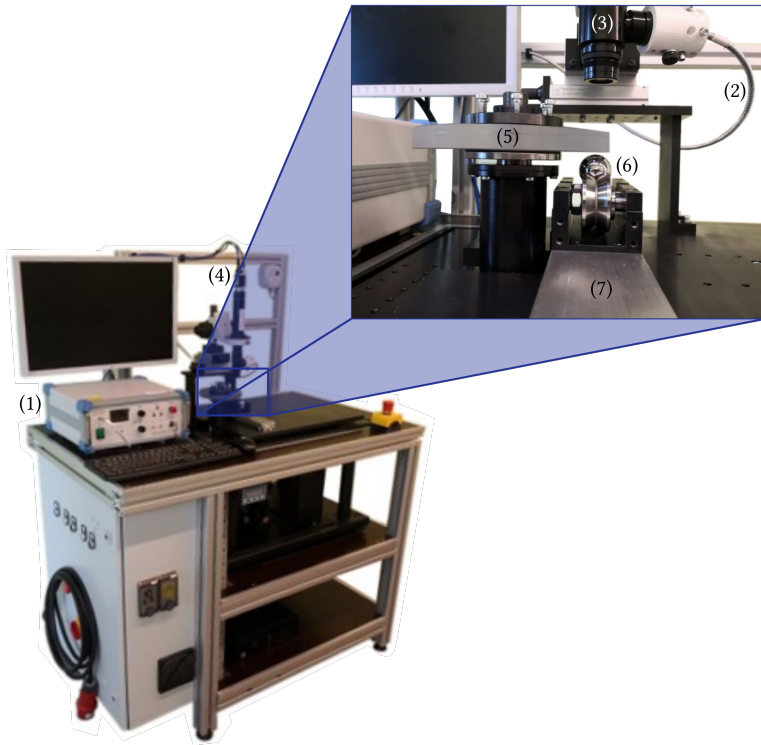
Figure 5.6.: Illustration of the optical EHL tribometer using the DIIM-method [69]. (1) Two colored laser; (2) Optical fiber; (3) Microscope optics; (4) CCD camera; (5) Coated glass disk; (6) Rolling element situated on V-groove bearings; (7) Load application mechanism.

The rotation of the drive during oscillation mode is converted into a reciprocal motion through a crank-rocker mechanism, which is depicted in a simplified form in Figure 5.7. The drive is supplied by a stepper motor continuously rotating at a fixed speed $\dot{\theta}_2$ around point O_{motor}. The axis of rotation for the motor (O_{motor}) and the disk (O_{Disc}) are separated by a distance r_1. The length of the crank lever is adjustable and denoted as r_2. The linkage r_3 and the length of the rocker lever r_4 are predetermined. The rotation of the disk is governed by the angle θ_4 with the rotation speed $\dot{\theta}_4$. The geometric

relationships governing the motion can be derived from the kinematic setup [102]:
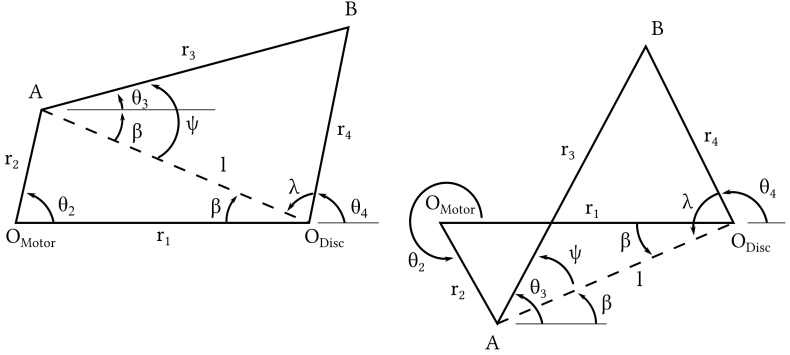
Figure 5.7.: Visual representation depicting the kinematics of the crank rocker mechanism responsible for converting the rotational motion of the motor at point O_{motor} into an oscillating motion of the glass disc at point O_{disc}.

$$\lambda = \arccos\left(\frac{l^2 + r_4^2 - r_3^2}{2 \cdot l \cdot r_4}\right) \tag{5.11}$$

$$\psi = \arccos\left(\frac{l^2 - r_4^2 + r_3^2}{2 \cdot l \cdot r_3}\right) \tag{5.12}$$

$$\beta = \arccos\left(\frac{l^2 + r_1^2 - r_2^2}{2 \cdot l \cdot r_1}\right) \tag{5.13}$$

These equations enable the calculation of the angles θ_3 and θ_4. It is necessary to make a distinction based on two cases: when $0 \leq \theta_2 < \pi$ and when $\pi \leq \theta_2 < 2\pi$:

$$\theta_3 = \begin{cases} \psi - \beta & \text{if } 0 \leq \theta_2 < \pi \\ \psi + \beta & \text{if } \pi \leq \theta_2 < 2\pi \end{cases} \tag{5.14}$$

49

$$\theta_4 = \begin{cases} \pi - (\lambda + \beta) & \text{if } 0 \leq \theta_2 < \pi \\ \pi - (\lambda - \beta) & \text{if } \pi \leq \theta_2 < 2\pi \end{cases} \qquad (5.15)$$

With the angular relations for θ_3 and θ_4 and the known rotational speed of the motor ($\dot{\theta}_2$), the rotational speed of the disk ($\dot{\theta}_4$) is:

$$\dot{\theta}_4 = \dot{\theta}_2 \cdot \frac{r_2}{r_4} \cdot \frac{\sin(\theta_3 - \theta_2)}{\sin(\theta_3 - \theta_4)} \qquad (5.16)$$

Figure 5.8 depicts the profile of the entrainment speed u_e between the glass disc and the rolling element as a function of the angular position (θ_4) of the glass disc. The motor is rotating with a constant $\dot{\theta}_2$, so that the oscillation angle θ_4 and thus the entrainment speed u_e of the glass disc will increase with increasing length of the crank lever r_2.
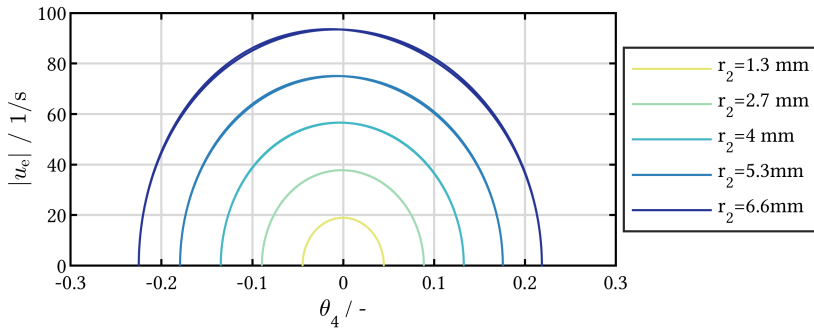
Figure 5.8.: Graph illustrating the profile of the entrainment speed u_e between the glass disc and the rolling element on the EHL tribometer. u_e is presented as a function of the angular position of the glass disc θ_4, considering various lengths of the crank lever r_2.

Assuming the condition of pure rolling between the rolling element and the disk, the entrainment velocity (u_e) can be expressed as follows, based on the distance of the contact point between the rolling element and the disk to the rotation axis of the disk (r_{dr}):

$$u_e = r_{dr} \cdot \dot{\theta}_4 \qquad (5.17)$$

When a lubricant is introduced into the contact between the rolling element and the glass disc, it forms a lubricant layer between the contact partners. The objective of the setup is not only to evaluate the behavior of the lubricant film purely optically but also to quantify the lubricant film height. To achieve this, light from a dichromatic laser source (1) is utilized, consisting of both a green laser with a wavelength of 520 nm and a red laser with a wavelength of 635 nm. This laser light is introduced into the beam path of the microscope (3) through an optical glass fiber (2). Subsequently, the laser light is directed through the glass disc into the contact area between the rolling element and the glass disc. The glass disc is coated on the contact side with a thin semi-reflective chromium layer with a thickness of 10 nm over which there is a transparent silica layer with a thickness of 200 nm.

The working principle is illustrated in Figure 5.9. To measure the lubricant film height, the Dichromatic Interference Intensity Modulation (DIIM) method [69] is employed. The glass disc's semitransparent chromium layer reflects a portion of the laser light and allows another part to pass through. The transmitted light travels through the silica layer, the lubricant film, and reflects off the rolling element. At the CCD sensor the phase-shifted beams interact, producing an interference pattern. The precise calculation of the resulting intensity of the interference pattern can be found in [38]. These intensity values are denoted as I_r for the red laser light and I_g for the green laser light.

$$I_i = \cos\left(\frac{4 \cdot n \cdot h \cdot \pi}{\lambda_i} + \phi_0\right), i = r, g \tag{5.18}$$

Linear superposition of the interferograms results in a modulated interference signal of intensity I_m, which consists of the carrier signal W_1 and the modulating signal W_2.

$$I_m = I_g - I_r$$

$$= -2 \cdot \sin\left(2 \cdot n \cdot h \cdot \pi \cdot \frac{\lambda_r - \lambda_g}{\lambda_r \cdot \lambda_g}\right) \cdot \sin\left(2 \cdot n \cdot h \cdot \pi \frac{\lambda_r + \lambda_g}{\lambda_r \cdot \lambda_g} + \phi_0\right) \tag{5.19}$$

$$= -W_2 \cdot W_1$$

$$W_1 = \sin\left(2 \cdot n \cdot h \cdot \pi \frac{\lambda_r + \lambda_g}{\lambda_r \cdot \lambda_g} + \phi_0\right) \tag{5.20}$$

$$W_2 = 2 \cdot \sin\left(2 \cdot n \cdot h \cdot \pi \cdot \frac{\lambda_r - \lambda_g}{\lambda_r \cdot \lambda_g}\right) \tag{5.21}$$

The modulation signal has a significantly longer wavelength than the individual wavelengths of the light source, increasing the range of lubricant film heights that can be determined without wavelength ambiguity.

Using the constructive and destructive intereference fringes, the lubricant film height can be determined using the following equations:

$$2 \cdot n \cdot h + \frac{\phi_0}{2 \cdot \pi} \cdot \lambda_i = N \cdot \lambda_i \tag{5.22}$$

$$2 \cdot n \cdot h + \frac{\phi_0}{2 \cdot \pi} \cdot \lambda_i = \left(N - \frac{1}{2}\right) \cdot \lambda_i \tag{5.23}$$

With n being the refractive index, h the film height, ϕ_0 the phase shift, λ the wave length and N the interference order. In this way, however, an unambiguous determination of the lubricant film height is only possible up to a lubricant film height of $h \leq \frac{\lambda}{2 \cdot n}$, since the order of the interference (N) is not known. Intensity modulation increases the equivalent wavelength of the modulation signal to λ_{eq}:

$$\lambda_{eq} = \frac{\lambda_r \cdot \lambda_g}{\lambda_r - \lambda_g} \tag{5.24}$$

A simple calculation example shows that the measurement range for the used light sources with wavelengths $\lambda_r = 635\,\text{nm}$ and $\lambda_g = 520\,\text{nm}$ increases from $\frac{\lambda_r}{2} = 326.5\,\text{nm}$ to $\frac{\lambda_{eq}}{2} = 1435.5\,\text{nm}$ assuming a refractive index of $n = 1$ and a phase offset of $\phi_0 = 0$. If higher lubricant film heights occur, the order of interference can be determined iteratively from image series, since during oscillation there is usually a zero speed crossing at which at least part of the contact has a very low lubricant film height of $h < \frac{\lambda_{eq}}{2}$.
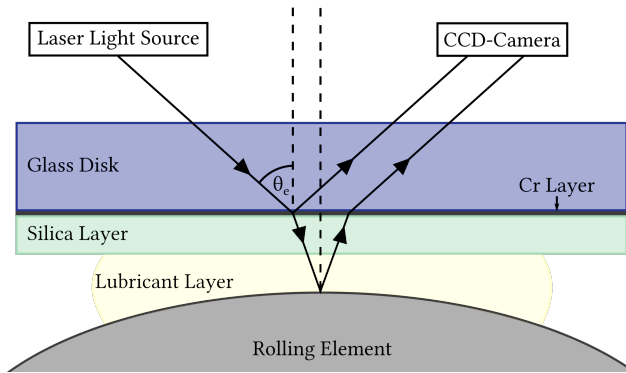
Figure 5.9.: Simplified representation of the formation of an interference pattern in the lubrication gap between the coated glass disc and the rolling element, based on the concept described in [105]. Here, θ_e stands for the angle of incidence.

Figure 5.10 (top) illustrates an example of the interference image of a lubricant-free contact between the glass disc and the rolling element at a load of 45 N under which a contact with a diameter of approx. 380 μm is formed. In the bottom part of the figure, a simplified side view sketch of the contact between the glass disc and the rolling element is presented. Although not drawn to scale, it demonstrates how the gap height between the contact partners is related to the interference pattern and the increasing orders of intensity maxima and minima in the interference image.

5.4. Greases

This chapter focuses on the greases used in the experiments conducted for this study. The greases can be categorized into three clusters:

- Industrial Series (IS): These are fully additivated greases commonly used in industrial applications. Section 5.4.1 provides detailed information about these greases and their properties.

- Model Series I (MS_I): Special model greases were formulated to investigate the influence of specific grease properties on wear and
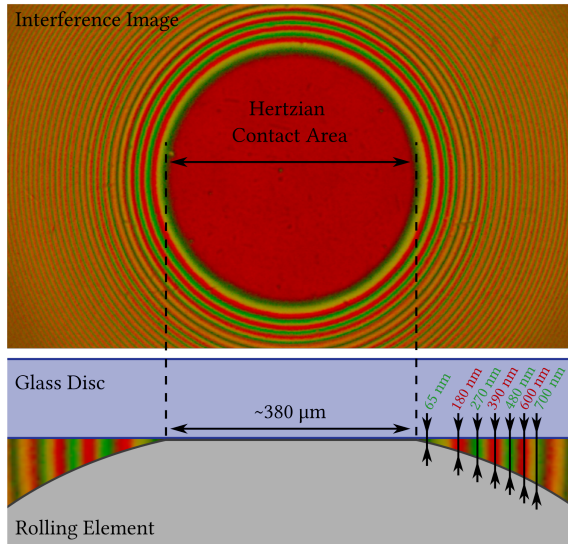
Figure 5.10.: Example of an interference image for a lubricant-free contact between the rolling element and the glass disc. The upper image displays the interference pattern as captured by the CCD sensor from a top-view perspective. The lower image demonstrates the correlation between the ascending order of interference rings and the increasing separation distance between the disc and the rolling element.

replenishment behavior. These greases are unadditivated and consist of lithium thickener and synthetic polyalphaolefin (PAO) base oil. While the chemical composition of these greases remained the same, the viscosity of the base oil and the bleeding behavior (base oil content) were altered. More information about this model series can be found in 5.4.2.

- Model Series II (MS_{II}): This model series was designed to study the effects of different thickeners, base oil types, and grease consistency. For more details on this model series, refer to 5.4.3.

Additionally, two other greases were investigated, as mentioned in section 5.4.4.

The oil separation rates of the greases were determined using the IP-121 method at 168 hours and 40° C [106] and with the same method at 20° C. The base oil viscosity at 40° C was determined according to ASTM-D 445 [7] for the model greases, while for the industrial greases, the values were taken from the respective data sheets. To determine the viscosity values at 20° C, the method according to Ubbelohde-Walther from DIN 51563 [29] was employed. The kinematic viscosities of the base oils at 40° C and 100° C before admixture to the greases were taken and converted to the dynamic viscosity with the corresponding density. In the case of industrial greases that had only one set of viscosity and temperature values available, the dynamic base oil viscosity at 20° C of the bled base oil was determined using a shear rheometer in plate-plate arrangement. The NLGI class of the model greases was determined using worked penetration (P60) with cone penetration according to ASTM D-217 (or ASTM D-1403) [5, 4]. For the consistency values of the industrial greases, the NLGI classes from the data sheets are shown in parentheses. If available, the measured values according to ASTM D-217 are provided without parentheses.

5.4.1. Industrial Greases (IS)

Five distinct types of industrial greases, specifically formulated for application in wind turbine pitch bearings, were chosen for analysis. The essential grease parameters relevant to this study are outlined in Table 5.4.1. Some parameters, such as the surface tension of the base oil, remain undetermined due to the scope of this research, and thus have been approximated. These specific parameters are indicated in Table 5.4.1 along with appropriate explanatory notes. Notably, the greases exhibit variations in chemical composition, evident through diverse thickener and base oil selections, as well as distinct additive compositions. However, the study's primary focus revolves around key parameters including base oil viscosity, oil separation rate, and consistency, which display substantial differences among the greases. Particularly intriguing is the variance in base oil viscosity among the greases. For instance, certain greases opt for a lower base oil viscosity, such as IS1 with a value of $v = 50$ cSt and especially IS2 with $v = 13$ cSt. Conversely, other greases emphasize a higher base oil viscosity, exemplified by IS4 and IS5 with $v = 460$ cSt. Clear differences can also be seen in the oil separation rate, ranging from 1.7 % for IS5 to 6.1 % for IS2. Noteworthy variations in grease consistency are evident as well. However, it is important to acknowledge

Table 5.2.: Characteristics of the examined industrial greases (IS)

| Name | Gleitmo 585K | Rhodina BBZ | BEM 41-141 |
Designation	IS1	IS2	IS3
Thickener Type	Li	Ca	LiX
Base Oil Type	PAO	Mineral Oil	Mineral/ Synthetic Oil
Base Oil Viscosity ν at 40°C in cSt	50	13	130
Base Oil Viscosity η_0 at 40°C in Pas	0.042	0.011	0.108
Base Oil Viscosity η_0 at 20°C in Pas	0.086[1]	0.024[2]	0.374[2]
Surface Tension σ_s in 10^{-3} N/m at 20°C	30[3]	30[3]	30[3]
Oil Separation Rate O_{sr} at 40°C (IP 121)	0.04	0.061	0.053
Oil Separation Rate O_{sr} at 20°C (IP 121[4])	0.026	0.061	0.034
NLGI Grade (Data Sheet)	2	1-2	1

| Name | Mobil SHC 460 wt | Stabyl Lx 460 |
Designation	IS4	IS5
Thickener Type	LiX	LiX
Base Oil Type	PAO	Synthetic Oil
Base Oil Viscosity ν at 40°C in cSt	460	460
Base Oil Viscosity η_0 at 40°C in Pas	0.382	0.382
Base Oil Viscosity η_0 at 20°C in Pas	1.767[1]	1.266[1]
Surface Tension at 20°C σ_s in 10^{-3} N/m	30[3]	30[3]
Oil Separation Rate O_{sr} at 40°C (IP 121)	0.022	0.017
Oil Separation Rate O_{sr} at 20°C (IP 121[4])	0.012	0.007
NLGI Grade (Data Sheet)	1.5	1.5

[1] Determined in plate-plate shear rheometer
[2] Calculation according to DIN 51563 [29]
[3] Assumption as exact measurements are not available.
[4] Measurement setup according to IP 121 [106] but at 20° C instead of 40° C

that disparities occasionally arise between measured worked penetration values following ASTM-D1430 and the consistency values provided in the corresponding data sheet. The results obtained with the industrial greases can be found in Section 6.1 as well as in Section 6.1.2, Section 6.2.1, Section 6.3.1 and Section 6.3.2.

5.4.2. Model Greases Series I (MS$_I$)

Grease MS$_I$1 is formulated with a base oil of low viscosity, characterized by a base oil viscosity of ν = 19 cSt. Meanwhile, grease MS$_I$2 employs the same

Table 5.3.: Characteristics of the examined greases of model series I (MS$_1$)

Designation	MS$_I$1	MS$_I$2	MS$_I$3
Thickener Type	LiX	LiX	LiX
Base Oil Type	93.7% PAO/ 6.3% Ester	93.7% PAO/ 6.3% Ester	93.7% PAO/ 6.3% Ester
Base Oil Viscosity ν at 40℃ in cSt	19	19	1067
Base Oil Viscosity η_0 at 40℃ in Pas	0.0171	0.0171	0.9603
Base Oil Viscosity η_0 at 20℃ in Pas	0.034[1]	0.034[1]	3.102[1]
Surface Tension σ_s in 10^{-3} N/m at 28℃	28.54	28.54	31.16
Oil Separation Rate O_{sr} at 40℃ (IP 121)	0.007	0.051	0.012
Oil Separation Rate O_{sr} at 20℃ (IP 121[2])	0.005	0.026	0.008
Pen60 1/2-scale at RT in 10^{-1} mm	276	317	276
NLGI Grade	2	1	2

[1] Calculation according to DIN 51563 [29]
[2] Measurement setup according to IP 121 [106] but at 20° C instead of 40° C

base oil, yet its base oil content has been augmented by 20%. This modification causes a transition from NLGI class 2 to 1, accompanied by an elevation in the oil separation rate O_{sr} from 0.7% to 5.1%. The ensuing Section 6.1 elucidates the impact of increased base oil content on wear behavior across variable oscillation parameters, utilizing these representative model greases. In contrast, grease MS$_I$3 has a base oil with significantly augmented viscosity, registering $\nu = 1067$ cSt compared to MS$_I$1. However, the consistency of these greases remains similar, as evidenced by the congruent worked penetration values $Pen60(\text{MS}_I1) = Pen60(\text{MS}_I3) = 27.6$ mm. Correspondingly, the oil separation rates for both greases are of comparable magnitude, ranging between 0.7% and 1.2% respectively. In Section 6.1.2, experimental investigations on the influence of base oil viscosity on wear initiation are undertaken using these specific greases. It's worth noting that similar greases have previously undergone testing in fretting conditions by LARSSON ET AL. and PRESILLA ET AL. as documented in their works [65, 66, 89].

5.4.3. Model Greases Series II (MS$_{II}$)

Model series II also comprises unadditivated greases. The principal objective of experimental investigations involving greases from model series II is to ascertain the impact of parameters such as base oil viscosity, oil separation

rate, consistency, and the chemical composition of the greases. To achieve this goal, a set of twelve greases ($MS_{II}1$ - $MS_{II}12$) has been formulated for this model series. This formulation incorporates two distinct types of thickeners: Lithium (Li) and anhydrous Calcium (Ca), along with two varying base oil types: Polyalphaolefin (PAO) and Ester (EST). These components are combined to yield Li-PAO, Li-EST, Ca-PAO, and Ca-EST greases. Three sub-series of greases are generated from these combinations, which are outlined in Table 5.4 across their corresponding rows. Greases $MS_{II}1 - MS_{II}4$ featured in the upper portion of the table are categorized as NLGI class 2.5 greases, displaying a relatively modest oil separation rate within the range of 0.8%-2.0%. The succeeding set, $MS_{II}5 - MS_{II}8$ situated in the middle part of the table, share the same base oil as $MS_{II}1 - MS_{II}4$, characterized by a PAO-oil with a viscosity of $\nu = 18$ cSt and an EST-oil with a viscosity of $\nu = 17$ cSt. However, they are adjusted to an NLGI class of 1.5, leading to an increased oil separation rate of $3.0 - 3.9\%$. Subsequently, the $MS_{II}9 - MS_{II}12$ greases, located in the lower segment of the table, are developed by admixing additional oils with notably low viscosities of $\nu = 5$ cSt to the PAO-oil and $\nu = 3.3$ cSt to the EST-oil of the $MS_{II}5 - MS_{II}8$ greases. Although the proportion of the additional base oil is relatively minor, resulting in a marginal divergence of the overall base oil viscosity, it is hypothesized that the low-viscosity component of the mixture will bleed out first during testing. A comparison of the oil separation rates between the $MS_{II}5 - MS_{II}8$ and $MS_{II}9 - MS_{II}12$ greases reveals a notable increase in the oil separation rate across three out of four cases due to the admixture of the low-viscosity base oil. The outcomes from component tests conducted with the model series II greases are documented in Section 6.1.2, whereas the findings from model tests performed on the EHL-Tribometer employing the corresponding greases can be found in Section 6.2.2.

Table 5.4.: Characteristics of the examined greases of model series II (MS_{II})

Designation	$MS_{II}1$	$MS_{II}2$	$MS_{II}3$	$MS_{II}4$
Thickener Type	Li	Li	Anh-Ca	Anh-Ca
Base Oil Type	PAO	EST	PAO	EST
Base Oil Viscosity v at 40°C in cSt	18	17	18	17
Base Oil Viscosity η_0 at 40°C in Pas	0.0148	0.0155	0.0148	0.0155
Base Oil Viscosity η_0 at 20°C in Pas	0.0328[1]	0.033[1]	0.0328[1]	0.033[1]
Surface Tension σ_s in 10^{-3} N/m	28.85	25.52	28.85	25.52
Oil Separation Rate O_{sr} at 40°C (IP 121)	0.019	0.008	0.01	0.02
Oil Separation Rate O_{sr} at 20°C (IP 121[2])	0.01	0.002	0.004	0.008
Pen60 1/2-scale at RT in 10^{-1} mm	266	253	266	253
NLGI Grade	2.5	2.5	2.5	2.5

Designation	$MS_{II}5$	$MS_{II}6$	$MS_{II}7$	$MS_{II}8$
Thickener Type	Li	Li	Anh-Ca	Anh-Ca
Base Oil Type	PAO	EST	PAO	EST
Base Oil Viscosity v at 40°C in cSt	18	17	18	17
Base Oil Viscosity η_0 at 40°C in Pas	0.0148	0.0155	0.0148	0.0155
Base Oil Viscosity η_0 at 20°C in Pas	0.0328[1]	0.033[1]	0.0328[1]	0.033[1]
Surface Tension in 10^{-3} N/m at 28°C	28.85	25.52	28.85	25.52
Oil Separation Rate O_{sr} at 40°C (IP 121)	0.03	0.037	0.039	0.03
Oil Separation Rate O_{sr} at 20°C (IP 121[2])	0.03	0.018	0.033	0.021
Pen60 1/2-scale at RT in 10^{-1} mm	305	304	312	311
NLGI Grade	1.5	1.5	1.5	1.5

Designation	$MS_{II}9$	$MS_{II}10$	$MS_{II}11$	$MS_{II}12$
Thickener Type	Li	Li	Anh-Ca	Anh-Ca
Base Oil Type	PAO	EST	PAO	EST
Base Oil Viscosity v at 40°C in cSt	14	10	12	13
Base Oil Viscosity η_0 at 40°C in Pas	0.015	0.009	0.012	0.010
Base Oil Viscosity η_0 at 20°C in Pas	0.0216[1]	0.016[1]	0.0168[1]	0.0237[1]
Surface Tension in 10^{-3} N/m	28.85	25.52	28.85	25.52
Oil Separation Rate O_{sr} at 40°C (IP 121)	0.037	0.053	0.04	0.028
Oil Separation Rate O_{sr} at 20°C (IP 121[2])	0.025	0.017	0.025	0.019
Pen60 1/2-scale at RT in 10^{-1} mm	305	303	306	304
NLGI Grade	1.5	1.5	1.5	1.5

[1] Calculation according to DIN 51563 [29]
[2] Measurement setup according to IP 121 [106] but at 20° C instead of 40° C

Table 5.5.: Characteristics of the examined other greases (O)

Name	Tribol GR 100-1 PD	MSD70
Designation	O1	O2
Thickener Type	Li	Li
Base Oil Type	Mineral	Mineral Oil
Base Oil Viscosity v at 40°C in cSt (data sheet)	100	100
Base Oil Viscosity η_0 at 40°C in Pas (data sheet)	0.0833	0.0833
Base Oil Viscosity η_0 at 40°C in Pas (bled oil)	0.1333	0.085
Base Oil Viscosity η_0 at 20°C in Pas (bled oil)	0.4767[1]	0.2797[1]
Surface Tension in 10^{-3} N/m	30[2]	30[2]
Oil Separation Rate O_{sr} at 40°C (IP 121)	0.106	0.071
Oil Separation Rate O_{sr} at 20°C (IP 121[3])	0.065	0.043
NLGI Grade (data sheet)	1	1

[1] Determined in plate-plate shear rheometer
[2] Assumption as exact measurements are not available.
[3] Measurement setup according to IP 121 [106] but at 20° C instead of 40° C

5.4.4. Other Greases (O)

This section highlights two greases that exhibit remarkable similarities in the properties outlined on their respective data sheets. Nonetheless, notable disparities in performance emerged during the oscillating bearing tests conducted. Table 5.5 provides a compilation of both the base oil viscosity values as presented on the data sheet and the empirically measured values of the seeped base oil. In the case of grease O2, there exists minimal contrast between the stated viscosities and the measured values. Conversely, for grease O1, the viscosity of the bled base oil surpasses the data sheet value by a substantial 60%. Additionally, the bled base oil from grease O1 displays non-Newtonian behavior, whereas the bled base oil from O2 keeps its Newtonian characteristics. These observations suggest the possible presence of polymers in the base oil of O1, increasing the viscosity of the bled base oil [101]. Both greases undergo thorough examination in Section 6.1.2 and are further subjected to investigation within the context of Section 6.3.3.

6. Experimental results

This chapter begins with a detailed parameter study involving angular contact ball bearings, delving into the influence of key operational parameters such as oscillation amplitude (θ), oscillation frequency (f), contact pressure (p), and the number of cycles (N) on the initiation of wear in oscillating rolling bearings (Section 6.1). Subsequently, the results obtained by varying the lubricant are detailed in Section 6.1.2. Specific component and model tests shed light on the underlying lubrication mechanisms. In Section 6.2, the results stemming from the investigations into base oil reflow are presented. Section 6.3 presents the findings of the investigations into the influence of the bearing cage on contact lubrication. Furthermore, Section 6.4 showcases the outcomes of supplementary investigations encompassing diverse areas of interest, including the examination of hybrid bearings, among other aspects.

6.1. Parameter Study

Within this section, a comprehensive presentation of rolling bearing test results is provided, aiming to discern the impact of diverse operational and grease parameters on wear initiation in oscillating rolling bearings. Section 6.1.1 presents the results from investigations into operating parameters, with specific focus on oscillation frequency, oscillation amplitude/amplitude ratio, load, and the number of cycles. In parallel, Section 3.3 delves into the results concerning the influence of grease-related parameters, including attributes such as oil separation rate, base oil viscosity, base oil type, and the type of thickener utilized.

6.1.1. Operating Parameters

Oscillation frequency and amplitude

To investigate the influence of oscillation frequency (f) and oscillation angle (θ) on wear initiation, experiments are conducted at a constant number of 4 000 oscillation cycles while varying the parameters f and θ. The specific values of the investigated parameters are provided in Table 6.1. It is important to highlight that the test subjects were unsealed 7208-type bearings, each containing 10 ml of grease, corresponding to 100% filling [62]. Before the tests, the bearings were rotated for 20 revolutions at 10 rpm. In consideration of the unsealed nature of the bearings, lubricating grease has the potential to exude from the bearing during both the initial running-in phase and the subsequent testing phase. Consequently, the prevailing conditions may not be directly comparable to those exhibited by a sealed bearing with complete (100%) lubricant filling.

Table 6.1.: Operating Parameters for the study of the influence of oscillation frequency f and amplitude θ.

Parameter	Value	Unit
Bearing Type	7208	-
max. Contact pressure p_{max}	2	GPa
Oscillation frequency f	0.2, 1, 3, 5	Hz
Oscillation amplitude θ	1, 7, 15, 30, 45	°
Amplitude ratio e_{or}	1, 4, 8, 16 , 24	-
Grease Type	IS1	-
Grease Amount	10 (100% filling) [62]	ml
Sealing	none	-

The plots depicting the maximum torque experienced per oscillation cycle are presented in Figure 6.1 for all examined parameter configurations. In the upper plot, the curves illustrate tests conducted at a frequency of 0.2 Hz with varying oscillation angles: $\theta = 2, 7, 15, 30$, and 45°. The curves corresponding to distinct oscillation angles are distinguished by different colors. Notably, regardless of the oscillation angle, all torque curves form a nearly horizontal line at a torque value of approximately 1.5 Nm. Upon observing the curves for a frequency of 1 Hz, it is apparent that most curves in this set also maintain an almost horizontal trajectory. However, the test conducted at $\theta = 15°$ displays a sharp surge starting around cycle number $N \approx 1\,000$ cycles. By the end of the experiment, the torque in this case rises to a level exceeding 8 Nm,

approximately 4.5 times the initial torque. A similar trend is observed for a frequency of 3 Hz, where pronounced torque escalation occurs not only at an angle of $\theta = 15°$ but also at $\theta = 7°$. In the context of $f = 5$ Hz, distinct increases in torque are noted at $\theta = 7°$ and $\theta = 15°$. Furthermore, there appears to be a torque rise at $\theta = 30°$. To facilitate a comprehensive overview of the experimental outcomes, a color map is presented in Figure 6.2. The vertical axis of the map depicts the oscillation angle, while the horizontal axis represents the oscillation frequency. The color scale signifies the maximum torque values achieved, i.e., the peaks of the curves depicted in Figure 6.1, and is indicated by the accompanying color bar. Dark blue indicates higher torque values, whereas light yellow represents lower values. Additionally, the color bar provides friction values calculated according to Section 3.2.4. The parameter combinations subjected to testing are denoted by black triangles within the color map. To ensure good visual clarity, torque values between tests are linearly interpolated.

Evidently, a distinct region characterized by an increased torque emerges within the scope of medium amplitude ratios coupled with high frequencies. In the case of the smallest amplitude ratio investigated ($e_{or} = 1$), no discernible torque increase is observed across the entire frequency spectrum examined, which spans from 0.2 to 5 Hz. For the subsequent larger amplitude ratio ($e_{or} = 4$), the experiments already show a notable increase in torque at higher frequencies (3 Hz, 5 Hz). This range of increased torque extends towards lower frequencies (1 Hz) when the amplitude ratio reaches $e_{or} = 8$. A further increase in the amplitude ratio prompts a displacement of the heightened torque range towards higher frequencies once again. Beyond an amplitude ratio of $e_{or} = 24$, no appreciable increase in torque is noticeable throughout the entirety of the frequency spectrum.

To establish the reproducibility of torque curves across diverse parameter configurations, two additional replicate tests are conducted at distinct parameter combinations. Figure 6.3 illustrates the three torque curves corresponding to each of the following parameter combinations: $f = 1$ Hz, $\theta = 15°$ (top); $f = 3$ Hz, $\theta = 7°$ (middle); and $f = 3$ Hz, $\theta = 30°$ (bottom). The presented experiments are carried out using both grease IS1 (green) and grease IS2 (blue), with the latter demonstrating contrasting behavior at the examined data points.

By conducting an optical analysis of the raceway surface and subsequently evaluating its visual characteristics, a distinct correlation between damage

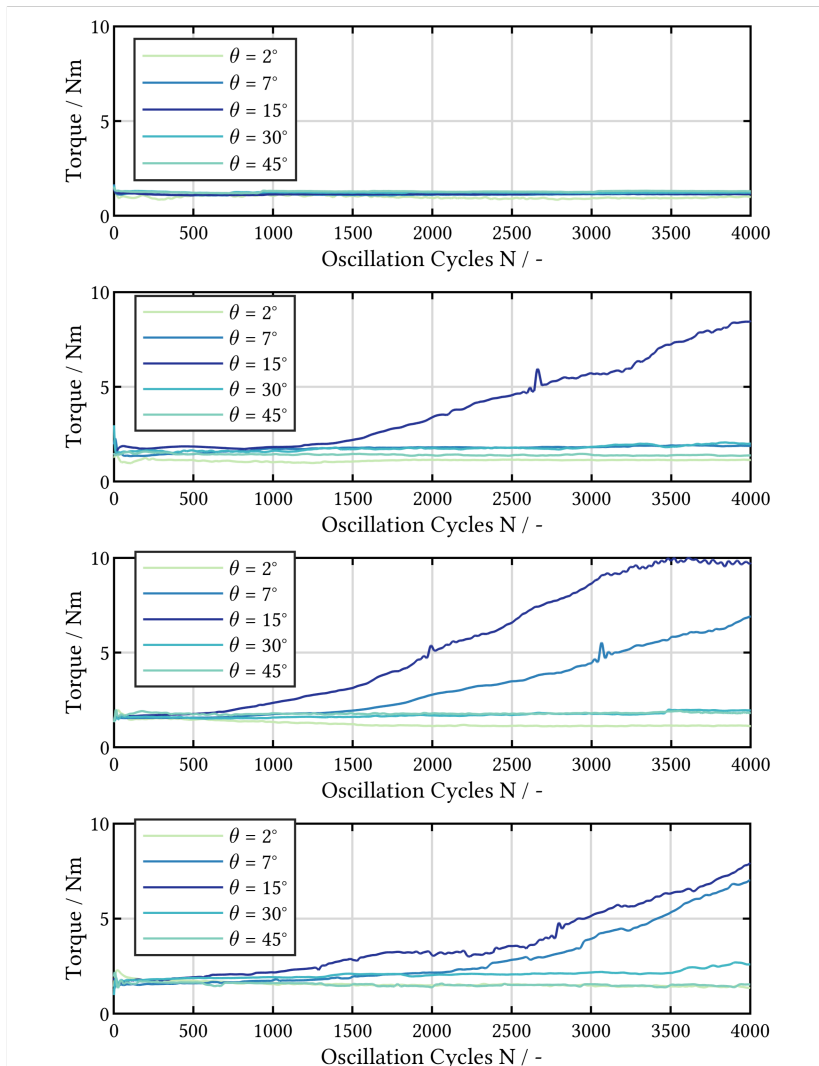**Figure 6.1.:** The diagram illustrates the plots depicting the maximum torque per oscillation cycle obtained from experiments employing industrial grease IS1. The oscillation amplitudes are varied as $\theta = 2, 7, 15, 30, 45°$, and the oscillation frequencies are set at $f = 0.2$ Hz (top row), $f = 1$ Hz (second row), $f = 3$ Hz (third row), and $f = 5$ Hz (bottom row), as detailed in [111].
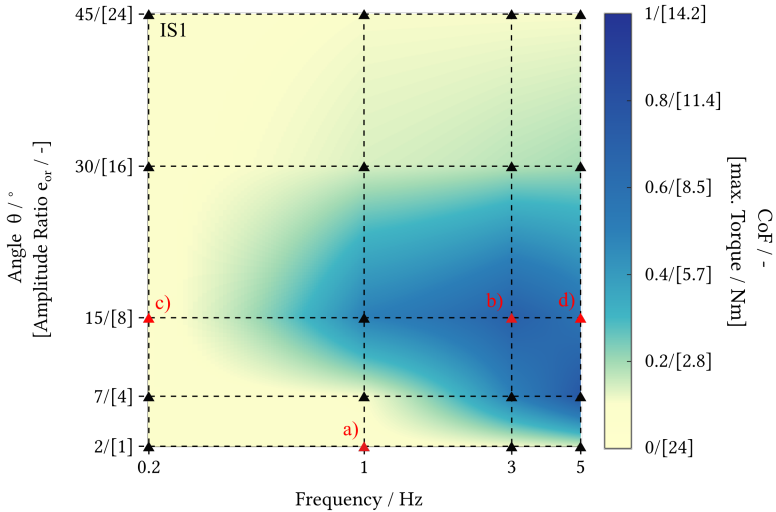
Figure 6.2.: Plot of maximum torques or CoF during oscillating bearing tests at different parameter combinations of oscillation frequency f and oscillation angle θ or amplitude ratio e. Test data points are indicated using triangular markers. The visualization of maximum torque or CoF values is achieved through color representation, with linear interpolation applied between the test points. The maximum contact pressure is 2 GPa, and the grease used is IS1 [111].

patterns and torque can be established. Figure 6.4 presents images of the raceway surface under four different parameter combinations, which are denoted by red triangles in Figure 6.2. The tests corresponding to Figures a) and c) of Figure 6.4 reveal no significant torque increase. Consequently, the optical images display no observable damage to the raceway. Conversely, the experiments associated with Figures b) and d) of Figure 6.4 exhibit a notable torque escalation. In these instances, the raceway surface experiences pronounced damage, characterized by a rough appearance due to micro pits and discoloration arising from corrosion byproducts, both of which are distinctly visible.

To establish a connection between the escalating coefficient of friction and raceway surface damage, a qualitative assessment of the damage is conducted using a grading system reminiscent of school grades, coupled with an associated color scheme.
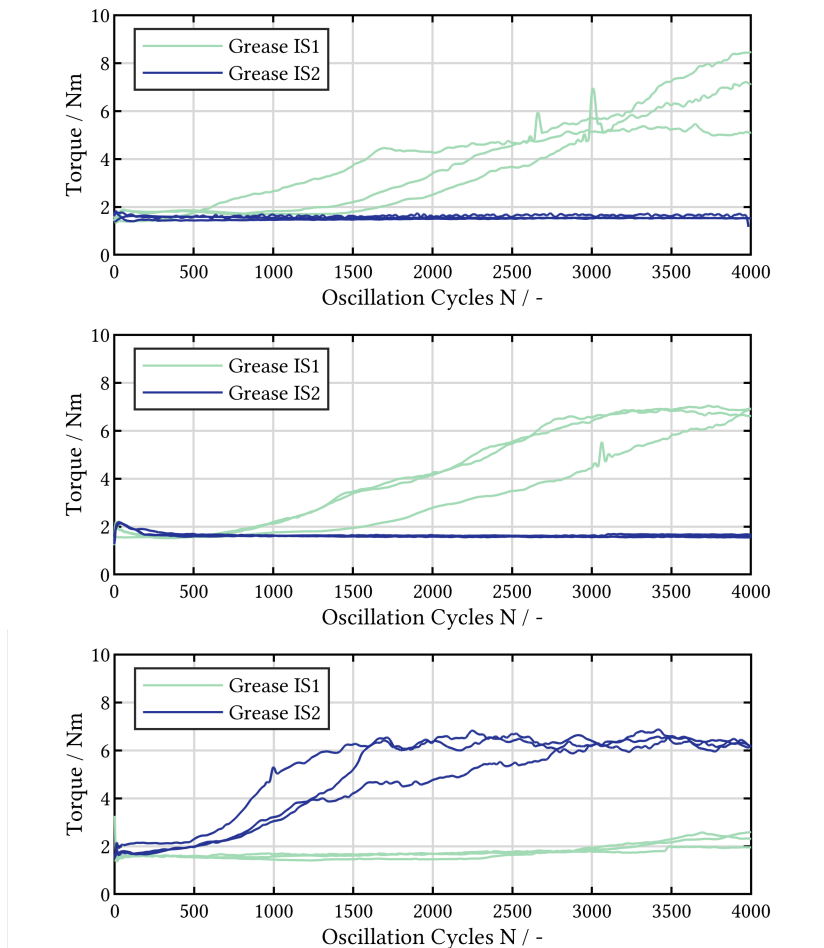
Figure 6.3.: Replicate experiments for the parameter combinations $f = 1\,\text{Hz}$, $\theta = 15°$ (top), $f = 3\,\text{Hz}$, $\theta = 7°$ (middle), and $f = 3\,\text{Hz}$, $\theta = 30°$ (bottom) using the studied greases IS1 (green) and IS2 (blue) [111].

The evaluation pertains exclusively to the load-side bearing. However, the bearings on both sides usually have a very similar damage pattern. Within this framework, individual damage instances on the raceways of the inner
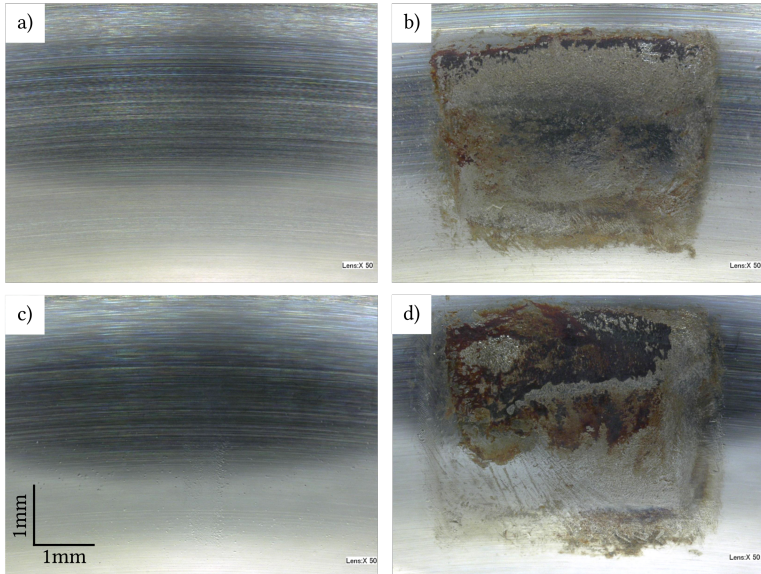
Figure 6.4.: Digital microscope images showcasing the raceway surface of both undamaged bearings, represented by images (a) and (c), and damaged bearings, depicted by images (b) and (d) [111].

and outer rings are assigned school grades, categorized as '1-undamaged', '3-initial damage', and '6-severe damage'. A grade of 1 indicates an absence of visible damage on the specific raceway segment, implying the absence of both corrosive products and micro pits. In Figure 6.5, such a segment is depicted in light yellow. If smaller portions of the over-rolled surface exhibit indications of corrosion, the segment is assigned a grade of 3, and represented in turquoise. If the over-rolled segment is entirely compromised, displaying corrosive products and micro pits, a grade of 6 is assigned, and the corresponding segment is rendered in dark blue. In Figure 6.4, the load-side bearing for each investigated parameter combination is depicted in gray, oriented relative to the direction of gravity (g). The damage severity grades are visually conveyed as colored segments positioned on the inner and outer rings. A comparison between the coefficient of friction color map in Figure 6.2 and the damage assessment in Figure 6.5 underscores a clear direct correlation

between the two. The evaluation of damage grades reveals that bearing raceways exhibit minimal damage at an amplitude ratio of $e = 1$. At an amplitude ratio of $e = 4$, the region prone to damage expands, mirroring the depiction in Figure 6.2, extending down to a frequency of $f = 1\,\text{Hz}$. For the highest amplitude ratio investigated, $e = 24$, raceway damage is virtually absent. Figure 6.5 demonstrates that raceway damage occurs symmetrically across both inner and outer raceways. Furthermore, it becomes evident that damage is uniformly distributed around the bearing's circumference. The relationship between the calculated coefficient of friction and the extent of damage is similarly observed for the other investigated lubricants. As a result, subsequent test analyses primarily rely on torque evaluation or the corresponding calculated coefficient of friction.
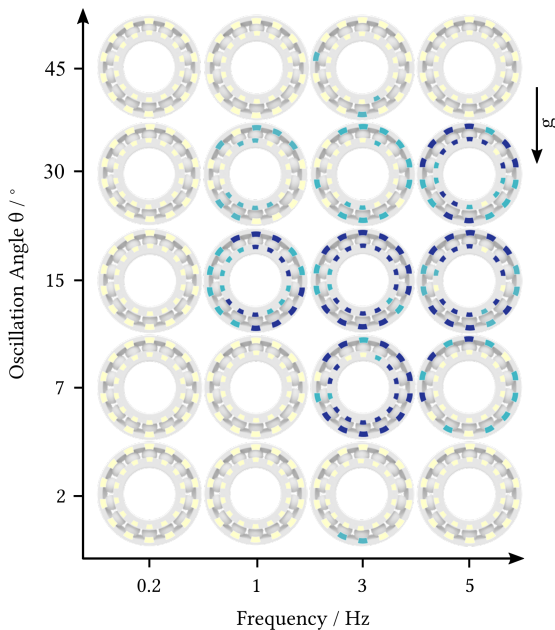
Figure 6.5.: Qualitative evaluation of the damage extent observed in the examined bearings under various operational conditions utilizing grease IS1, as documented in [111].

Temperature

Throughout the experimental trials, temperature measurements were taken on both the outer ring of the bearing and the surrounding environment using platinum resistance thermometers with 100 Ohm Resistance (PT100) sensors. Figure 6.6 illustrates the recorded average temperatures in relation to the operational parameters. The left panel shows the outer ring temperatures, while the right panel displays the ambient temperatures. Notably, the temperature difference between the outer ring and the ambient environment remains minimal, with just a few degrees Celsius across all cases. The calculated average outer ring temperature does not exceed 22.7° C. This result indicates that the heat input from dissipated friction energy is insufficient to cause a significant temperature increase in the test setup. This consistent thermal behavior has been observed in all bearing tests conducted within this study.
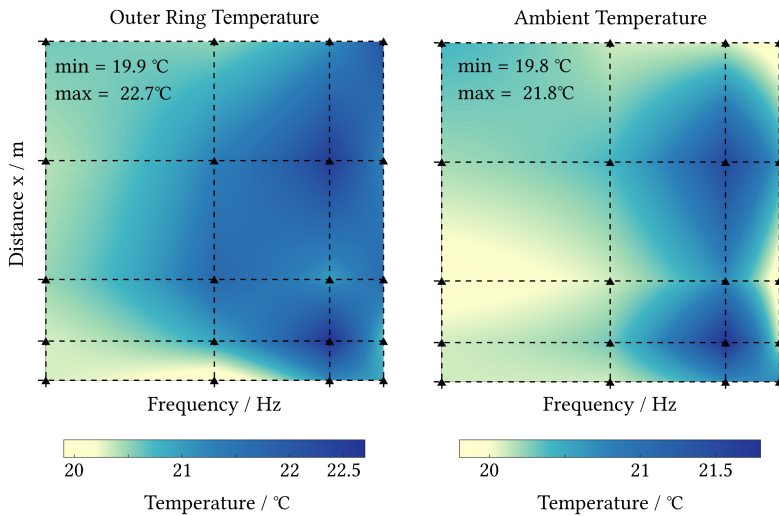
Figure 6.6.: Outer ring (left) and ambient (right) temperatures as a function of the operating parameters. Test data points are indicated using triangular markers. The visualization is achieved through color representation, with linear interpolation applied between the test points.

Contact pressure

The presented results thus far show the foundational impact of the operating parameters, oscillation frequency, and oscillation amplitude (or amplitude ratio). Figure 6.7 illustrates the findings derived from assessing the maximum friction values under varying maximum contact pressures, denoted as p_{max}. The upper, middle, and lower color maps correspond to p_{max} values of 1.5 GPa, 2 GPa, and 2.5 GPa, respectively. The parameter matrices for the distinct load steps remain consistent in terms of oscillation angle (θ = 2, 7, 15, 30, 45°), frequency (f = 0.2, 1, 3, 5 Hz), and oscillation cycles (N = 4 000). Upon comparing the friction coefficient results between investigations at p_{max} = 1.5 GPa and p_{max} = 2 GPa, a clear trend emerges: the damage-critical region becomes notably more pronounced at higher contact pressures. For instance, the friction values from tests conducted at an oscillation frequency of f = 1 Hz display minimal friction coefficient increase at p_{max} = 1.5 GPa across all amplitude ratios. Conversely, at p_{max} = 2 GPa, a conspicuous friction coefficient increase is observable, particularly at an oscillation angle of θ = 15°. Overall, the maximum coefficients of friction attained within the damage-critical range are significantly lower at p_{max} = 1.5 GPa in comparison to p_{max} = 2 GPa. Transitioning to the subsequent load increment, from p_{max} = 2 GPa to p_{max} = 2.5 GPa, the visual alterations in the color map are less pronounced. In fact, the friction coefficient at the parameter combination of f = 1 Hz and θ = 7° demonstrates a minor decrease. However, as amplitude ratios grow larger (θ = 30°), the damage-critical area expands. The investigations into load variation highlight a tendency for the damage-critical zone to widen with increasing pressure while maintaining a constant cycle count. An intriguing observation is that the most critical amplitude ratio for damage initiation seems to be θ = 15°, irrespective of the applied load. In this context, "most critical for damage initiation" signifies that the damage-critical range extends to lower frequencies most extensively at this specific ratio.

Oscillation cycles

The previous tests have maintained a constant cycle count of N = 4 000 oscillation cycles. In an effort to estimate wear progression over extended test durations, tests with a tenfold increase in oscillation cycles (N = 40 000 cycles) are presented below, spanning various parameter combinations. Subsequently, a wear-critical assessment is undertaken over a test duration of N = 160 000 cycles, facilitating both qualitative and quantitative evaluation
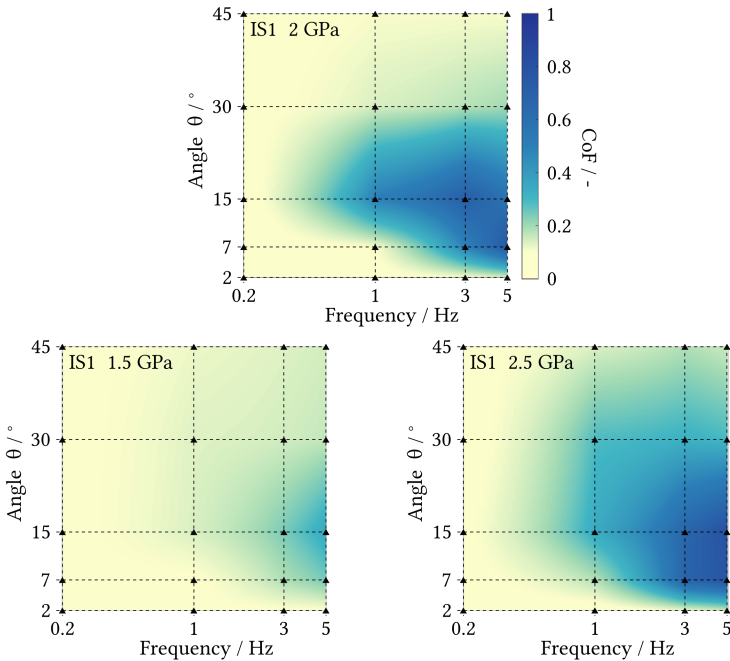
Figure 6.7.: CoF maps for grease IS1 with varying contact pressures of 1.5 GPa, 2 GPa and 2.5 GPa.

of wear development. First, the results of three tests are showcased, each originating from non-damaging regions of the 2 GPa test matrix (see Figure 6.8). The first test encompasses a small oscillation angle of $\theta = 2°$ at $f = 3$ Hz — well below the oscillation angle previously identified as susceptible to early wear. The second test involves the most damage-prone oscillation angle of $\theta = 15°$ but at the smallest frequency of 0.2 Hz, a parameter combination previously free of damage indications. The third test explores oscillation angles of $\theta = 30°$, $45°$, and $60°$ at $f = 3$ Hz — beyond the oscillation angle that appeared to encourage wear, as indicated by prior findings.

Indeed, these parameters outline the damage critical area. An examination of the curves of the friction coefficients shows that even after 40 000 cycles no damage occurs in the previously undamaged areas for the test at $\theta = 2°$, $f = 3$ Hz and $\theta = 15°$, $f = 0.2$ Hz. However, in the case of an increased
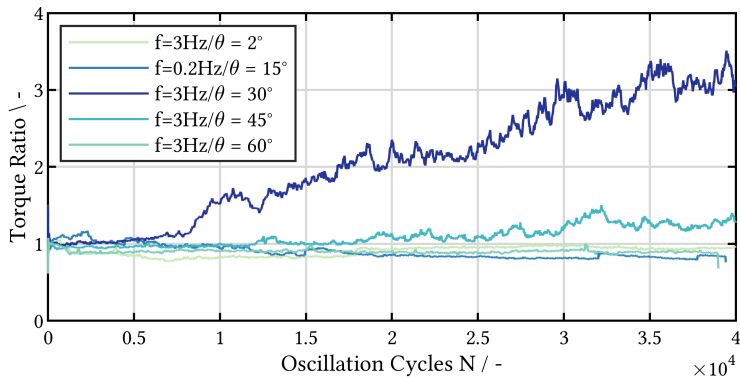
Figure 6.8.: The figure illustrates the torque ratio per oscillation cycle obtained from experiments utilizing industrial grease IS1. The parameter combinations considered are $\theta = 2°$ with $f = 3\,\text{Hz}$, $\theta = 15°$ with $f = 0.2\,\text{Hz}$, $\theta = 30°$ with $f = 3\,\text{Hz}$, $\theta = 45°$ with $f = 3\,\text{Hz}$, and $\theta = 60°$ with $f = 3\,\text{Hz}$, all tracked over a period of $N = 40\,000$ cycles. The torque ratio is calculated as the quotient of the maximum torque per cycle to the mean torque during the initial 200 oscillation cycles.

oscillation angle, such as $\theta = 30°$ at $f = 3\,\text{Hz}$, torque escalation initiates after approximately 8 000 cycles, reaching torque ratios of up to 3.5. Specifically, at $\theta = 45°$ and $f = 3\,\text{Hz}$, a minor torque increase becomes apparent around the 20 000 cycle mark, albeit significantly smaller than that observed at $\theta = 30°$. Remarkably, at an angle of $\theta = 60°$, no further increase is observed at all. Within the explored parameter range, a plausible hypothesis emerges: for lower frequencies and smaller amplitude ratios, wear-critical conditions either prompt swift wear onset or remain wear-uncritical over an extended timeframe. However, in scenarios involving higher frequencies and larger amplitude ratios, the development of the damage-critical zone has not yet reached completion within the initial 4 000 oscillation cycles.

For the tests conducted at a lower contact pressure of $p_{\max} = 1.5\,\text{GPa}$, it becomes evident that the damage-critical region has not yet reached its full extent within the initial 4 000 cycles. In order to illustrate this behavior comprehensively, all tests were extended to a cycle count of 40 000. Figure 6.9 offers a comparison between the friction coefficient map at 4 000 cycles, as previously shown in Figure 6.7, and the friction map at 40 000 cycles. The

progression is visually apparent: the damage-critical area becomes more pronounced as the oscillation cycle count increases. Comparing the friction maps from the tests at 1.5 GPa and 40 000 cycles with those at 2 GPa and 2.5 GPa at 4 000 cycles, a noteworthy observation emerges. The damage-critical regions seem to encompass very similar parameter ranges. Consequently, it can be inferred that, particularly for higher contact pressures starting from 2 GPa, a near-steady state condition has likely already developed after 4 000 cycles. However, it is crucial to note that in the vicinity of the boundary of the damage-critical range — especially for larger oscillation angles in the range of $\theta = 30 - 60°$ — operational parameters may prove more critical than their representation within the 4 000-cycle color maps might suggest.
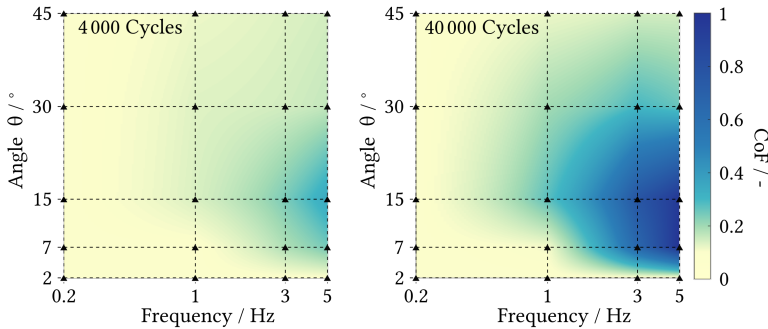
Figure 6.9.: Comparison of the friction maps at a contact pressure of 1.5 GPa after 4 000 cycles (left) and after 40 000 cycles (right)

Furthermore, an extensive sequence of tests was conducted to investigate the progression of damage for a critical parameter combination. To achieve this, all test parameters were held constant — except for the number of cycles ($\theta = 5°$, $f = 5$ Hz, $p_{max} = 2$ GPa). A single test was executed at each cycle count of $N = 1 000, 10 000, 20 000, 40 000, 80 000, 160 000$. Following each test, the bearings' raceways were evaluated utilizing digital microscopy and a laser scanning microscope to discern their topography, thereby enabling wear volume determination. The detailed methodology for wear assessment is explained in section 5.2. Figure 6.10 presents digital microscopic images illustrating representative instances of damage marks on the raceway surface at selected intervals within the test series (1 000, 20 000, and 160 000 cycles).

After the initial 1 000 cycles, signs of damage initiation become evident at specific contact points on both the inner and outer rings. Certain sections of the raceway surface traversed by the rolling element exhibit signs of roughening and discoloration, attributable to adhesion and tribo-corrosion.
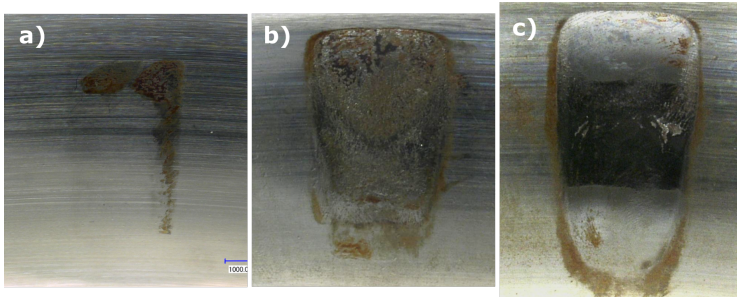
Figure 6.10.: Bearing raceway damage after 1 000 cycles (left), 20 000 cycles (middle), and after 160 000 cycles (right) in a test with $f = 5\,\text{Hz}$, $\theta = 7°$, and $p_{max} = 2\,\text{GPa}$ [112].

With increasing cycle count, the damage expands to encompass the entire contact region, manifesting around the circumference at each contact point. The central image in Figure 6.10 offers a representative picture of this condition after 20 000 oscillation cycles. These marks portray material chipping over the entire expanse, coupled with a surface that has become noticeably roughened. Additionally, areas exhibiting discoloration induced by tribo-corrosion are discernible. As the progression of damage unfolds, certain sections of the damage marks begin to undergo a smoothing process. After 160 000 cycles (as illustrated in Figure 6.10, rightmost depiction), the complete expanse of the damage marks acquires a polished mirror-like appearance. The images within Figure 6.10 attest that the dimensions of the marks expand as the cycle count rises. This expansion is a consequence of the gradual loss of material from the raceway surface. The magnitude of this mass loss can be computed for each contact area on both the inner and outer rings through topography measurements and the methodology detailed in section 5.2. The outcomes of this evaluation are presented in Figure 6.11.

Following 1 000 cycles, the majority of contacts are undamaged, with preliminary measurements indicating no measurable wear through the employed methodology. As a consequence, a wear volume of zero is assumed for all marks at this cycle count. Subsequent to 10 000 cycles, discernible damage marks begin to emerge on the outer ring, exhibiting measurable extents of
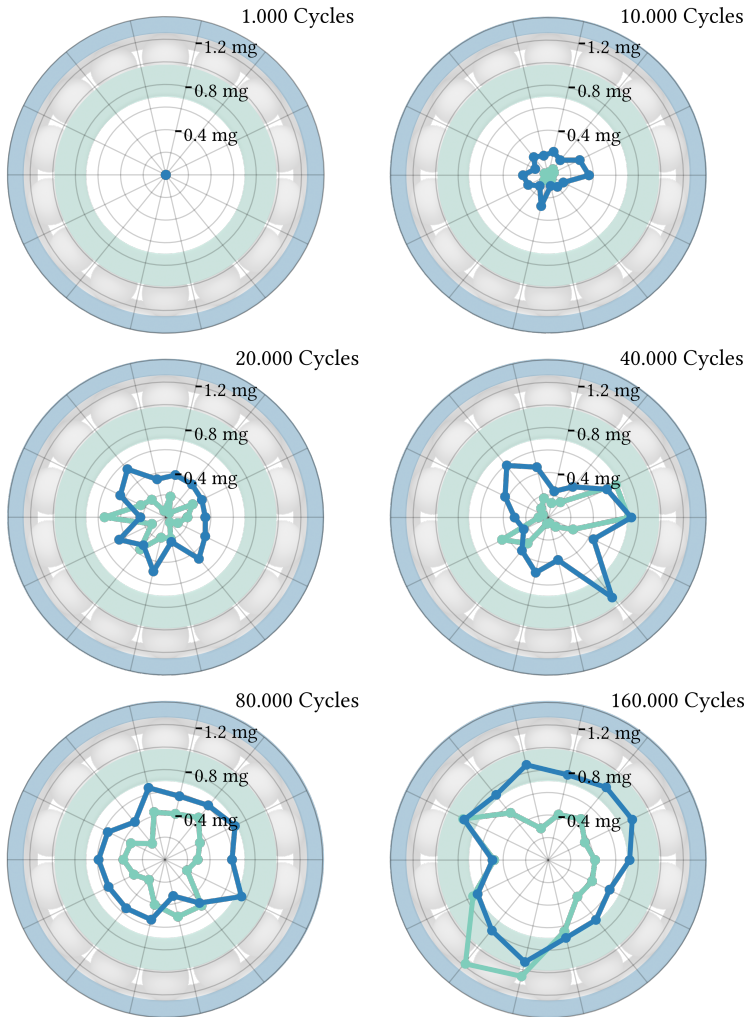
Figure 6.11.: Loss of mass per damage mark on the raceway of the inner and outer ring calculated from the wear volume for tests after 1 000, 10 000, 20 000, 40 000, 80 000, and 160 000 cycles in a test with $f = 5\,\text{Hz}$, $\theta = 7°$, and $p_{\text{max}} = 2\,\text{GPa}$.
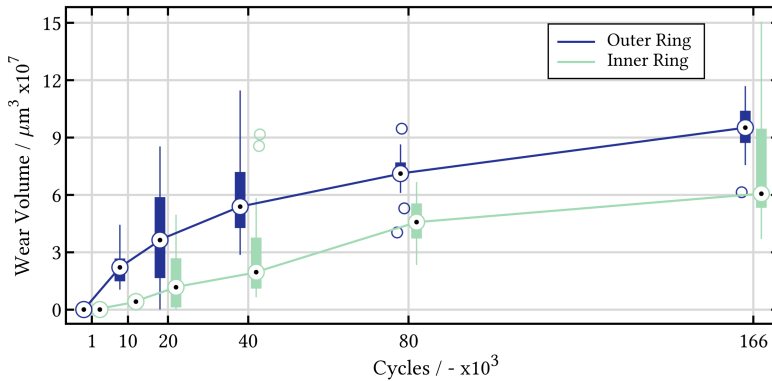
Figure 6.12.: Box plot of the mass loss per damage mark on the raceway of the inner and outer ring, calculated from the wear volume for tests after 1 000, 10 000, 20 000, 40 000, 80 000, and 160 000 cycles in a test with $f = 5\,\text{Hz}$, $\theta = 7°$, and $p_{max} = 2\,\text{GPa}$.

up to 0.4 mg per wear mark (depicted in dark blue). It is evident that wear is not consistently distributed across all marks. Upon reaching 40 000 cycles, a range of wear marks is observed on the outer ring, encompassing a spectrum of mass losses, with some marks recording over 0.9 mg and others registering only around 0.2 mg in mass loss. Figure 6.12 offers a graphical representation of the wear progression using a box plot. On the y-axis, the wear volume per mark is depicted in μm^3 above the corresponding cycle number on the x-axis. Results from measurements conducted on the outer ring are depicted in blue, while those from measurements on the inner ring are portrayed in green. A black dot within a white circle indicates the median of results at a specific cycle count. The ends of the thicker bars signify the 25% and 75% quantiles, the ends of the thinner bars represent the maximum and minimum values, and colored circles denote outliers. The median values are linearly interlinked. As observed in Figure 6.11, the uneven distribution of wear across marks is reflected in the noticeable scatter evident in the box plot. The median wear volume values for the outer ring follow a diminishing trend. After an initial steep rise in the curve between 1 000 and 20 000 cycles, the curve's progression levels off, maintaining almost linear growth between 80 000 and 160 000 cycles. Median values for the inner ring similarly exhibit a decreasing pattern. However, the slope of the median values for the inner ring is notably

gentler than that of the values for the outer ring, especially at lower cycle numbers. As cycle numbers increase, the slope of the inner ring's median values aligns with the slope of the outer ring's values.
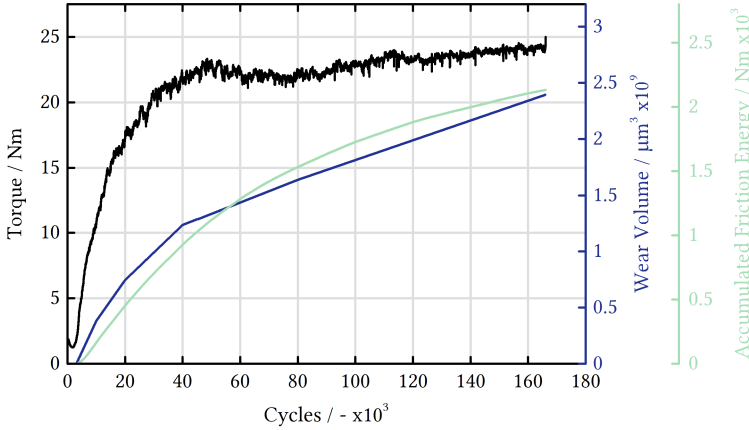
Figure 6.13.: Development of the maximum torque per wear mark (black), the raceway wear volume per bearing (dark blue) and the accumulation of friction energy over oscillation cycles (green) for a test at $f = 5\,\text{Hz}$, $\theta = 7°$, and $p_{max} = 2\,\text{GPa}$.

To establish a correlation between the measured wear volume and the recorded torque data, Figure 6.13 illustrates the progression of the maximum torque per oscillation cycle (depicted in black), the evolution of the raceway wear volume per bearing (inner and outer ring) linearly interpolated between the measured data points (displayed in dark blue), and the trajectory of accumulated frictional energy over the cycle count (shown in green). The curve representing the accumulated frictional energy is derived by summing up the areas enclosed by the torque loops, which correspond to the frictional energy $E_{d,i}$, over the cycle count n.

$$E_{d,n} = \sum_{i=1}^{n} E_{d,i} \tag{6.1}$$

The exact procedure was explained in more detail in Section 5.1.2 and in [27]. Observing the trajectory of the maximum torque, a distinctive pat-

tern emerges. After approximately 50 000 cycles, the curve reaches a local maximum, maintaining a nearly constant high level up to 160 000 cycles. Similarly, the course of the mass loss curve follows a degressive trend. In the initial phase, characterized by the development of surface roughness due to adhesive and corrosive damage, the wear curve experiences a steep ascent. Subsequently, as the wear marks begin to smoothen, the curve's rise levels off. This degressive pattern is also evident in the accumulated frictional energy curve, depicted in green in Figure 6.13. Intuitively, one might infer that the accumulated frictional energy would exhibit an almost linear increase from approximately 50 000 cycles, given the near-constant nature of the maximum torque. However, comprehending the degressive trend in accumulated frictional energy requires a closer examination of the torque loops. Figure 6.14 presents specific instances of these loops at cycle counts corresponding to the removal of bearings and determination of mass loss, among other stages of the test sequence.

Figure 6.14.: Development of the torque loops over the number of cycles (1 000, 5 000, 10 000, 20 000, 40 000, 80 000, 160 000 cycles) for a test at $f = 5\,\text{Hz}$, $\theta = 7°$, and $p_{max} = 2\,\text{GPa}$.

The torque loops over the oscillation angle are represented by various shades of green and blue in the hysteresis plots, ranging from light green for cycle 1 000 to dark blue for cycle 160 000. Notably, during the initial phase of the tests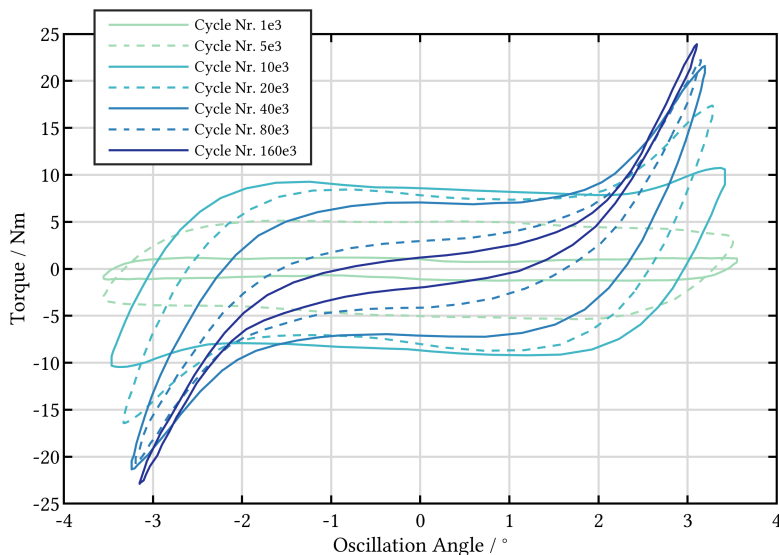, the torque hysteresis expands uniformly with increasing cycle count across the oscillation angle. This indicates an increase in the coefficient of friction across the entire swept raceway surface. As the cycle count progresses, distinctive peaks begin to materialize at the reversal points, which is particularly evident from cycle 10 000 onward. These peaks grow more prominent as the cycle count increases and the wear trough deepens. Concurrently, starting at cycle 20 000, there is no further widening of the hysteresis within the central region — between the reversal points. Subsequently, the middle part of the hysteresis gradually contracts over time. This shift contributes to both the degressive trajectory of the maximum torque and the cumulative dissipated frictional energy. The emergence of peaks at the reversal points in the hysteresis also coincides with the observation that the original oscillation angle of 7° can no longer be entirely reached by the motor as the test sequence unfolds. The shape of the torque curves and the wear grooves suggests that the torque peaks at the reversal points are not caused by an increased coefficient of friction. An elevated friction coefficient at the reversal point would result in a peak of similar magnitude with reversed sign after the direction of motion is reversed. The peaks arise from the configuration of the wear groove, which necessitates the rolling element to be pushed against the applied axial load over the edge slope of the groove. Upon reversing the direction of motion, the roller is pressed back into the groove by the applied load. The motor must exert a torque opposing the direction of motion to maintain the prescribed sinusoidal shape. Therefore a change in sign of the torque occurs only close to 1° or −1° after 160 000 cycles (dark blue solid line) in Figure 5.14, and not immediately after the reversal of motion.

Illustrated in Figure 6.15 is the progression of the energy wear coefficient α_v according to FOUVRY. This coefficient is derived by calculating the ratio of the wear volume V_n to the accumulated dissipated energy $E_{d,n}$ at a specific cycle count n.

$$\alpha_{v,n} = \frac{V_n}{\sum_{i=1}^{n} E_{d,i}} \tag{6.2}$$

In the initial 3 000 cycles, as torque remains relatively stable, it is inferred that the majority of the frictional energy is absorbed by the intact fluid and
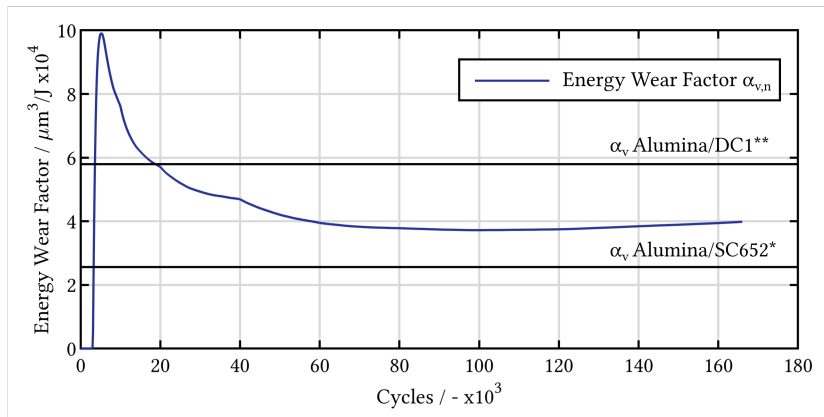
Figure 6.15.: Development of the energy wear factor α_v plotted against the number of oscillation cycles. * Energy wear factor for an Alumina/SC652 contact in the oscillating ball-on-disc test under pure sliding found in [27]. ** Energy wear factor for an Alumina/DC1 contact in the oscillating ball-on-disc test with pure sliding found in [27].

thickener film, rather than contributing significantly to wear between the metallic contact surfaces. Consequently, a threshold cycle count denoted as n_{th} is introduced, encompassing the range up to which the accumulated dissipated energy and, consequently, the energy wear coefficient α_v are assumed to be negligible (zero). Subsequent to this threshold, a rapid upsurge in the energy wear coefficient α_v ensues, culminating at a value of approximately $10\,000\,\frac{\mu m^3}{J}$. After reaching this peak, a degressive decline characterizes the curve until $\alpha_v \approx 4\,000\,\frac{\mu m^3}{J}$ at 80 000 cycles. The curve then stabilizes at a nearly constant level up to a cycle count of 160 000. In Figure 6.15, two black horizontal lines are evident, representing energy wear factors derived by Fouvry through an oscillating ball-on-disk experiment under pure sliding conditions focusing on abrasive wear and oxidative phenomena. This experimental setup featured an alumina ball as the counterbody, while the base body comprised sintered steel (DC1) and high-speed steel (HSS), among other materials. Notably, the material properties of the investigated materials by Fouvry, as well as those of 100Cr6 — employed as both the base and counterbody material in the bearing — are detailed in Table 6.2.

Table 6.2.: Characteristics of the bearing steel's material properties and the material combinations employed in [27].

	Young's modulus, E (GPa)	Poisson coefficient, v	Hardness, H (HV)
100Cr6	210	0.3	800
Alumina (counterbody)	370	0.27	2300
HSS (SC652)	230	0.28	800
DC1 (sintered steel)	200	0.3	370

SC652 and 100Cr6 exhibit comparable material properties. Alumina has a significantly higher hardness than the listed steels, while the sintered steel (DC1) demonstrates relatively lower hardness. A noteworthy observation is that the energy wear factor within the bearings during the initial phase of the test markedly surpasses the energy wear factor observed in the Alumina/DC1 combination tested by Fouvry. As the cycle count increases, the energy wear factor in the bearings aligns itself within the range of factors determined by Fouvry, trending closer to the energy wear factor observed in the Alumina/SC652 pairing.

6.1.2. Grease Parameters

Oil Separation and Base Oil Viscosity

The parameter study investigating the effects of oil separation rate and base oil viscosity was conducted using the greases from model series I (MS_I). The detailed data for these greases can be found in Table 5.4.2 in Section 5.4. Notably, grease MS_I1 possesses a low base oil viscosity of $v = 19$ cSt and an oil separation rate of $O_{sr} = 0.7\%$ (according to IP121). In contrast, grease MS_I2 differs from MS_I1 solely by the addition of an extra 20% base oil during the manufacturing process, resulting in an increased oil separation rate of 5.1%. While MS_I3 shares a similar oil separation rate with MS_I1, it possesses a significantly higher base oil viscosity of 1067 cSt. Importantly, all of these greases do not contain additives.

In Figure 6.16, the curves depicting the maximum torque per oscillation cycle are graphed for these model greases. The experimental parameters are consistent with those employed in the experiments exploring the variation of oscillation angle and frequency, as detailed in Section 6.1, utilizing grease IS_I (see Table 6.1). The left column displays the experiments conducted with

grease MS_I1, the middle column represents grease MS_I2, and the right column depicts the experiments involving grease MS_I3. Within each diagram, the tests for oscillation angles of $\theta = 2, 7, 15, 30, 45°$ are presented, with the top row showcasing experiments at an oscillation frequency of $f = 0.2\,Hz$. Subsequent rows exhibit results for other studied frequencies: $f = 1, 3, 5\,Hz$.

Notably, a key observation is the absence of torque increase at any oscillation angle for both MS_I1 and MS_I2 at $f = 0.2\,Hz$. Conversely, for MS_I3, a substantial torque increase is evident at angles $\theta = 2, 7, 15, 30°$. Notably, the experiment at 2° angle displays a peak solely during the initial phase, subsiding to a lower level after 400 cycles. At $\theta = 15°$, torque monotonically increases, exhibiting the most pronounced magnitude. At $f = 1\,Hz$, torque increase is also observed for specific parameter combinations with MS_I1. This increase is most prominent at $\theta = 15°$. In the case of MS_I2 and $f = 1\,Hz$, slight torque increases can also be discerned at $\theta = 7, 15, 30°$, though the maximum torques reached are notably lower than those for MS_I1. Grease MS_I3 at $f = 1\,Hz$, on the other hand, demonstrates significant torque increases at $\theta = 2, 7, 15, 30°$, with attained maxima surpassing those of the other model greases for the respective parameter combinations. Unlike the other greases, certain torque curves for MS_I3 reach their maximum within the first quarter of the test period, subsequently dropping to lower levels in some instances. For higher frequencies, specifically $f = 3, 5\,Hz$, it becomes evident that torque increases manifest for an expanding range of parameter combinations. For model greases MS_I1 and MS_I2, the reached torque maxima escalate with increasing frequency, while this trend is not consistently observed for grease MS_I3.

For these tests, too, the maximum coefficients of friction calculated according to Section 3.2.4 are shown in a friction color map, see Figure 6.17. When comparing the friction map of MS_I1 (top) with the map of MS_I2 (bottom left), it is immediately apparent that the damage-critical area is significantly reduced by the additional base oil. Both on the frequency and on the oscillation angle axis, the damage-critical area becomes smaller. An opposite effect is noticed when comparing the friction maps of MS_I1 (top) and MS_I3 (bottom right). The increased base oil viscosity has the effect that the damage-critical area spreads out significantly, especially towards low oscillation frequencies. Even very small oscillation angles show significantly increased coefficients of friction in contrast to the other greases. However, it is also noticeable that the operating conditions become less critical for the MS_I3 grease for an oscillation angle of $\theta = 45°$ compared to the smaller amplitude ratios investigated.
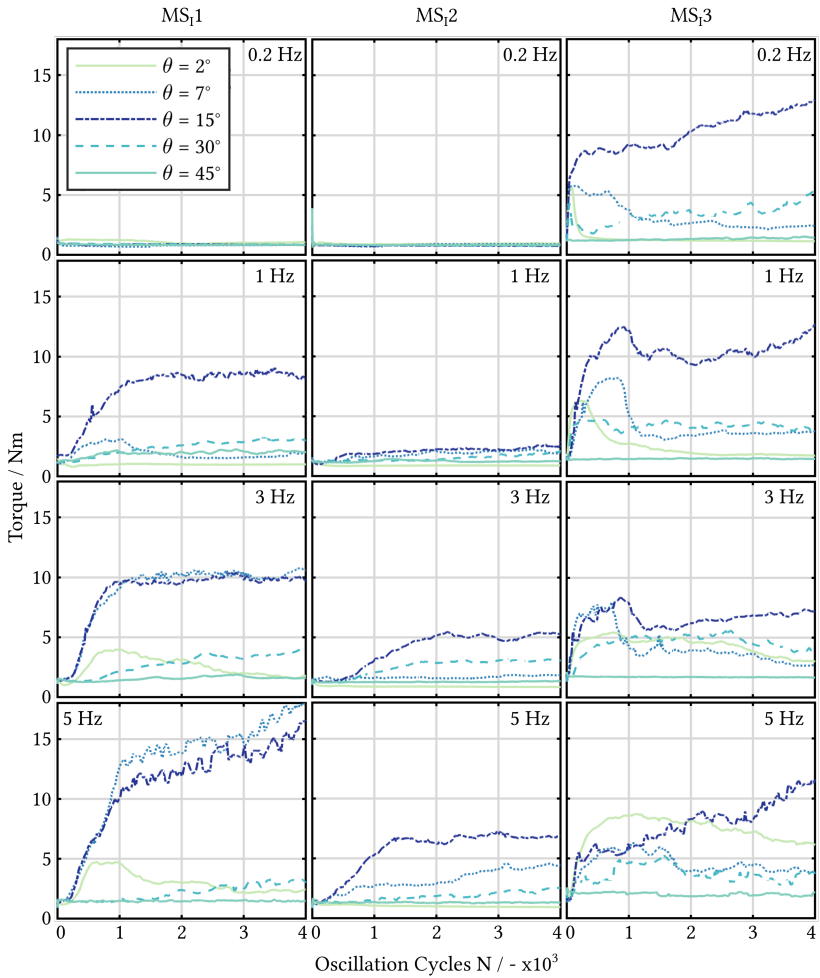
Figure 6.16.: Torque curves for the tests with model greases LiX4, LiX4+20 and LiX100 with varying oil separation rate and base oil viscosity.
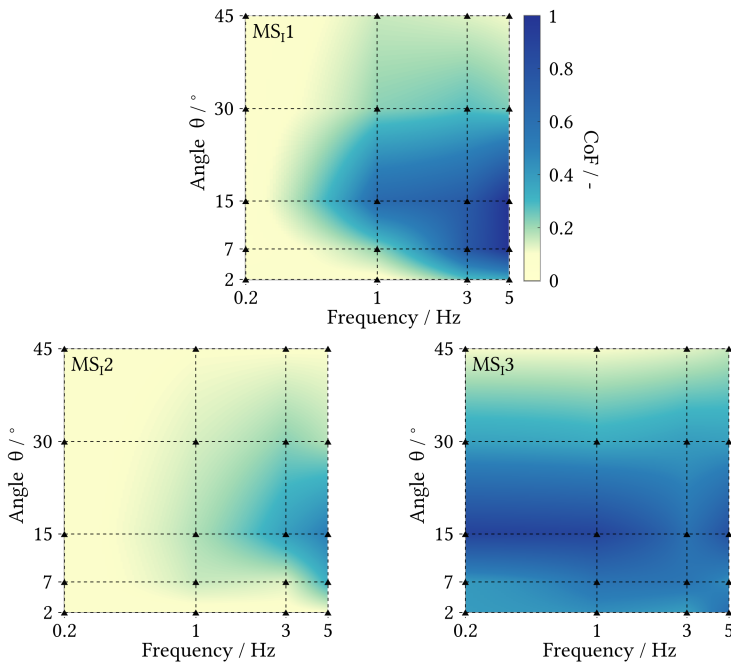
Figure 6.17.: CoF maps for the model greases LiX4, LiX4+20 and LiX100 with varying oil separation rate and base oil viscosity. Best performing: LiX4+20 with high oil separation O_{sr} and low base oil viscosity η_0.

Thickener Type, Base Oil Type and NLGI-Grade

In the second model series, a total of twelve distinct grease formulations were subjected to testing, encompassing variations in both chemical composition and physical attributes. These formulations were crafted through the combination of two distinct thickener types (lithium (Li) and calcium (Ca)), two different base oil varieties (poly-alpha-olefin (PAO) and ester (EST)), and two NLGI grades (1.5 and 2.5). The detailed compositions of these twelve greases can be found in Table 5.4 in Section 5.4.3.

From the previously illustrated friction maps, three specific parameter combinations were selected as the operational parameters for this study. These selections were made at the boundary regions of the damage-critical area.

More precisely, the chosen parameter combinations include: a small oscillation angle of $\theta = 7°$ at a frequency of $f = 3\,\text{Hz}$, an oscillation angle of $\theta = 15°$ which was earlier identified as the most critical angle, paired with a frequency of $f = 1\,\text{Hz}$, and finally, a larger oscillation angle of $\theta = 30°$ in conjunction with a frequency of $f = 3\,\text{Hz}$. These specified parameter combinations have been marked with distinctive red triangles on the friction map for grease IS1, as exemplified in Figure 6.18. Additionally, offset color squares corresponding to the selected parameter combinations are also displayed. These color squares are further organized into color triplets, as indicated by the accompanying arrows in Figure 6.18. Within each triplet, the name of the respective grease (in this case, IS1) and the associated coefficient of friction for the given color square are presented.

The lower section of Figure 6.18 presents the outcomes of the twelve analyzed greases under the three aforementioned operational parameter combinations. The arrangement is structured with columns denoting the various combinations of thickener and base oil types, while the rows correspond to the NLGI grades. Specifically, the third row includes greases to which the low viscosity base oil was subsequently added, therefore denoted as 'Low Visc.'. Further information regarding these greases can be found in Section 5.4.3.
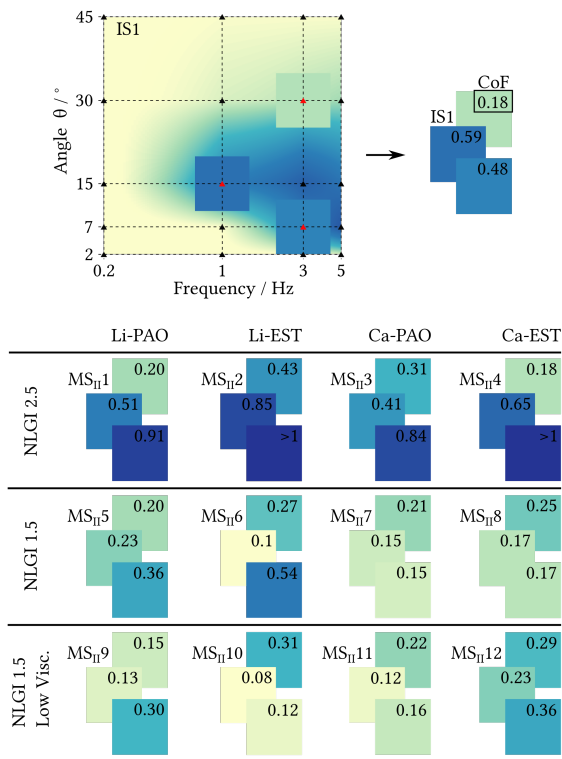
Figure 6.18.: An overview of the maximum torque values reached for the greases in MS_{II} during tests at $e = 4$ and $f = 3$ Hz, $e = 8$ and $f = 1$ Hz, and $e = 16$ and $f = 3$ Hz.

Initial observation reveals a pattern where greases with NLGI-grade 2.5 exhibit notably inferior performance when compared with greases possessing a lower NLGI-grade of 1.5, particularly at oscillation angles of $\theta = 7°$ and $\theta = 15°$. This trend is consistently apparent irrespective of the thickener and base oil type. The influence of the thickener and base oil type is less conspicuous. To analyse this impact, Figure 6.19 illustrates the averaged maximum coefficients of friction reached, as they relate to the operating parameters and the type of thickener used.

In this context, the x-axis lists the respective parameter combinations. The blue bars correspond to the mean coefficient of friction among all greases

featuring a lithium-based thickener, while the green bars represent the mean coefficient of friction for greases with a calcium-based thickener, aligned with the corresponding parameter combination.

Upon analyzing the chart, a notable observation is that the mean coefficient of friction for calcium-based greases is consistently lower than that observed for lithium-based greases across all tested parameter combinations. The most significant discrepancy, amounting to $\Delta\mu = 0.09$, is attained at 3 Hz and 7°, while differences for other parameter combinations are relatively minor ($\Delta\mu < 0.03$). However, it is essential to note that, while the overall trend favors calcium thickeners, individual results do not uniformly support this pattern. For instance, upon comparing $MS_{II}6$ and $MS_{II}10$ with $MS_{II}8$ and $MS_{II}12$ at 1 Hz and 15°, the friction values obtained are lower for lithium-based greases. Due to the presence of considerable standard deviation, a definitive performance advantage of a particular thickener cannot be determined from these findings.

Similarly, the right diagram in Figure 6.20 presents the evaluation concerning the distinct base oil types PAO and EST. Here, a discernible pattern is evident in the mean values, indicating a lower friction value for PAO in comparison to EST. However, akin to the thickener analysis, isolated results exhibit contradictory behavior. For example, $MS_{II}6$ and $MS_{II}10$ at 1 Hz and 15° performed better than their counterparts employing PAO base oil.

The conspicuous variance in performance between low and high NLGI-grades appears to be unrelated to the chemical composition of the greases. An insightful observation emerges upon considering the oil separation rate of the greases, where it becomes evident that greases with higher NLGI-grades tend to exhibit lower oil separation. Specifically, all greases with an NLGI-grade of 2.5 display oil separation rates of $O_{sr} \leq 2\%$, while greases with an NLGI-grade of 1.5 exhibit oil separation rates of $O_{sr} > 2.8\%$. In order to graphically depict the relationship between oil separation rate, base oil viscosity, and the maximum coefficient of friction, Figure 6.21 showcases the reached maximum coefficients of friction μ_{max} plotted against the coefficients of oil separation rate O_{sr} and base oil viscosity η_0. The presentation employs dark blue dots to denote test outcomes for the parameter combination of 3 Hz and 7°, dark green dots for tests at 1 Hz and 15°, and light green dots for tests at 3 Hz and 30°. Additionally, corresponding linear trend lines are depicted for each parameter combination. Across all parameter combinations, a consistent trend emerges, indicating a positive correlation between the
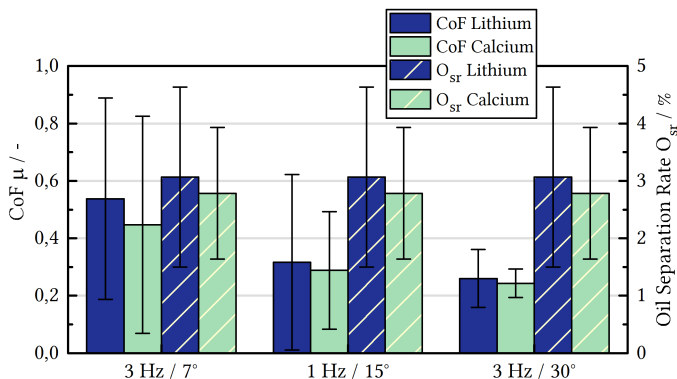
Figure 6.19.: Bar chart illustrating the mean values of the maximum coefficient of friction μ across the examined operating parameter combinations. The blue bars depict the mean values of the tested greases with Li thickener, while the green bars represent those with Ca thickener. The striped bars indicate the mean oil separation rate O_{sr} of the greases. Standard deviations are denoted by black error bars.
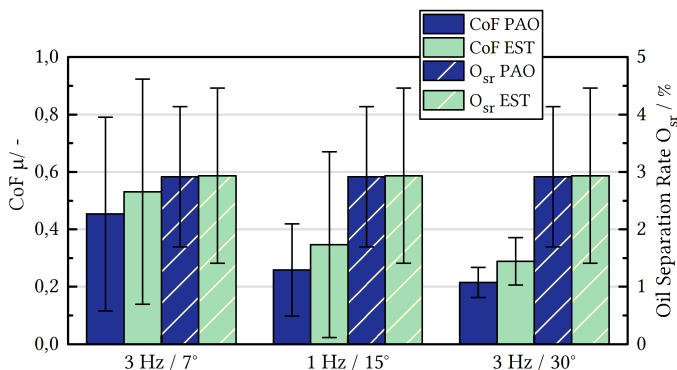
Figure 6.20.: Bar chart depicting the mean values of the maximum coefficient of friction μ across the tested operating parameter combinations. The blue bars denote the mean values of the tested greases with PAO base oil, while the green bars represent those with EST base oil. The striped bars display the mean oil separation rate O_{sr} of the greases. Standard deviations are indicated using black error bars.

maximum coefficient of friction μ_{max} and the coefficient of base oil viscosity η_0 and oil separation rate O_{sr}. Notably, the slope of the trend line appears remarkably similar for the parameter combinations of 3 Hz and 7°, as well as 1 Hz and 15°. In contrast, the slope is notably lower for the 3 Hz and 30° combination.
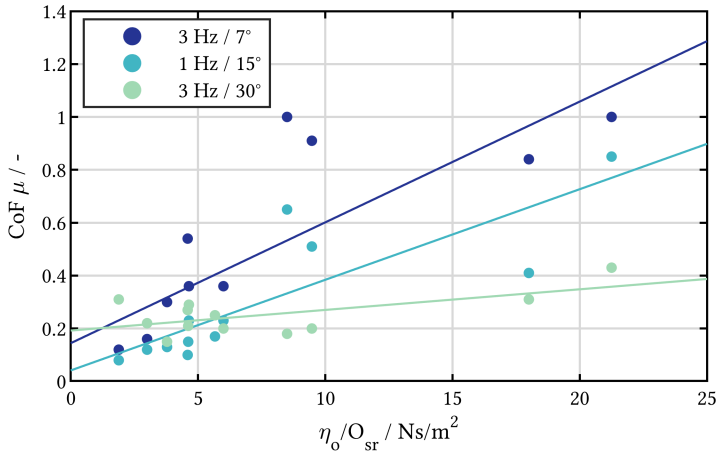
Figure 6.21.: Chart illustrating the maximum Coefficient of Friction (CoF) values μ as colored circles plotted against the ratio of base oil viscosity η_0 to oil separation rate O_{sr}. The values are color-coded according to the tested parameter combinations of 3 Hz and 7° (dark blue), 1 Hz and 15° (turquoise), and 3 Hz and 30° (green). Additionally, trend lines for the respective operating parameter combinations are drawn in their corresponding colors.

Fully formulated industrial greases

This section presents the findings from tests involving fully additivated greases commonly employed in industrial applications. A comparison of friction maps for greases IS1 and IS2 is illustrated in Figure 6.22. Notably, IS2 is a calcium-based grease characterized by a relatively high oil separation rate of $O_{sr} = 6.1\%$ and a low base oil viscosity of $\nu = 13$ cSt at 40° C. A key observation is that the most critical oscillation angle, which denotes the angle at which the damage-critical range extends the farthest into the realm of low

frequencies, deviates from the $\theta = 15°$ observed in experiments within the MS_I model series (Section 5.4.2) and the IS grease series.
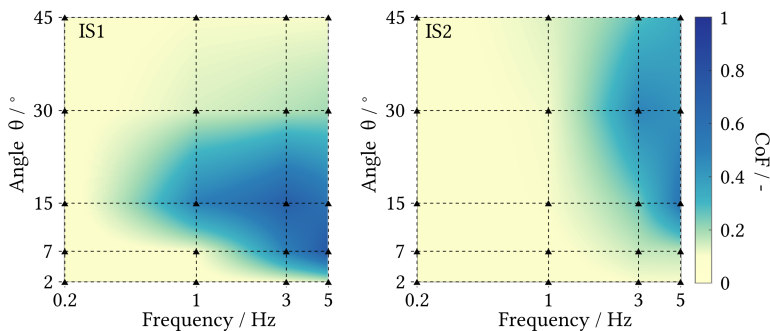
Figure 6.22.: Comparison of CoF color maps for grease IS1 (left) and grease IS2 (right).

The industrial greases, specifically IS3 through IS5, were subjected to tests mirroring those conducted on the greases from the model series MS_{II} at three parameter combinations situated within the boundary region of the damage-critical area: $f = 3\,\text{Hz}\ \theta = 7°$, $f = 1\,\text{Hz}\ \theta = 15°$, and $f = 3\,\text{Hz}\ \theta = 30°$. The outcomes of these tests are presented in Figure 6.23, using the methodology outlined in Section 5.4.3, which employs color triplets to convey the associated friction values. Further details regarding the grease properties can be found in Section 5.4.1. Broadly speaking, the tested greases can be divided into two categories. On one hand, greases IS1 to IS3 possess a comparatively low base oil viscosity ($v = 13 - 130\,\text{cSt}$ at 40° C) coupled with a high oil separation rate ($O_{sr} = 4 - 6.1\%$). On the other hand, IS4 and IS5 greases exhibit a high base oil viscosity of $v = 460\,\text{cSt}$ at 40° C, along with a lower oil separation rate ranging between $O_{sr} = 1.7 - 2.2\%$. Upon comparing the color triplets of these greases, it becomes evident that greases IS4 and IS5 exhibit substantially higher coefficients of friction (CoF) than greases IS1 to IS3 within the context of smaller oscillation angles (7°, 15°). However, this distinction diminishes when considering an angle of (30°), as the achieved CoFs are generally low for all greases except for grease IS2.

Figure 6.23.: Color triplets and associated coefficients of friction for industrial greases IS1-IS5.

6.2. Investigations on Base Oil Reflow

The preceding bearing tests have revealed that both the oil separation rate (O_{sr}) and the base oil viscosity (η_0) have an influence on damage initiation in oscillating rolling bearings. To gain a deeper insight into the impact of base oil reflow and the associated lubrication mechanisms, this section presents the outcomes of targeted rolling bearing tests conducted on the oscillating bearing test rig. Additionally, model tests performed on the EHL-tribometer are also included to further elucidate these effects.

6.2.1. Bearing Experiments - Base Oil Reflow

To underscore the significance of base oil reflow for contact lubrication, a series of bearing tests were conducted. For this purpose, a parameter combination of an oscillation frequency $f = 3\,\text{Hz}$ and an oscillation angle $\theta = 15°$ was chosen. This parameter set was previously identified as critical for damage initiation during continuous oscillation. However, in these experiments, a unique approach was employed. Interruptions in the form of pauses with a duration of t_p were introduced to facilitate base oil reflow. The pause duration (t_p) was varied between 5 and 60 seconds, while the number of uninterrupted base cycles (N_u) between the pauses ranged from a maximum of 100 cycles to a minimum of 1 cycle. The specific combinations of parameters investigated are detailed in Table 6.3. It is important to note that the pauses were consistently timed to coincide with the zero crossing of the oscillation. Following each pause, the oscillation was resumed from the corresponding position. The motion profile during these tests is visually represented in Figure 6.24.
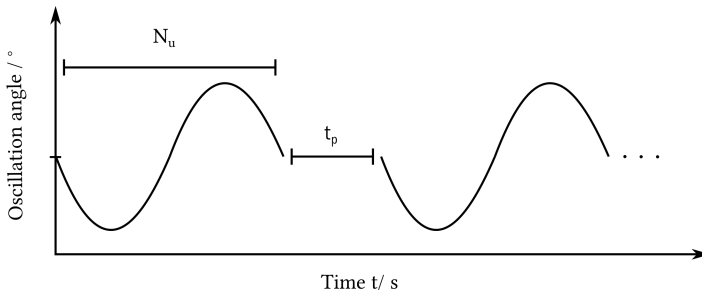
Figure 6.24.: Schematic of the movement pattern during the bearing tests with pauses for base oil reflow.

No.	N_u/-	t_p/s	$\frac{N_u}{t_p}/\frac{1}{s}$	T_{max}/Nm
0	4 000	0	∞	10
1	1	5	0.2	2.23
1.1	1	5	0.2	1.58
2	10	5	2	3.51
2.1	10	5	2	4.11
3	50	5	10	4.22
4	100	5	20	6.63
4.1	100	5	20	5.28
5	10	60	$0.1\overline{66}$	2.49
5.1	10	60	$0.1\overline{66}$	1.64
6	100	60	$1.\overline{66}$	3.77
6.1	100	60	$1.\overline{66}$	3.59
7	600	60	10	4.6

Table 6.3.: Number of uninterrupted base cycles N_u and pause duration t_p with the corresponding quotient $\frac{N_u}{t_p}$ and the maximum torque T_{max} reached during the experiment. The total number of cycles for all tests is $N = 4\,000$.

Figure 6.25 illustrates the torque curves of selected tests with a consistent pause duration of $t_p = 5\,\mathrm{s}$, while the number of uninterrupted base cycles is varied as $N_p = 100, 50, 10, 1$. The dark blue curve represents the torque progression of the reference test conducted at $f = 3\,\mathrm{Hz}$ and $\Theta = 15°$ without any interruptions. This torque curve exhibits an initial rise around the 700th cycle and subsequently follows a continuous monotonic increase, reaching an approximate value of 10 Nm. Upon introducing pause periods, a discernible reduction in the maximum torque after $N = 4\,000$ cycles is observed. Specifically, for the test employing a five-second pause following every 100 base cycles, there is a noticeable drop in the maximum torque from 10 Nm to 6.5 Nm. Further reduction in the number of uninterrupted base cycles, N_u, continues to diminish the maximum torque. In the scenario where only 1 base cycle occurs between successive pauses, the torque remains consistently low, as indicated by the light green curve in Figure 6.25.
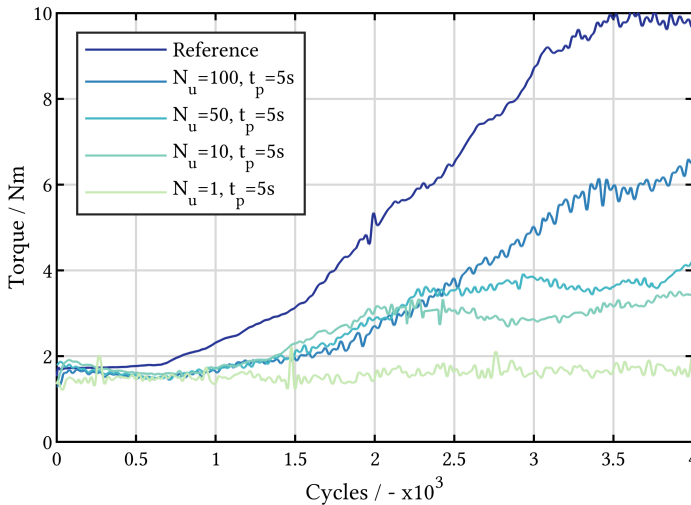
Figure 6.25.: Resultant torque curves from oscillating bearing tests with varying numbers of uninterrupted base cycles N_u, a constant pause duration t_p, and grease IS1.

Figure 6.26 depicts the outcomes of selected test runs in which a consistent number of uninterrupted base cycles $N_u = 10$ and $N_u = 100$ were maintained,

while the pause duration t_p was varied at values of t_p = 5 and 60 s. The dark blue curve corresponds to the reference experiment. For the setting of N_u = 10 and t_p = 5 s, the maximum torque reached amounts to T_{max} = 3.5 Nm, signifying a reduction of 6.5 Nm compared to the reference test. When the pause duration t_p is increased from 5 s to 60 s, the torque curve remains consistently at a lower level, as indicated by the light green curve. In essence, the experiments with incorporated pauses highlight that both reducing the number of base cycles and extending the pause duration yield wear-reducing effects in oscillating rolling element bearings.
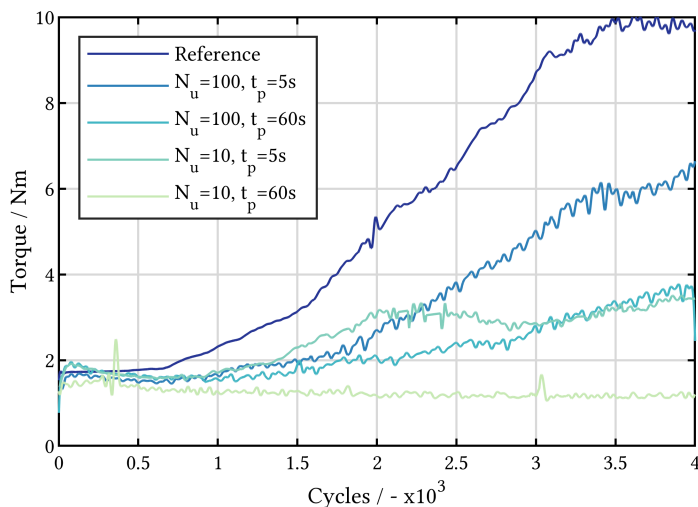
Figure 6.26.: Resultant torque curves from oscillating bearing tests with constant number of uninterrupted base cycles N_u and varying pause duration t_p.

To elucidate this relationship further, the correlation between the maximum torque T_{max} reached in tests No. 1-7 and the ratio of the number of cycles N_u to the pause duration t_p is depicted in Figure 6.27, along with corresponding details provided in Table 6.3. The blue circles represent the measured maximum torque values from the experiments, which are approximated by a logarithmic trend curve. Notably, tests No.1, No.1.1, No.5, and No.5.1, each exhibiting a quotient $\frac{N_u}{t_p} \leq 0.2$, demonstrate nearly undamaged conditions

concerning torque and raceway damage. As the quotient increases, both the maximum torque and the extent of raceway surface damage escalate. It is important to mention that the reference test is not encompassed in this representation.
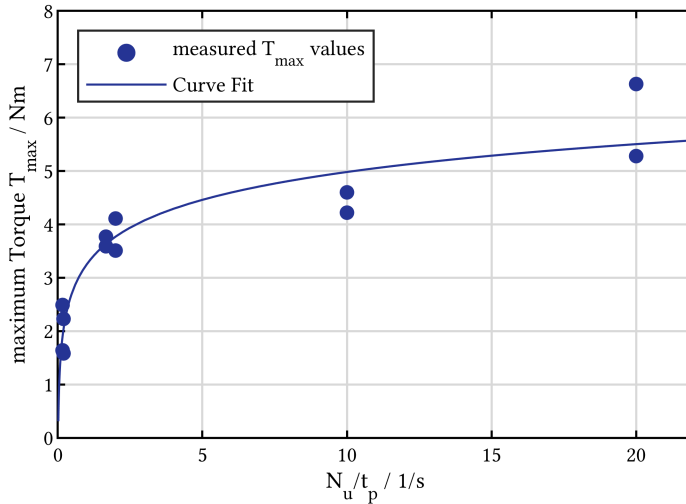
Figure 6.27.: Maximum torque values plotted against the quotient of the number of uninterrupted base cycles N_u and the pause duration t_p.

6.2.2. Model Experiments - Base Oil Reflow

To gain deeper insights into the lubricant behavior surrounding the rolling contact, a series of experiments is conducted using the optical EHL-tribometer, as introduced in Section 5.3. The experimental setup replicates the approach utilized in the rolling bearing tests, involving an oscillating motion pattern interrupted by pause intervals. The primary objective of these experiments is to quantitatively assess the phenomenon of base oil reflow during the pause intervals and its effects on the subsequent oscillation cycle. For this purpose, a pause is introduced after a specified number of oscillation cycles N_p. During the final cycle prior to the pause ($N_p - 1$), as illustrated at the top of Figure 6.28,

the region within the inlet of the rolling element that is filled with lubricant is measured. The measured wetted area is depicted using a transparent blue overlay in the figure. Subsequently, a 50-second pause is initiated. During this pause, changes in both the lubricant wetted area at the inlet and outlet are carefully monitored. The images in the middle section of Figure 6.28 illustrate the measured area wetted with lubricant at the onset of the pause (upper image) and after the pause (lower image). Following the pause, the oscillation motion resumes. In the cycle immediately subsequent to the pause ($N_p + 1$), depicted at the bottom of Figure 6.28, the area within the inlet that remains wetted with lubricant is measured once again.
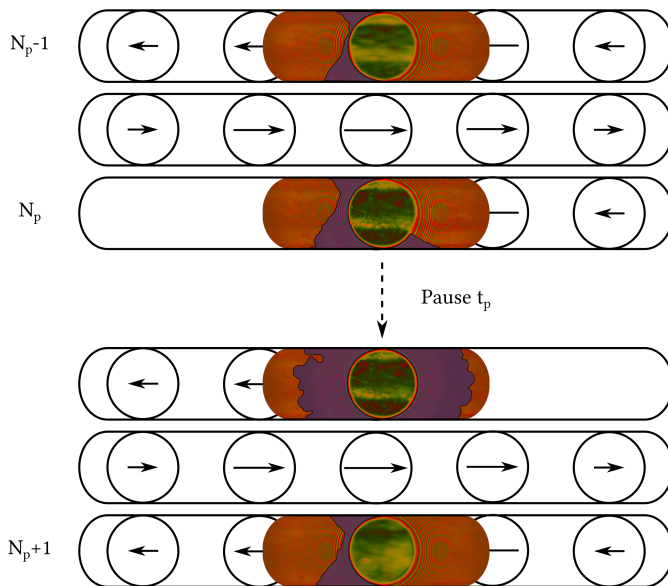
Figure 6.28.: Schematic representation of the measurement of lubricant reflow into the near field of the rolling contact on the EHL-tribometer. The measurements are conducted after $N_p = 100$, 500, 1 000, 1 500, and 2 000 cycles.

In both the cycle preceding and following the pause, the central, minimum, and maximum lubricant film heights (h_c, h_{min}, and h_{max}) within the contact

region are determined. This comprehensive evaluation allows us to assess the influence of changes in lubricant volume within the inlet on the film height within the contact.

Figure 6.29.: Development of the lubricant wetted area in the outlet region of the rolling element contact throughout the duration of the pause for grease $MS_{II}1$. The measurements are taken during the pauses after N_p = 100, 500, 1 000, 1 500, and 2 000 cycles.

The experimental tests are conducted using eight model greases from the MS_{II} series, which is detailed in Section 5.4.3. These greases are also employed in the bearing tests discussed in Section 6.1.2. The specific greases, labeled $MS_{II}1$ through $MS_{II}9$, are categorized as follows:

- Greases $MS_{II}1$ to $MS_{II}4$ have an NLGI grade of 2.5 and exhibit low oil separation O_{sr}.

- Greases $MS_{II}5$ to $MS_{II}13$ have an NLGI grade of 1.5 and demonstrate higher oil separation.

- The thickener composition varies between lithium and calcium.

- The base oil type varies between poly-alpha-olefin and ester.

- Greases $MS_{II}1$ to $MS_{II}9$ possess a low base oil viscosity ranging from v = 14 to 18 cSt at 40° C.

- Grease $MS_{II}13$ has an increased base oil viscosity of $v = 160$ cSt at $40°$ C.

As shown in Figure 6.28, during the pause interval, both the wetted area in the inlet and outlet of the rolling element contact increases. For instance, Figure 6.29 provides an illustrative example depicting the evolution of the lubricant-wetted area in the outlet for grease $MS_{II}1$. In this graph, the x-axis represents the pause duration, while the y-axis represents the measured wetted area relative to the Hertzian contact area. The plot includes five curves, each corresponding to a pause implemented after $N_p = 100, 500, 1\,000, 1\,500$, and $2\,000$ cycles. The curves reveal that the area wetted with lubricant is minimal at the beginning of the pause and subsequently increases with an extended pause duration. Observing the curves for the outlet in Figure 6.29, it is evident that the curve representing the wetted area during the pause after $N_u = 100$ cycles lies below the curves corresponding to the pauses after higher cycle numbers. However, it is important to note that this behavior is not universally representative across all grease samples. Depending on the specific grease, wetting may exhibit different patterns, with some greases demonstrating more effective wetting after a higher number of cycles, and others showing enhanced wetting after a lower cycle count.

To facilitate comparison of the reflow behavior during the pause intervals across different greases, an average value of the wetted area over all pause intervals is employed. Figure 6.30 depicts the development of the mean relubricated area within the outlet of the rolling element contact. This representation highlights the relationship between the pause duration (x-axis), the quotient $S_{N,red}$ (y-axis), and the mean lubricant-wetted area (z-axis). This quotient $S_{N,red}$ is defined by Equation 6.3 and contains base oil viscosity η_0, oil separation rate O_{sr}, and surface tension σ_s of the base oil.

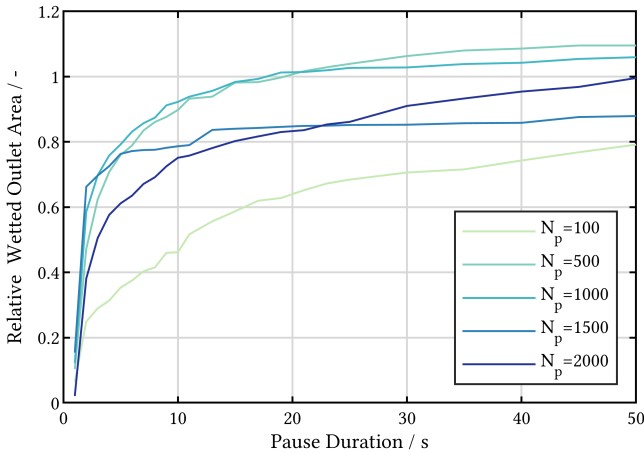$$S_{N,red} = \frac{\eta_0}{\sigma_s \cdot O_{sr}} \tag{6.3}$$
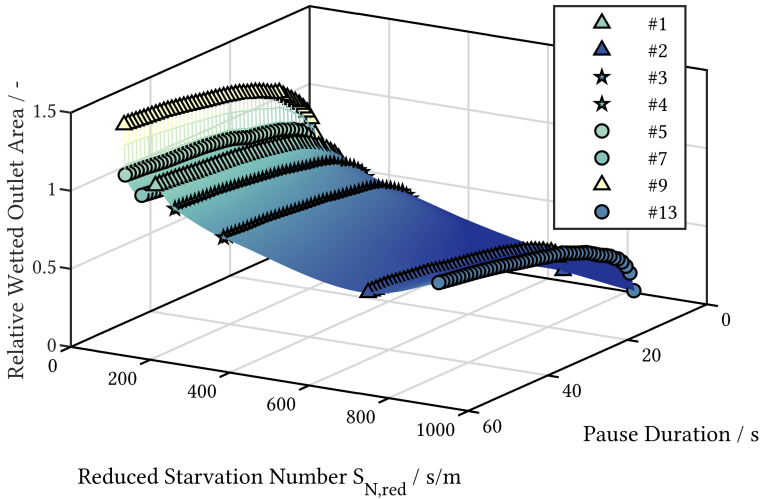
Figure 6.30.: Development of the average lubricant wetted area in the outlet of the rolling element contact throughout the duration of the pause, in relation to the quotient of base oil viscosity η_0 and the product of oil separation rate O_{sr} and surface tension σ_s of the base oil.

The individual grease samples are represented by their respective quotient $S_{N,red}$. Linear interpolation was employed to increase the visual relationship between these factors. As observed in Figure 6.29 (using grease $MS_{II}1$ as an example), a progressively increasing wetted area with longer pause times can be observed for all the other grease samples as well. Figure 6.31 further demonstrates that the wetted area also experiences a degressive increase over time for the contact inlet. Both for the inlet and the outlet, there is a tendency for the relubricated area to decrease as the quotient $S_{N,red}$ increases. This suggests that a combination of low base oil viscosity and high oil separation rate promotes effective lubricant reflow within the near field of the contact.

Figure 6.32 displays the outcomes of the assessment regarding the lubricant reflow in the inlet of the rolling contact during the cycle preceding the pause (N_p-1) and the cycle succeeding the pause (N_p+1) for all the different lubricants. On the y-axis, the surface area wetted with lubricant is presented in relation to the HERTZian contact area, while the x-axis represents the various grease samples. The dark blue bars correspond to the mean wetted inlet area before
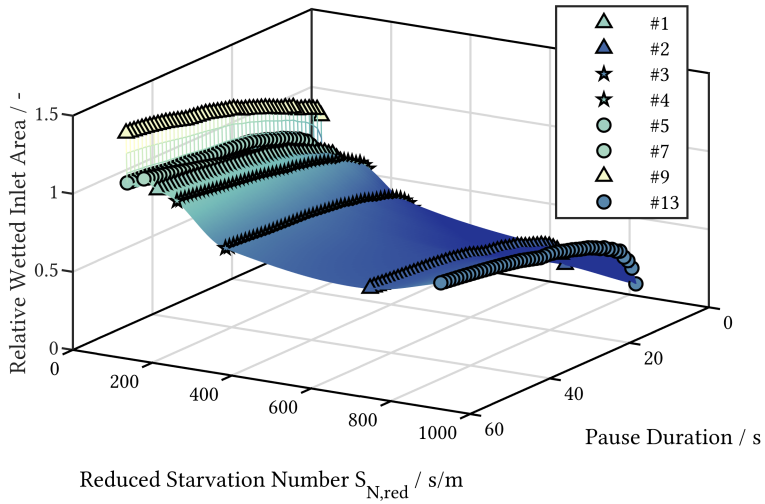
Figure 6.31.: Development of the average lubricant wetted area in the inlet of the rolling element contact throughout the duration of the pause, in relation to the quotient of base oil viscosity η_0 and the product of oil separation rate O_{sr} and surface tension σ_s of the base oil.

Grease	Thickener	Base Oil	η_0/Pas at RT	NLGI	$O_{sr}/-$	$\sigma_s/\frac{mN}{m}$
MS$_{II}$1	Li	PAO	0.0328	2.5	0.01	28.85
MS$_{II}$2	Li	EST	0.033	2.5	0.002	25.52
MS$_{II}$3	Ca	PAO	0.0328	2.5	0.004	28.85
MS$_{II}$4	Ca	EST	0.033	2.5	0.008	25.52
MS$_{II}$5	Li	PAO	0.0328	1.5	0.03	28.85
MS$_{II}$6	Li	EST	0.033	1.5	0.018	25.52
MS$_{II}$7	Ca	PAO	0.0328	1.5	0.033	28.85
MS$_{II}$13	Li	PAO	0.333	1.5	0.014	28.79

Table 6.4.: Parameters of the model greases utilized for the study on base oil reflow on the EHL-tribometer.

the pause at N_p = 100, 500, 1 000, 1 500, and 2 000 cycles. In contrast, the green bars represent the mean wetted inlet area after the pause. Additionally, the light yellow bars portray the quotient $\frac{1}{S_{N,red}}$ of the greases, which is indicated on the right secondary y-axis. This analysis aims to explore how the lubricant reflow during the pause influences the lubricant supply to the contact inlet in the subsequent oscillation after the pause.
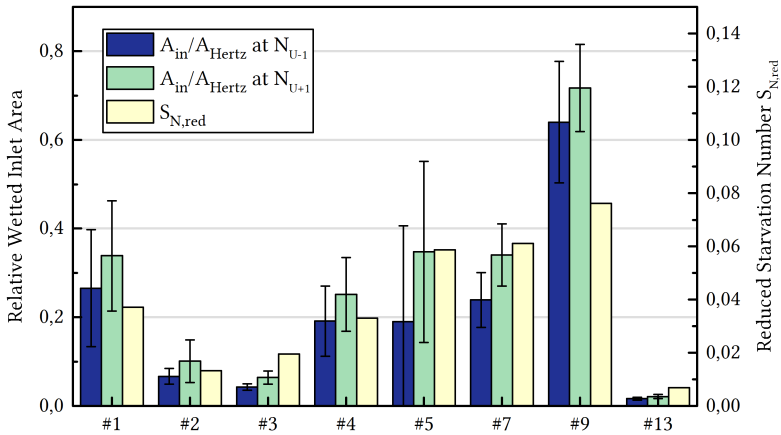
Figure 6.32.: Mean values of the wetted inlet area before (dark blue) and after (green) the pauses after N_p = 100, 500, 1 000, 1 500, and 2 000 cycles. The light yellow bars display the reciprocal of the reduced starvation number $S_{N,red}$.

Upon initial examination, it is evident that the wetted inlet area is larger in the half cycle after the pause (green) compared to the half cycle before the pause (dark blue), irrespective of the tested grease sample. A clear correlation can also be observed between the quotient $\frac{1}{S_{N,red}}$ of the greases and the wetted inlet area. For instance, grease $MS_{II}9$ exhibits the largest wetted area both before and after the pause, and it also possesses the highest oil separation rate O_{sr}, resulting in the highest quotient $\frac{1}{S_{N,red}}$. Conversely, greases $MS_{II}2$, $MS_{II}3$, and $MS_{II}13$ display notably lower wetted inlet areas. In the case of $MS_{II}2$ and $MS_{II}3$, these observations align with low oil separation rates (O_{sr} = 0.8%

and $O_{sr} = 1\%$, respectively) and consequently low quotients $\frac{1}{S_{N,red}}$. Grease $MS_{II}13$ exhibits the lowest wetted areas despite a high oil separation rate of $O_{sr} = 3.2\%$. However, this grease has a significantly higher base oil viscosity compared to the other samples, leading to a high quotient $\frac{1}{S_{N,red}}$.

The previous findings have demonstrated that lubricant supply to the contact can be enhanced by introducing pauses, and that greases with a low quotient $S_{N,red}$ offer improved lubricant supply in oscillating operation. Moving forward, the impact of the additional lubricant introduced to the contact inlet due to the pauses on lubricant film formation in the ball-on-disc contact will be explored. To achieve this, lubricant film height measurements were taken in the cycle preceding each pause (N_p-1) and the cycle following each pause (N_p+1), and the difference was computed for each instance.

Figure 6.33 presents the outcomes of the calculated changes in minimum h_{min} (dark blue bar), maximum h_{max} (light green bar), and central h_c (green bar) lubricant film height (primary y-axis), as well as the wetted inlet area for each condition for grease sample $MS_{II}5$. The ensuing diagrams consistently portray relative lubricant film heights. This denotes that the measured lubricant film height is standardized relative to the central lubricant film height $h_{c,oil}$ of the base oil, as determined in according to HAMROCK AND DOWSON. Likewise, the alteration in the wetted inlet area is normalized in relation to the HERTzian contact area.

In Figure 6.34, the results are shown for grease sample $MS_{II}3$. The light yellow bars in Figure 6.33 demonstrate an increase in wetted inlet area after the pause for all experimental time points, except after $N_p = 2\,000$ for sample $MS_{II}3$. However, the alteration in wetted inlet area does not always exhibit a straightforward correlation with the change in lubricant film height. In the case of central film height h_c (green bars) in Figure 6.34 for grease sample $MS_{II}5$, changes appear to correlate, implying that an augmented presence of lubricant in the inlet leads to a higher central lubricant film height. Correspondingly, a decrease in lubricant supply, as seen with $N_p = 2\,000$, results in a lower central film height h_c. However, the minimum and maximum film heights h_{min} and h_{max} sometimes show contrasting behavior. For instance, the change in h_{min} after $N_p = 100$ cycles exhibits a significant decrease, despite the increase in lubricant supply to the inlet. Similarly, no discernible correlation between measured lubricant film heights and lubricant presence in the inlet can be identified for grease sample $MS_{II}3$.
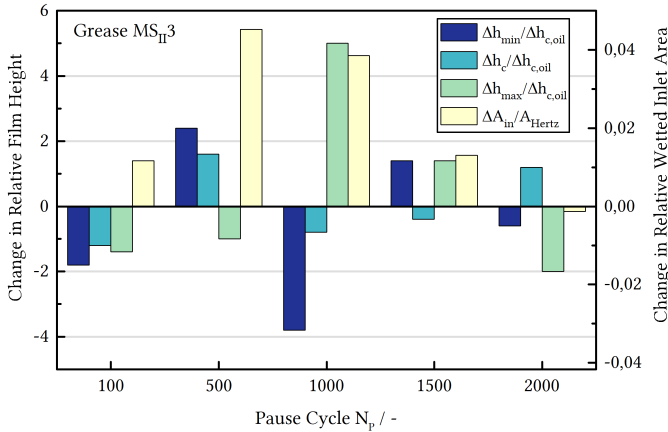
Figure 6.33.: Variation of the minimum (dark blue bar), maximum (light green bar), and central (green bar) lubricant film height beneath the wetted inlet surfaces (yellow bars) during the inserted breaks at cycle number N_p. The diagram presents findings for grease sample $MS_{II}3$.

Figure 6.35 depicts the mean value of the change in central film heights h_c (dark blue bars) and the mean value of the change in wetted inlet area (green bars) across all pauses for each respective grease sample. At first glance, an apparent correlation between the mean changes in wetted inlet area and central lubricant film height is evident. However, upon closer examination, when considering the standard deviation of the measured mean lubricant film heights and analyzing individual measurements (examples of which are illustrated in Figure 6.33 and Figure 6.34), it is not possible to conclusively infer a correlation between inlet lubricant supply and lubricant film height using the employed testing and analysis methods.

In summary, the investigations on base oil reflow have demonstrated that wear in oscillating rolling bearings can be mitigated by introducing pauses. The experiments conducted on the optical EHL-tribometer have revealed the occurrence of lubricant reflow, likely involving base oil, during pauses within the oscillation. This base oil reflow is facilitated by higher oil separation rates and lower base oil viscosity. Despite these findings, it has not been definitively established that a direct correlation exists between the lubricant supply to the inlet and changes in lubricant film height.
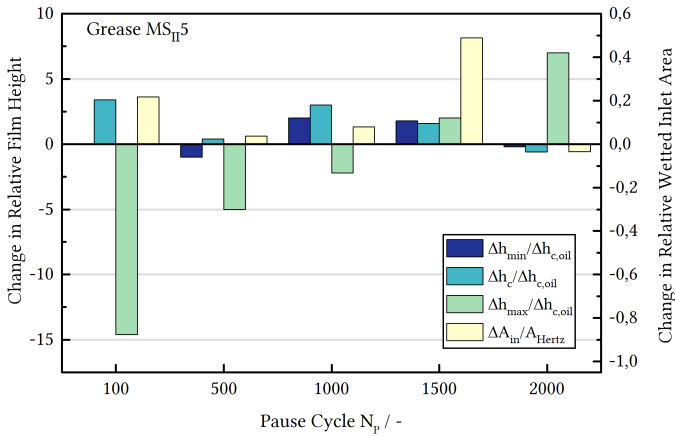
Figure 6.34.: Variation of the minimum (dark blue bar), maximum (light green bar), and central (green bar) lubricant film height beneath the wetted inlet surfaces (yellow bars) during the inserted breaks at cycle number N_p. The diagram presents findings for grease sample $MS_{II}5$.
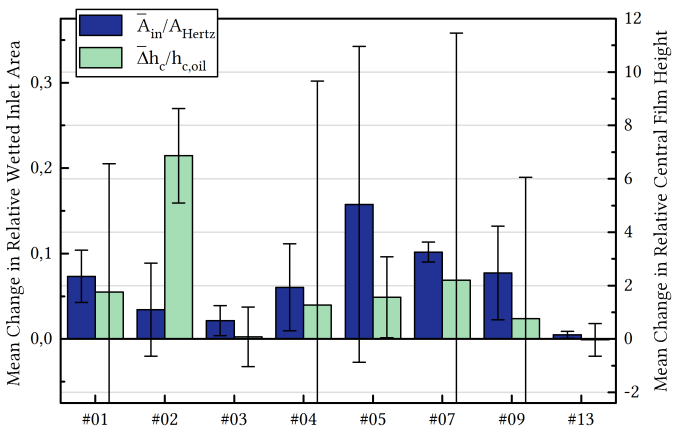
Figure 6.35.: Change in the average central film height within the rolling contact due to the introduction of pauses (green), compared to the alteration of the wetted inlet area (blue).

6.3. Role of the Cage

The bearing experiments discussed in Section 6.1 reveal that the test conditions involving larger oscillation angles ($\theta > 30°$) are less critical with respect to early wear initiation. One conjecture is that, apart from the conventional base oil bleeding, an additional relubrication mechanism may arise due to the interaction between the rolling element and the bearing cage. This hypothesis will be examined in the subsequent sections. To achieve this, similar to the approach delineated in Section 6.2.1, a combination of component tests conducted on the oscillating bearing test rig and model tests conducted on the optical EHL-tribometer are carried out.

6.3.1. Bearing Tests - Lubrication Cycles

To elucidate the impact of larger oscillation angles on wear initiation, a comparable approach, as detailed in Section 6.2.1, was adopted for the component tests. The wear-critical parameter combination comprises an oscillation angle of $\theta_b = 15°$ and a frequency of $f = 3\,\mathrm{Hz}$, and is used as the base oscillation cycle. In contrast to the methodology outlined in Section 6.2.1, the base cycles in this scenario are not interrupted by pauses. Instead, they are interspersed with lubrication cycles featuring a larger oscillation amplitude θ_l. A graphical depiction of this motion profile is provided in Figure 6.36. For subsequent reference, the uninterrupted base cycles are denoted by N_u, while the total count of base cycles is represented by N_a. Detailed experimental conditions are tabulated in Table 6.5. In this specific series of tests, bearings equipped with the original plastic cage of an FAG type 7208-B-XL-TVP bearing, along with the complete set of rolling elements, were employed.

No.	N_a	N_u	$\theta_l/°$	N_{4Nm}
0	4 118	4 118	-	1 747
1	3 099	100	30	2 969
1.1	2 782	100	30	2 427
2	4 967	100	33.75	4 888
2.1	8 188	100	33.75	7 257
3	9 081	100	37.5	7 482
3.1	9 339	100	37.5	8 562
4	14 088	100	45	12 764
4.1	20 977	100	45	14 920
5	21 309	100	50	-
5.1	21 742	100	50	-
6	21 890	100	60	-
6.1	36 359	100	60	-
6.2	186 678	100	60	-

Table 6.5.: Test results of the bearing tests with lubrication cycles: N_a - total number of oscillation cycles; N_u - number of uninterrupted base cycles; θ_l - angle of the lubrication cycle; N_{4Nm} - number of cycles until a torque limit of 4,Nm is exceeded.
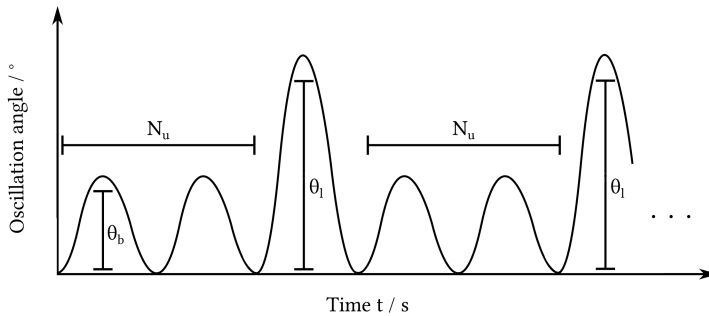
Figure 6.36.: Diagram illustrating the movement pattern during the bearing tests with lubrication cycles.

As in previous evaluations, the examination of the tests is conducted based on the evolution of the maximum torque per base oscillation cycle.

Figure 6.37 portrays the torque profiles of tests employing lubrication cycles (No. 1-No. 6) with varying oscillation angles θ_l, alongside the torque curve of the reference test conducted without lubrication cycles (No. 0). The smallest investigated lubrication cycle features an angle of $\theta_l = 30°$, implemented in experiments No. 1 and No. 1.1, illustrated by the dark blue curves in Figure 6.37. Notably, these curves exhibit the most pronounced torque surge, apart from the reference test (black curve). It's worth mentioning that, in this instance, the lubrication cycle does not exert a decisive influence on the bearing's wear behavior. Subsequently, experiments No. 2 to No. 4 employ larger angles for the lubrication cycle (θ_l of 33.75°, 37.5°, and 45°).
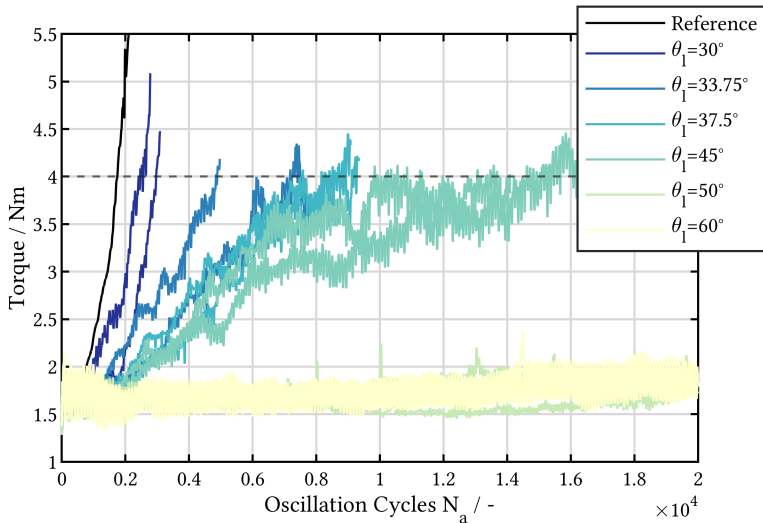
Figure 6.37.: Trend of the maximum torque in the base cycles for integrated lubrication cycles with varying oscillation amplitude θ_l across the cycle count N_a.

As the angle of the lubrication cycle increases, the slope of the torque curves gradually decreases. This trend is evident in the values denoted as N_{4Nm} and presented in Table 6.5, indicating the number of cycles required to surpass the torque limit of 4 Nm. For the reference test, as well as tests No. 1 and No. 1.1, this limit is exceeded in fewer than 3 000 cycles, whereas for test No. 4 and No. 4.1, this limit is reached after more than 12 000 cycles. While

lubrication cycles featuring an angle of $\theta_l \leq 45°$ can extend the time until a specific torque value is attained, they are not capable of entirely preventing damage. Notably, further increasing the angle of the lubrication cycle to $\theta_l = 50°$ leads to a scenario where the torque ceases to exhibit significant increases over the examined experimental period, remaining almost constant beyond 20 000 cycles. Moreover, elevating the angle of the lubrication cycle to $\theta_l = 60°$ yields a torque curve that remains consistently low. The preceding experiments have underscored the growing effectiveness of lubrication cycles in mitigating raceway damage as the oscillation angle θ_l increases. To facilitate subsequent discussions regarding the mechanism responsible for damage prevention, additional experiments are carried out. Firstly, tests will be conducted with half the number of rolling elements to assess the impact of overrolling of adjacent contact areas. Detailed calculations of kinematics, outlined in Section 3.1, will determine the required oscillation angle for contact areas of two adjacent rolling elements to overlap. This occurs when the distance traveled, denoted as the over-rolled path x, on the raceway surpasses the path x_{sep} indicated by the pitch angle between rolling elements. The pitch angle is defined by:

$$\phi_{\text{sep}} = \frac{2\pi}{Z} \tag{6.4}$$

Consequently, the rotation angle of the inner ring $\theta_{\text{overlap,ir}}$ at which the adjacent contact areas on the inner ring start to overlap, and the rotation angle $\theta_{\text{overlap,or}}$ at which the contact areas on the outer ring begin to overlap, can be calculated as follows:

$$\theta_{\text{overlap,ir}} = \phi_{\text{sep}} \cdot \frac{2 \cdot r_{\text{p}} \cdot (r_{\text{p}} - r_{\text{re}} \cdot \cos\alpha)}{r_{\text{p}}^2 - r_{\text{re}}^2 \cdot (\cos^2\alpha)} \approx 45° \tag{6.5}$$

$$\theta_{\text{overlap,or}} = \phi_{\text{sep}} \cdot \frac{2 \cdot r_{\text{p}} \cdot (r_{\text{p}} + r_{\text{re}} \cdot \cos\alpha)}{r_{\text{p}}^2 - r_{\text{re}}^2 \cdot (\cos^2\alpha)} \approx 60° \tag{6.6}$$

Additionally, an exploration into the impact of the cage on lubrication will be undertaken by conducting tests involving both rolling element cages and tests conducted without such cages.

The specific test conditions outlined in Table 6.6 have been derived from the aforementioned considerations. In the nomenclature, 'FC' denotes 'Full Cage',

indicating tests performed with a cage and a complete set of fourteen rolling elements; 'HC' signifies 'Half Cage', representing tests executed with a cage and a half set of rolling elements; 'FNC' and 'HNC' stand for 'Full No Cage' and 'Half No Cage', respectively, representing tests performed with a full set and a half set of rolling elements without a cage. Drawing from the earlier discussed concepts, the rotation angles $\theta_{\text{overlap,ir}}$ and $\theta_{\text{overlap,or}}$ were selected as the oscillation angles for the lubrication cycle. A standardized amount of grease, specifically 10 ml, is employed for all experimental runs. In the case of experiments involving half sets of rolling elements, every second cage pocket is occupied by a rolling element after cleaning, resulting in a bearing configuration with seven rolling elements, each separated by an empty cage pocket. For experiments conducted without cages, a specialized mounting procedure is required. Subsequent to disassembling the bearing for pre-test cleaning, the plastic cage is bisected perpendicular to the bearing's rotational axis using a cut-off grinder. Following reassembly, one half of the cage is placed on the rolling element set as a spacer, while the bearing is greased. The grease maintains the position of the cage halves against the rolling element set during the shaft assembly, ensuring the separation between rolling elements is maintained until the axial load is applied. Following the application of the axial load, the cage halves can be extracted from the bearing through an opening in the test setup. The position of the rolling elements is monitored using a camera. Due to the consistent axial load, the rolling elements maintain their positions during the run-in process and oscillation during the test run, even in the absence of a cage. The occurrence of wear on the raceways prompts some of the rolling elements to shift over time.

Figure 6.38 portrays the torque profiles of tests involving a lubrication cycle with an angle of $\theta_l = 45°$, corresponding to the angle required for overlapping contact areas on the inner ring raceway with a full set of rolling elements ($\theta_{\text{overlap,ir}}$). The vertical axis depicts the relative torque, which is computed by dividing the actual torque value by the mean torque value during the initial 40 oscillation cycles. Notably, the test denoted by the dark blue curve representing 'HNC2' was terminated prematurely due to the detection of significant rolling element migration. Across all tests, torque values exhibit an upward trend over time, indicative of raceway damage. It is noteworthy that the maximum torque attained by tests conducted without a cage (blue curves) surpasses that of tests performed with a cage (green curves).

No.	N_u	θ_l
FC1	100	45
HC1	100	45
FNC1	100	45
HNC1	100	45
FC2	100	60
HC2	100	60
FNC2	100	60
HNC2	100	60

Table 6.6.: Operating parameters for the lubrication cycle tests with different rolling element-cage setups.
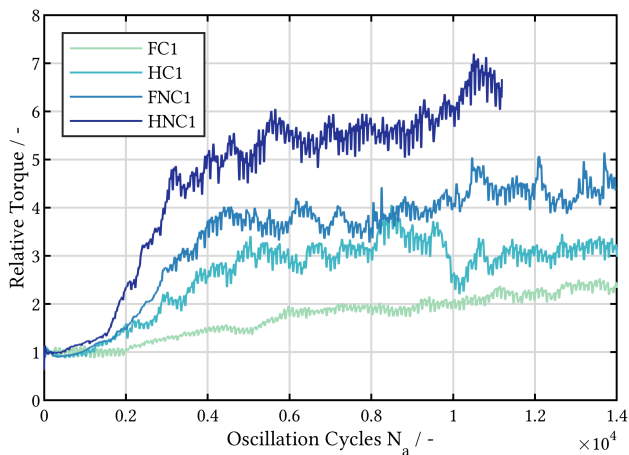
Figure 6.38.: Comparison of the maximum torque curves for tests with lubrication cycles and full (FC1, FNC1) and halved (HC1, HNC1) rolling element sets, as well as with (FC1, HC1) and without (FNC1, HNC1) cages. The angle of the lubrication cycle is $\theta = 45°$. The base cycles have an oscillation angle of $\theta = 15°$ at $f = 3$ Hz.

Figure 6.39 presents the outcomes of tests involving a lubrication cycle with an angle of $\theta_l = 60°$, corresponding to the angle necessary for overlapping outer raceway contact areas with a full set of rolling elements ($\theta_{overlap,or}$). The 'FC2' experiment (light green) reveals that the lubrication cycle proves highly

effective for a full set of rolling elements with a cage, resulting in minimal torque increase over the tested time span. In contrast, test 'HC2' (dark green) involving a halved rolling element set exhibits nearly a twofold increase in torque. This suggests that reducing the rolling element set has an adverse impact. A comparison between tests 'FC2' and 'FNC2' involving a full set of rolling elements indicates that the absence of a cage also detrimentally affects lubrication. In test 'FNC2', the rolling elements were observed to migrate and contact each other after a relatively brief period. Notably, the most substantial torque increase is demonstrated by the 'HNC2' experiment.
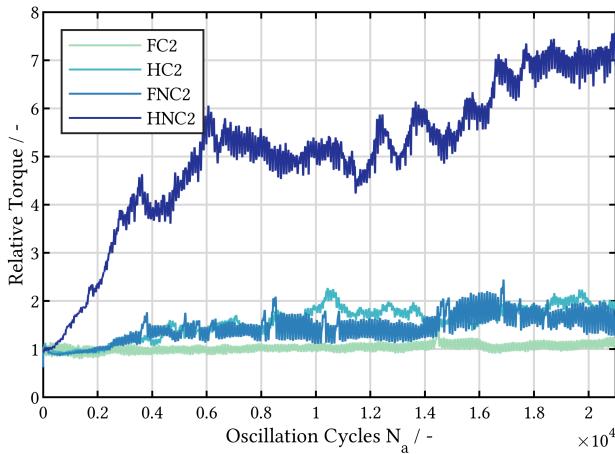
Figure 6.39.: Comparison of the maximum torque curves for tests with lubrication cycles and full (FC2, FNC2) and halved (HC2, HNC2) rolling element sets, as well as with (FC2, HC2) and without (FNC2, HNC2) cages. The angle of the lubrication cycle is $\theta = 60°$. The base cycles have an oscillation angle of $\theta = 15°$ at $f = 3\,\mathrm{Hz}$.

The obtained test results suggest that the bearing cage plays a crucial role in facilitating lubricant supply to the raceway contacts of the rolling elements. While a potential positive impact resulting from the overlapping of adjacent contact areas on the inner ring cannot be dismissed, the upcoming experiments specifically focus on exploring the beneficial influence of the cage.

To comprehensively understand the interaction between the cage and the rolling elements, a thorough examination of the bearing's kinematics is required. Figure 6.40 provides a proportional cross-sectional view of the bearing cage and rolling elements. The cross-sectional plane is inclined at an angle $\beta = 43.84°$ relative to the plane perpendicular to the inner ring's rotational axis, as depicted in the upper left corner. This inclination angle of $\beta = 43.84°$ arises from the inclination of the resultant rotation axis of the rolling element, as determined by Equation 3.8. Notably, the rotation axis of the rolling element is perpendicular to the plane of the image.

Figure 6.40 highlights three distinct angles. The angle γ_b represents the degree of rotation of the rolling element around the axis β during the basic oscillation cycle (in this instance, $\theta_b = 15°$), as depicted in Figure 6.36. On the other hand, $\gamma_{l,Im,ir}$ and $\gamma_{l,Im,or}$ indicate the angles required for a lubrication cycle to fully immerse the swept area on the rolling element's surface during the base cycle within the cage. As illustrated in Figure 6.36, it holds that $\gamma_{l,Im,or} > \gamma_{l,Im,ir}$ for the given cage. Consequently, once $\gamma_l > \gamma_{l,Im,or}$, both contact areas on the rolling element are entirely immersed within the cage during an oscillation cycle.

Figure 6.40.: Sectional view of the rolling element set with the manufacturer's cage ('OEM') through the center of the rolling element, perpendicular to the axis of the resulting angular velocity of the rolling element ω_{RE}.

Utilizing the equations outlined in Section 3.1, we can establish a relationship between the angular velocity of the inner ring Ω_{ir} and the resulting angular velocity of the rolling element in the context of the cage-relative system ω_{re}. This relationship is given by:

$$i_{re} = \frac{\omega_{re}}{\Omega_{ir}} = 2.47 \tag{6.7}$$

From the oscillation angle of the base cycle θ_b and the transmission ratio i_{re}, the angle $\gamma_b = 37.05°$ can be determined. Employing the cage geometry, we can subsequently deduce the following angles: $\gamma_{l,Im,or} = 110.34°$, $\gamma_{l,Im,ir} = 91.61°$, $\gamma_{Cage,or} = 146.59°$, and $\gamma_{Cage,ir} = 109.13°$. With the transmission ratio i_{re}, the corresponding angles for the inner ring can be derived:

$$\theta_{l,Im,ir} = \frac{\gamma_{l,Im,ir}}{i_{re}} = 37.09° \tag{6.8}$$

$$\theta_{l,Im,or} = \frac{\gamma_{l,Im,or}}{i_{re}} = 44.67° \tag{6.9}$$

$$\theta_{cage,ir} = \frac{\gamma_{cage,ir}}{i_{re}} = 44.25° \tag{6.10}$$

$$\theta_{cage,or} = \frac{\gamma_{cage,or}}{i_{re}} = 59.35° \tag{6.11}$$

To ensure complete immersion of the contact track on the rolling element within the cage for a base oscillation with angle θ_b, the lubrication cycle must have an angle $\theta_l > 45°$. The findings depicted in Figure 6.36 reveal that lubrication cycles with an angle of $\theta_l = 50°$ have proven to be very effective. When considered in conjunction with the tests conducted involving cages, both with and without reduced rolling element sets, these results suggest that the cage plays an important role in facilitating lubrication of the rolling contact, particularly when the oscillation angle is substantial enough to enable interaction of the contact area with the cage.

To experimentally validate the hypothesis regarding cage influence, a modified cage (KV1) has been developed and subjected to testing under comparable operational conditions. Figure 6.41 provides a scaled representation of the

	OEM	KV1
$\theta_{\mathrm{l,Im,OR}}$	44.67°	24.7°
$\theta_{\mathrm{l,Im,IR}}$	37.09°	21.08°
$\theta_{\mathrm{Cage,OR}}$	59.35°	24.7°
$\theta_{\mathrm{Cage,IR}}$	44.25°	21.08°

Table 6.7.: Comparison of the relevant angles for relubrication through cage interaction between the OEM cage and the 3D-printed design KV1.

newly designed cage within the same sectional plane as the original cage illustrated in Figure 6.40.

To assess the effectiveness of the newly designed cage (KV1), the tests are replicated using a base oscillation cycle of $\theta_{\mathrm{b}} = 15°$, along with lubrication cycles featuring angles of $\theta_{\mathrm{l}} = 30°, 33.75°, 37.5°, 45°$, all utilizing the KV1 cage design. The selection of the total number of oscillation cycles N_{a} mirrors that of equivalent tests conducted with the manufacturer's (OEM) cage.

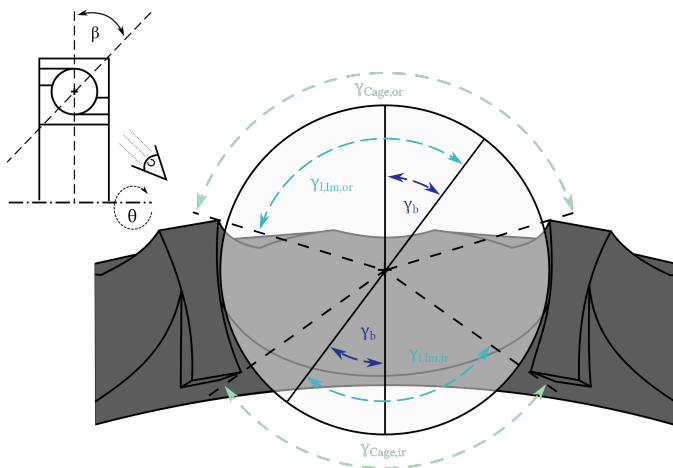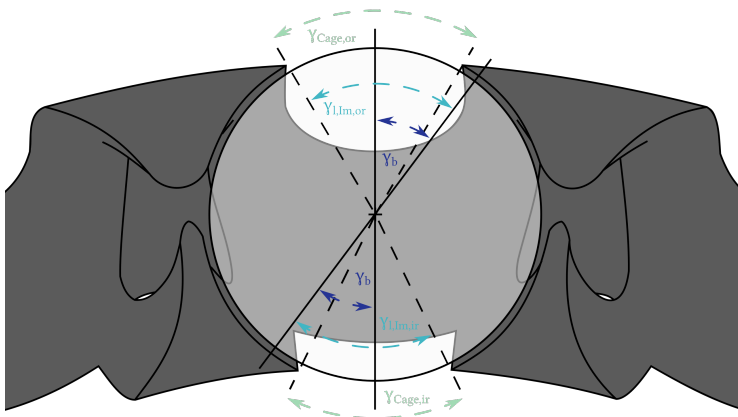**Figure 6.41.:** Sectional view of the rolling element set with the cage 'KV1' through the center of the rolling element, perpendicular to the axis of the resulting angular velocity of the rolling element ω_{RE}.

Figure 6.42 presents a comparative analysis of the torque curves obtained from tests conducted using the OEM cage and the newly designed cage variant KV1. The distinct trend is evident: the KV1 cage variant effectively prevents torque escalation and consequently premature wear initiation across all examined lubrication cycle angles θ_l. This series of investigations underscores the pivotal role that the cage plays in influencing the lubrication of the rolling contacts.
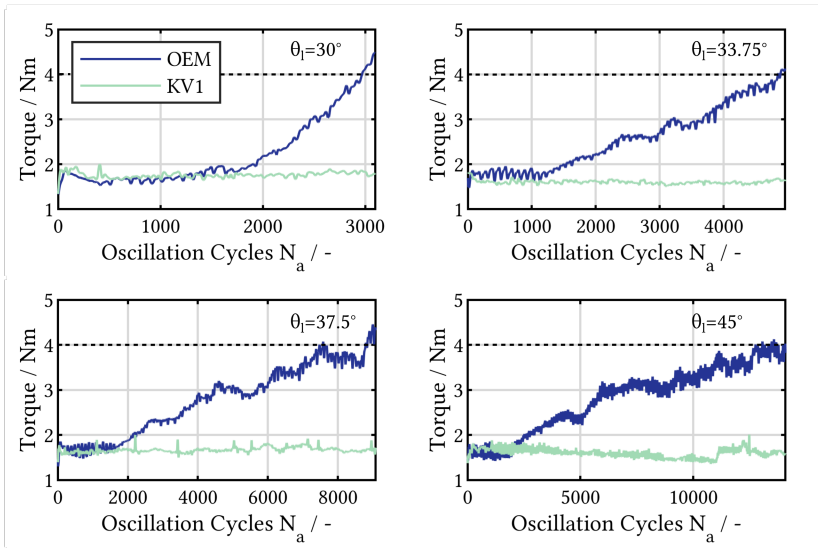
Figure 6.42.: Comparison of the torque curves with integrated lubrication cycles between the manufacturer's cage 'OEM' (blue) and the cage variant KV1 (green). The curves are presented for a number of uninterrupted base cycles $N_u = 100$ and lubrication cycle angles $\theta_l = 30°, 33.75°, 37.5°, 45°$.

6.3.2. Bearing Tests - Cage Designs

Section 6.3.1 demonstrated how an optimized cage design can effectively prevent early wear initiation. The aim of this section is to identify how long wear initiation can be delayed and how the cage design can be further optimized. In this pursuit, various cage configurations are presented in greater

detail. Furthermore, an examination is conducted involving a variant where the OEM cage is sealed using two shields, thereby gauging whether a cage that comprehensively envelops the rolling element is indispensable, or if a simple seal can serve the same purpose.

Figure 6.43 offers a visual representation of the various cage variants under investigation. The upper image presents the OEM cage variant in a 3D view, with rolling elements inserted, featuring a one-piece window cage design. This particular variant is used both with and without shielding in the tests. A sectional view through a plane parallel to the bearing's rotational axis is shown on the right. Furthermore, a cross-section of the cage perpendicular to the rolling axis of the rolling element, intersecting its center, is displayed in Figure 6.40. The images below showcase the KV1 cage variant, a 3D-printed snap cage design. A cross-sectional view of the cage, perpendicular to the rolling axis of the rolling element through its center, is depicted in Figure 6.41. Cage variant KV2 shares core similarities with KV1 but includes an extension in the form of a cover that can be attached to the open front side of the cage, effectively enveloping the rolling element from multiple directions. This modification is intended to accommodate scenarios where the actual axis of rotation of the rolling element may deviate from the theoretically calculated axis. Cage variant KV3 introduces a slight adjustment to KV2, featuring shielding lips on both sides of the cage to prevent lubricant leakage.

OEM (+ Sealing)

KV1

KV2

KV3
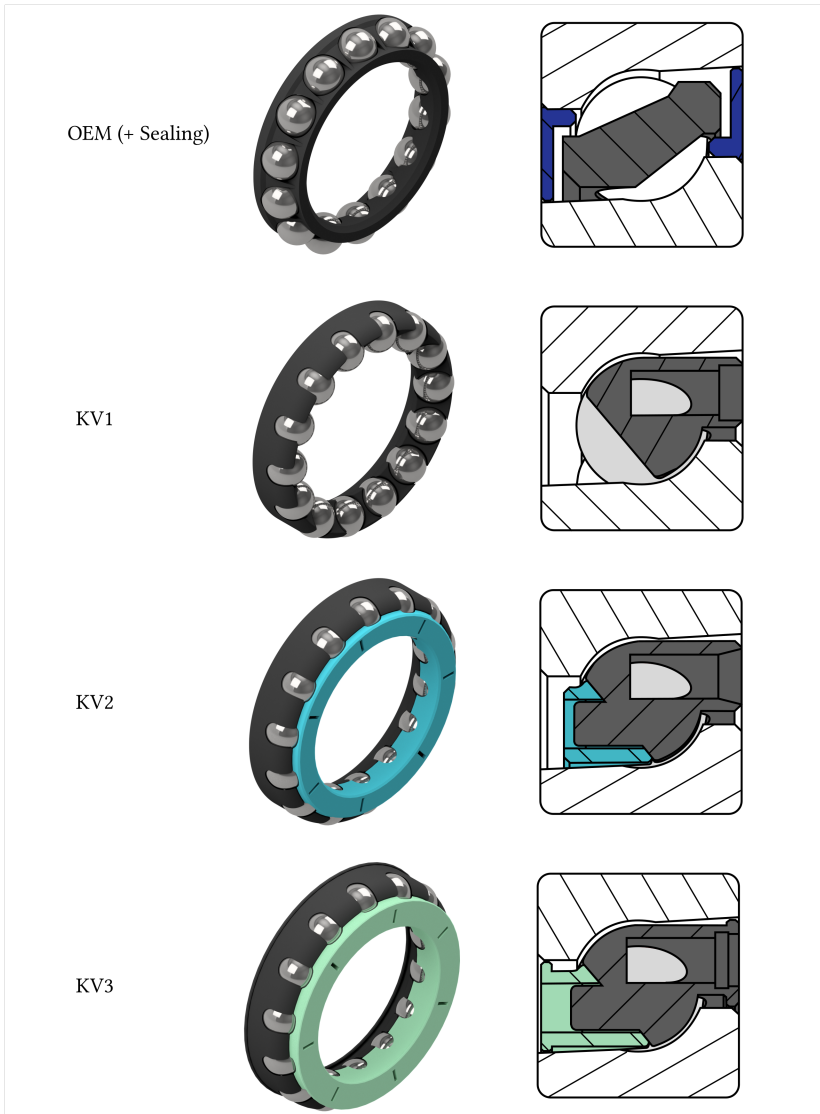
Figure 6.43.: Illustration showcasing the various cage variants utilized.

To begin, a detailed analysis of the test results is conducted for both the OEM cage with and without shielding, as well as for the initial cage variant KV1. The torque curves of the performed tests are presented in Figure 6.44. The dark blue curve represents the reference test conducted with the OEM cage without shielding. Notably, the torque curve exhibits a substantial increase starting at approximately 8 000 cycles and reaches approximately 9 Nm over the course of the 80 000-cycle test duration. The two turquoise curves depict the torque curves at the onset of the tests involving the OEM cage with shielding. It is observed that the torque increase commences around a similar cycle count as the reference test. However, the torque curves initially exhibit a rise to a maximum of roughly 3.5 Nm, which is then followed by a sustained plateau. In contrast, the tests utilizing the KV1 cage variant demonstrate no noticeable torque escalation during the initial 80 000 cycles.
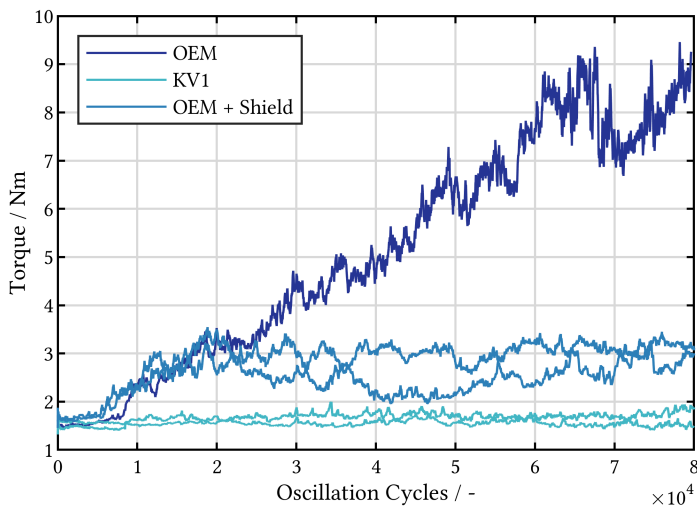
Figure 6.44.: Comparison of torque curves of the tests at $f = 3\,\text{Hz}$ and $\theta = 30°$ conducted with the OEM cage, cage variant KV1, and the OEM cage with shielding.

To further investigate the factors contributing to the torque increase, an additional test was performed using the OEM cage with shielding and the KV1 cage variant. These tests were disassembled shortly after the observed

torque escalation in the tests with the OEM cage and shielding. The disassembly procedure was conducted with careful precision to minimize bearing movement, facilitating a detailed analysis of grease distribution within the bearing. Subsequently, damage marks were examined under an optical microscope. Upon inspecting the distribution of the damage marks, as shown in Figure 6.45, intriguing patterns emerge. Notably, when utilizing the OEM cage with shielding, significant damage was observed on the raceway, particularly at the upper section of the bearing. In contrast, the KV1 cage variant exhibits localized damage on the raceway, but this damage appears randomly distributed around the bearing's circumference and is less severe in nature. This distinct distribution of damage marks is consistently observed across other tests as well. For all alternative cage variants, the damage marks are relatively evenly spread around the bearing's circumference.
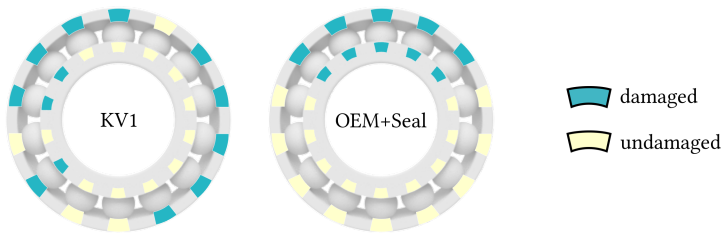
Figure 6.45.: Comparison of the distribution of damage marks on the raceway of the load-side bearing for a test with cage variant KV1 (left) and OEM cage with shielding (right) after $N_a = 7\,000$ cycles. Raceway areas on which corrosive damage could be detected are colored in turquoise, while undamaged areas are colored in yellow. The severity of the damage is not assessed in this context.

Figure 6.46 illustrates the distribution of grease on the raceways following the disassembly of the bearings. The left side of the figure displays images of the raceway of the bearing with cage variant KV1, while the right side features images of the bearing with OEM cage and shielding. The upper half of the figure presents four pictures, each depicting the contact areas of the uppermost contact region on the inner and outer rings. Upon comparing the top two images, specifically those depicting the contact area on the outer ring of the uppermost contact region, a noticeable distinction becomes evident. The region devoid of grease due to the presence of the rolling element is notably

more extensive for the OEM cage with shielding (on the right) compared to the test utilizing cage KV1 (on the left). In the KV1 case, some areas still contain grease reservoirs that protrude into the contact region. A similar observation holds when contrasting the images of the second row, which represent the inner ring of the uppermost contact region. Again, the zone lacking grease is considerably more pronounced for the OEM cage with shielding compared to the KV1 cage. This pattern aligns with the distribution of the observed damage, which is more significant on the right side (OEM cage with shielding) than on the left side (KV1 cage). In contrast, at the lowest contact area of the bearing, the scenario is reversed. The grease distribution for cage KV1 closely resembles that observed at the uppermost contact region. Conversely, large quantities of grease are present on the raceways for the OEM cage with shielding, indicating that the grease has migrated downward over time due to bearing movement in combination with gravity. Consequently, even in the extended tests utilizing the OEM cage and shielding, damage is primarily localized to the upper contact regions.
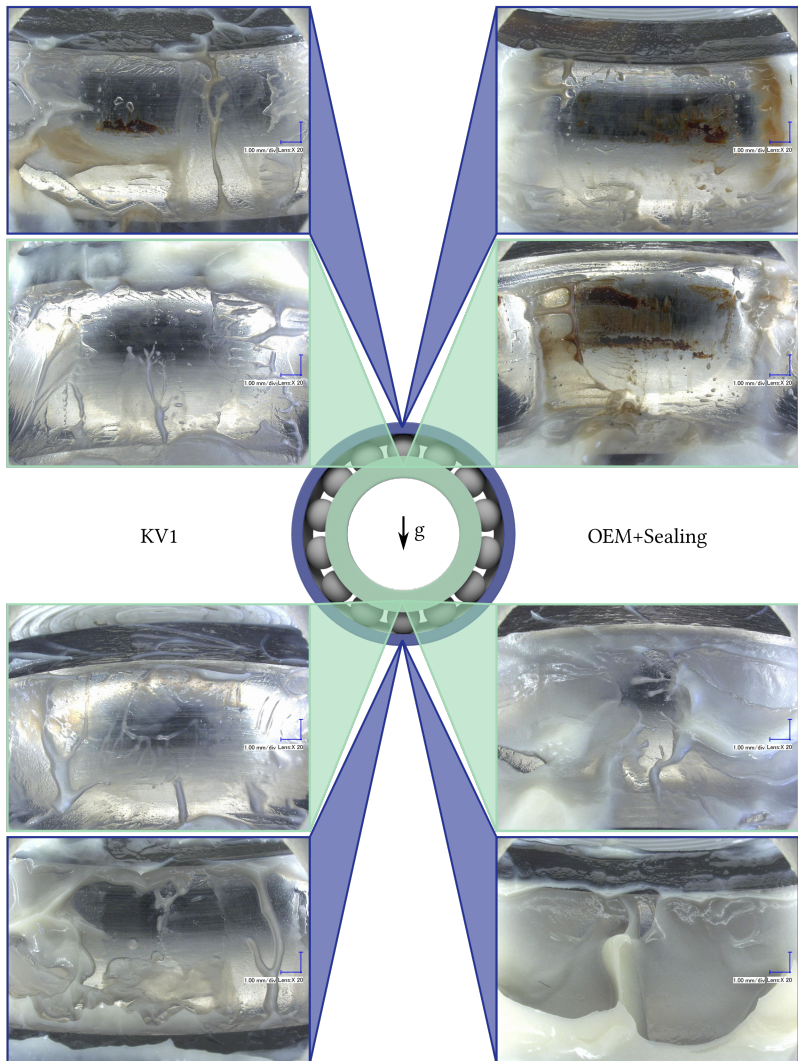
Figure 6.46.: Comparison of grease distribution after a test with the OEM cage and shielding on the right and the KV1 cage variant on the left. Depicted are the contact areas on the inner ring (outlined in green) and on the outer ring (outlined in blue) at the uppermost and lowermost contact points of the bearing, respectively.

Figure 6.47 contains the torque curves of the tests with the OEM cage and the cage variants KV1 and KV2. Here it can be seen that although the torque curve of KV1 does not increase right at the start, as is the case with the OEM cage with shielding, it begins to rise steeply at a certain point, while one of the tests with shielding remains at a relatively constant level over a period of 1 million cycles. The other shielded test rises more sharply because one of the shields was not seated optimally and grease was able to leak from the underside. In this case, the damage spread further down in the bearing. The lowest contact areas were still undamaged.

The torque curves of the tests with cage KV2 show a qualitatively similar course to the tests with cage KV1. However, the number of cycles until damage initiation can be increased fivefold. After about 5 million cycles, both curves rise steeply and top the test with OEM cage and intact shielding towards the end of the tests.
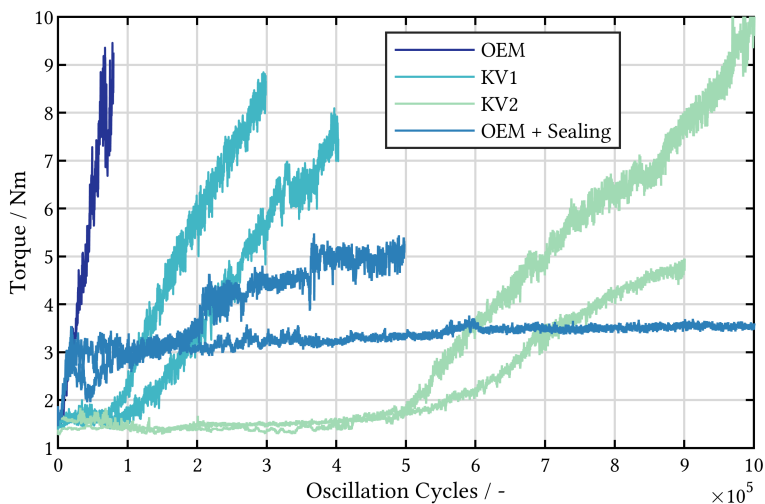
Figure 6.47.: Torque curves of the tests at $f = 3\,\text{Hz}$ and $\theta = 30°$ with the OEM cage, with and without shielding, and the cage variants KV1 and KV2.

The KV3 cage variant represents an expansion of the KV2 variant, enhancing it with narrow shielding gaps on both sides of the cage. This variant aims to

combine the advantages observed in bearings with shielding and those with a cage design that encases the rolling element.

In Figure 6.48, the results of the reference test using the OEM cage, as well as the test involving the OEM cage with shielding, are presented alongside the outcomes for cage variants KV1, KV2, and KV3.
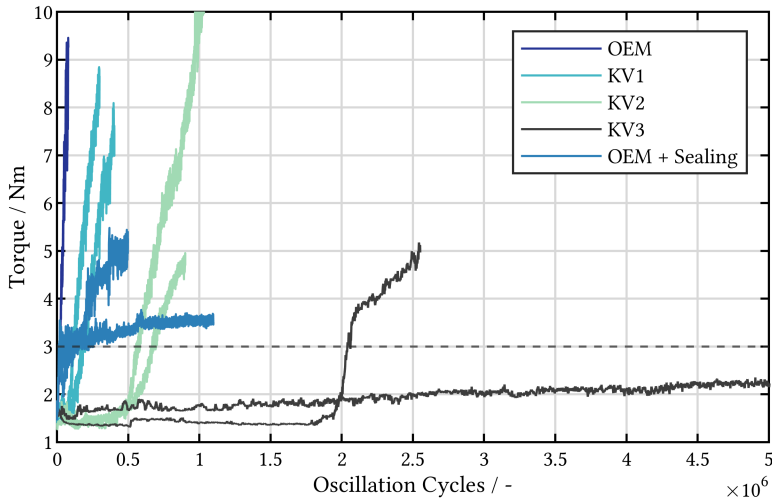
Figure 6.48.: Torque curves of the tests at $f = 3\,\text{Hz}$ and $\theta = 30°$ with the OEM cage, with and without shielding, and the cage variants KV1, KV2, and KV3

To quantitatively assess the significance of the cage's impact on the onset of raceway damage, the cycle thresholds at which a peak torque of 3 Nm is exceeded are presented in Table 6.8. For tests using the manufacturer's (OEM) cage, as well as tests employing both the OEM cage and shielding, the torque threshold is surpassed before reaching 17 000 cycles. In the case of the cage variant KV1, this metric demonstrates an augmentation of up to tenfold, extending to 178 881 cycles. Through the adoption of the KV2 variant, the cycle threshold can be extended to surpass 500 000 cycles. Notably, the KV3 variant achieves a cycle threshold exceeding 2 million cycles in one test, while in the other, no threshold is reached during a runtime exceeding 5 million

No.	Cage Variant	N_a	N_{3Nm}	T_{max}/Nm
0	OEM	79 639	16 879	9.46
1.1	OEM + Sealing	497 967	12 825	5.48
1.2	OEM + Sealing	1 098 265	16 620	3.77
2.1	KV1	298 553	113 771	8.85
2.2	KV1	402 692	178 881	8.09
3.1	KV2	900 699	666 362	4.95
3.2	KV2	1 219 928	556 429	14.21
4.1	KV3	2 551 500	2 061 400	5.18
4.2	KV3	5 018 500	-	2.35

Table 6.8.: Test results of the bearing tests with different cage designs for an oscillation angle of $\theta = 30°$ at $f = 3\,Hz$: N_a - total number of oscillation cycles; N_{3Nm} - number of cycles until a torque limit of 3 Nm is exceeded; T_{max} - maximum torque reached.

cycles. In comparison to the OEM cage, the KV3 cage variant effectively delays the initiation of damage by a factor exceeding 100.

6.3.3. Model Experiments - Cage Influence

In the preceding sections (Section 6.3.1 and 6.3.2), angular contact ball bearing tests have demonstrated the pivotal role of the cage in influencing lubrication conditions within the contact area during oscillating operations. This section delves further into this influence by conducting investigations using model experiments on the optical EHL (Elastohydrodynamic Lubrication) tribometer. To achieve this objective, the original experimental setup of the test rig is equipped with a 3D-printed component that emulates the cage within the bearing assembly. Figure 6.49 visually illustrates the assembly, depicting the original setup with V-groove bearings and a rolling element on the left without the simulated cage, and on the right, with the simulated cage included. To examine this influence, a series of tests is conducted on both setups, encompassing varying oscillation angles and different types of lubricating greases.

Variant without Cage   Variant with Cage
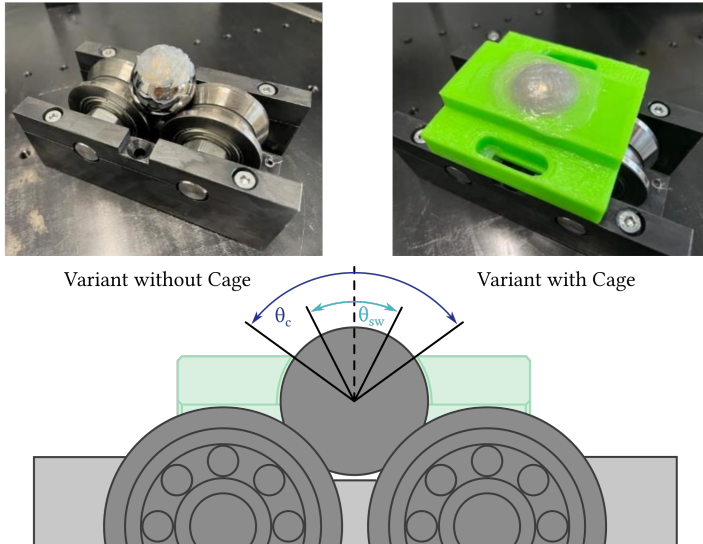
Figure 6.49.: Rolling element mounted on the V-groove bearings without a simulated cage (top left) and with a simulated cage (top right). The illustration in the lower half of the image depicts a longitudinal section through the assembly of V-groove bearings, rolling element, and cage to illustrate the angles θ_{sw} and θ_c.

Prior to the experiments, lubricant is uniformly applied to the cleaned glass disc and the cleaned rolling element. A consistent 1 mm-thick grease layer is spread onto the underside of the glass disc using a plastic slider. Similarly, a lubricant layer of approximately 1 mm height is applied to the upper quarter of the rolling element. It is important to note that the contact region between the rolling element and the V-groove remains devoid of lubrication to ensure rolling motion. Subsequently, the rolling element is pressed against the glass disc with a normal force of 45 N, inducing a maximum contact pressure of $p_{max} = 590$ MPa. For the experiment, a constant oscillation angle and frequency are sustained for a duration of $N = 3\,000$ oscillation cycles. The oscillation frequency, set at $f = 1$ Hz, remains consistent across all experiments. The experiment's parameter matrix is outlined in Table 6.9. The topmost row designates the types of lubricating greases under investigation. The first column presents the distances x traversed by the contact center during the

	IS1		IS2		O1		O2	
Distance x	Cage	No Cage	Cage	No Cage	Cage	No Cage	Cage	No Cage
6 mm	N	N	N	N	N	N	N	N
12 mm	N	N	N	N	N	N	N	N
18 mm	N	N	N	N	N	N	N	N
24 mm	N	N	N	N	N	N	N	N
30 mm	N	N	N	N	N	N	N	N

Table 6.9.: Test matrix for the experiments investigating the impact of the cage on the lubrication condition of the rolling contact on the EHL tribometer. Total number of oscillation cycles: $N = 3\,000$.

Oscillation Angle/ °		5.1	10.2	15.3	20.5	25.7
Distance x/ mm		6	12	18	24	30
Amplitude ratio $e = \frac{x}{2b}$/ -		15.8	31.5	47.2	63.0	78.7

Table 6.10.: Oscillation angles used in the experiments on the EHL tribometer and the resulting amplitude ratios.

experiments with different oscillation angles, as detailed in Table 6.10. For every combination of grease type and distance x, two tests with the cage, denoted as 'Cage', and one test without the cage, denoted as 'No Cage', are executed. When employing the cage in the tests, the average value derived from both trials is considered the outcome for the measurement of the lubricant film height.

The amplitude ratio values presented in Table 6.10 are derived from the displacement of the contact center relative to the rotational axis of the glass disc, as well as the width of the HERTZian contact denoted as $2b$. Some of these values are notably greater than those observed in the component-level tests. Nonetheless, given the primary focus on examining the influence of the cage, the significance of the amplitude ratio is of minor importance in the context of this investigation.

Similar to the cage designs shown in Section 6.3.2, an angle θ_{sw} and a critical angle θ_c can be calculated for the simulated cage within the context of the EHL tribometer. These angles are visually depicted in Figure 6.49. Specifically, θ_{sw} denotes the maximal angle at which, theoretically, no part of the track enters the cage. This angle corresponds to a rolling distance of $x_{sw} = 12$ mm.

Conversely, θ_c signifies the angle from which the entire track becomes fully immersed within the cage's enclosure during an oscillation. This critical angle corresponds to a covered distance of the contact center of $x_c = 24$ mm. These boundaries are illustrated by dashed horizontal lines in Table 6.9.
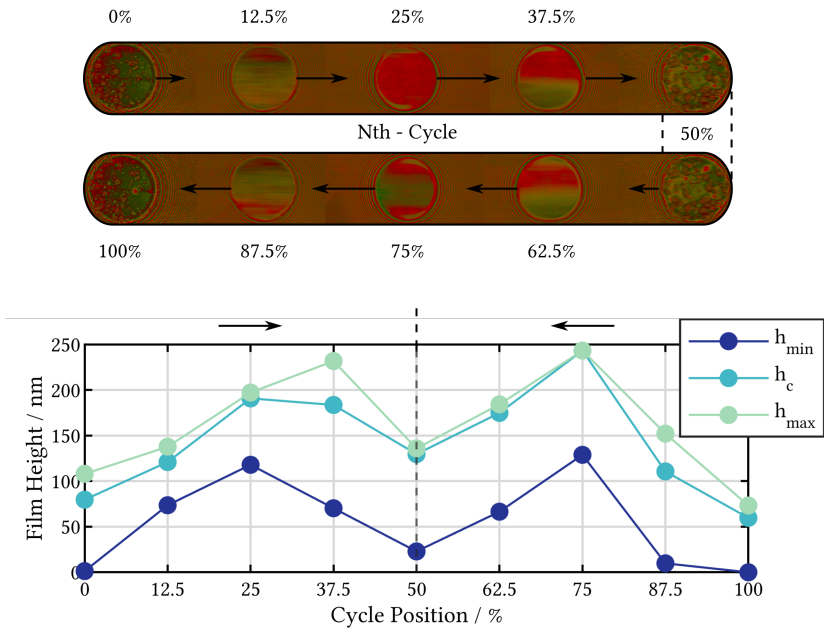
Figure 6.50.: Description of the evaluation methodology for the experiments investigating the impact of the simulated cage on the lubricant film height in the rolling contact. The upper section illustrates the positions in the oscillation cycle where the lubricant film heights are measured, while the lower section illustrates the measurements of the minimum (h_{min}), central (h_c), and maximum (h_{max}) lubricant film heights at each corresponding position.

The assessment of the tests involves the examination of lubricant film heights at nine specific points throughout an oscillation cycle. Figure 6.50 provides a visual representation of the designated points where lubricant film heights are measured. The upper portion of the figure illustrates the 1 000th oscillation cycle of the experiment employing grease O1 and the simulated cage at an

oscillation distance of $x = 30\,\text{mm}$, serving as an illustrative example. Within this cycle, the contact area is analyzed at the onset of oscillation (0% of the cycle path), as well as at the intervals of 12.5%, 25%, and 37.5% during the rightward motion, indicated by the black arrows. Similarly, measurements are taken at the reversal point (50% of the cycle path) and the points of equal velocity during the return motion. These measurements encompass the minimum lubricant film height (h_{min}), central lubricant film height (h_c), and maximum lubricant film height (h_{max}) within the contact region. These points are then plotted on a diagram, as exemplified in Figure 6.50. In order to observe the temporal evolution of lubricant film heights at the selected points, evaluations are performed after 200, 600, 1 000, 1 200, 1 400, 2 000, and 3 000 oscillation cycles. The results indicate that a steady-state condition for the measured lubricant film heights is established after 1 000 cycles, within the investigated period. Consequently, the subsequent analyses showcase results from the 1 000th oscillation cycle for each case, in order to highlight the influence of the simulated cage on the lubrication state of the rolling contact.

The impact of the simulated cage on the lubrication condition becomes evident through Figure 6.51. This figure comprises three plots, illustrating lubricant film heights as a function of the oscillation distance x along the x-axis and the contact position within the oscillation cycle. The color-coded data points indicate distinct contact positions. Points with equivalent velocity during the oscillation cycle share the same color. Solid lines connect the points representing measured film heights, while dashed lines connect the triangular markers representing film heights calculated according to the Hamrock and Dowson. The upper plot depicts the central lubricant film heights (h_c) for a test conducted without the simulated cage, utilizing grease O1. The lower two plots showcase tests under similar conditions, conducted with the simulated cage. The vertical dashed lines denote the distances x_{sw} and x_c prescribed by the cage.

Upon comparing the results for distances $x = 6\,\text{mm}$ and $x_{\text{sw}} = 12\,\text{mm}$ — where the cage's influence is anticipated to be negligible — it is evident that the measured lubricant film heights remain below 50 nm in all three tests and at all oscillation cycle positions, with the exception of a single point at $x = 6\,\text{mm}$ and 0% of the cycle path. At $x = 18\,\text{mm}$, discernible increases in certain lubricant film heights can be attributed to the presence of the simulated cage. Notably, substantial increases in lubricant film height are observed in specific instances, particularly at points representing 0%, 12.5%, 37.5%, 62.5%, and

87.5% of the oscillation cycle. From a distance of $x_c = 24$ mm, up to a tenfold increase in lubricant film height is observed across various positions within tests employing the cage. However, for the first test with the cage (middle chart), this effect is less pronounced at the 25%, and 75% positions of the cycles than for the second test (bottom chart). At the overcritical distance of $x = 30$ mm, substantial increases in lubricant film height are observed in these positions.

Figure 6.52 illustrates the impact of the cage on the central lubricant film height for the tested greases: O1, O2, IS1, and IS2. Unlike Figure 6.51, these plots show the difference Δh_c in the central lubricant film height between tests conducted with and without the simulated cage. Overall, it is clear that the cage positively affects the lubricant film height from a distance of $x_c = 24$ mm, spanning across various positions and greases. Furthermore, a positive impact on the lubricant film height is observed at the midpoint positions (25% and 75%) for all greases except IS2, particularly at $x_c = 30$ mm. Similarly, a favorable influence on the 12.5%, 37.5%, 62.5%, and 87.5% positions becomes evident, usually manifesting at a distance of $x_c = 18$ mm. Remarkably, in the case of grease O2, the cage results in a significant elevation of the lubricant film height at positions 12.5%, 37.5%, 62.5%, and 87.5%, as well as at the reversal points, excluding the 25% and 75% positions.

Moving from a distance of $x_c = 24$ mm to $x_c = 30$ mm leads to a decrease in lubricant film height at the 12.5%, 37.5%, 62.5%, and 87.5% positions, while an increase is observed at the 25% and 75% positions. For greases O2 and IS1 a positive effect of the cage on lubricant film height can be observed, even at the smaller distance of $x_{sw} = 12$ mm. Interestingly, at the minimal distance of $x_{sw} = 6$ mm, discernible differences in measured lubricant film heights are apparent. In the case of grease IS2, the cage seems to have a favorable impact on lubricant film heights at the 12.5%, 37.5%, 62.5%, and 87.5% and at the 25%, and 75% positions, even at this smaller distance. Conversely, an opposing effect is seen with grease IS1, where negative differences emerge in lubricant film heights at one of the reversal points and the 12.5%, 37.5%, 62.5%, and 87.5% positions. It is also noteworthy that the cage's influence is particularly pronounced at the reversal points for grease IS1, yielding exclusively positive and remarkably substantial differences.

To determine whether the variation in lubricant film height, attributed to the cage, is primarily influenced by the base oil or also affected by the thickener, the results are depicted in Figure 6.53, relative to the calculated lubricant

film height according to Hamrock and Dowson. More precisely, the plot illustrates the difference in the central lubricant film height Δh_c relative to the calculated maximum central lubricant film height according to Hamrock and Dowson ($h_\mathrm{c,hd,max}$) at the position of the highest entrainment speed, corresponding to the respective oscillation distance. This normalization procedure enables the assessment of whether the alteration in lubricant film height could potentially be attributed solely to the base oil. In this context, values of $\frac{\Delta h_\mathrm{c}}{h_\mathrm{c,hd,max}} \leq 1$ indicate that the observed variations fall within the scope of influence of the base oil itself. Values exceeding 1 suggest that the presence of the thickener contributes to the observed effects on the lubricant film height.

Upon evaluating the results for greases O1 and O2, it is evident that the relative change in lubricant film height remains below 1. This relative change consistently increases with the oscillation distance. Conversely, for greases IS1 and IS2, the relative changes are notably larger, with the cage enabling a three- to fivefold increase in the relative central lubricant film height.
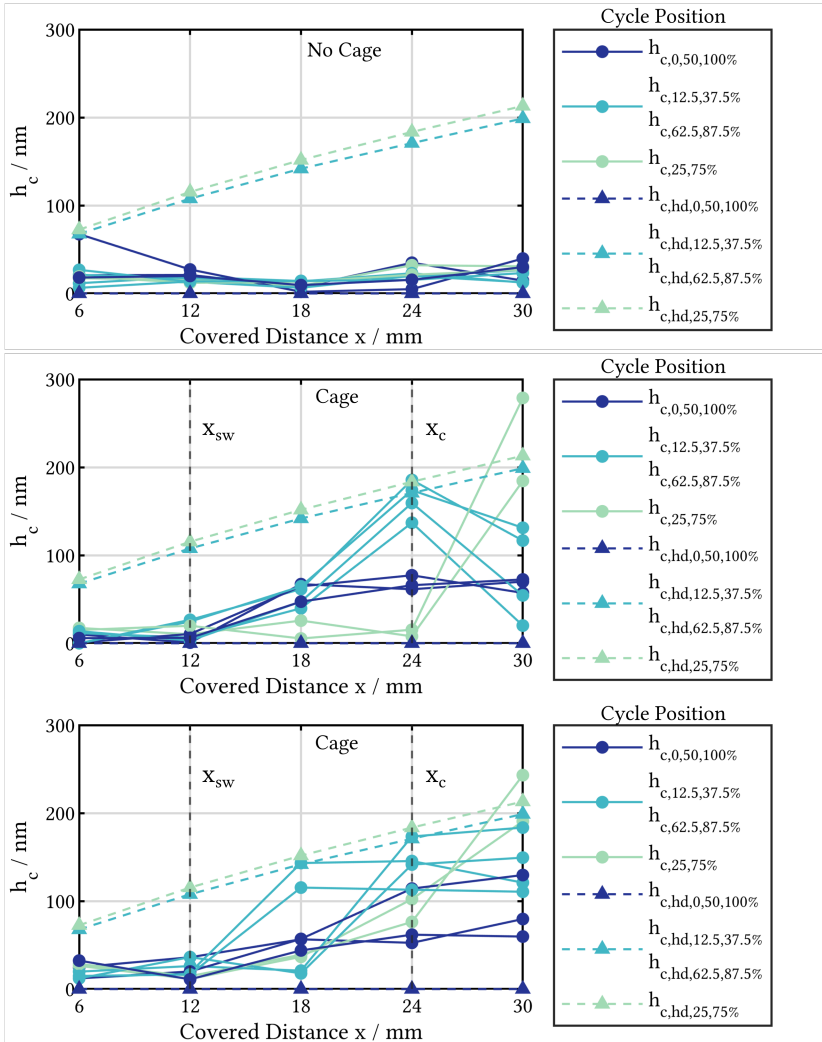
Figure 6.51.: Comparison of the measured central lubricant film height h_c on the EHL tribometer for the model grease O1. The upper diagram displays the results without a simulated cage, while the lower diagrams depict two tests conducted under the same conditions using the simulated cage. The dots connected by solid lines represent the measured film heights, while the dashed lines indicate the film heights calculated according to the HAMROCK AND DOWSON model.
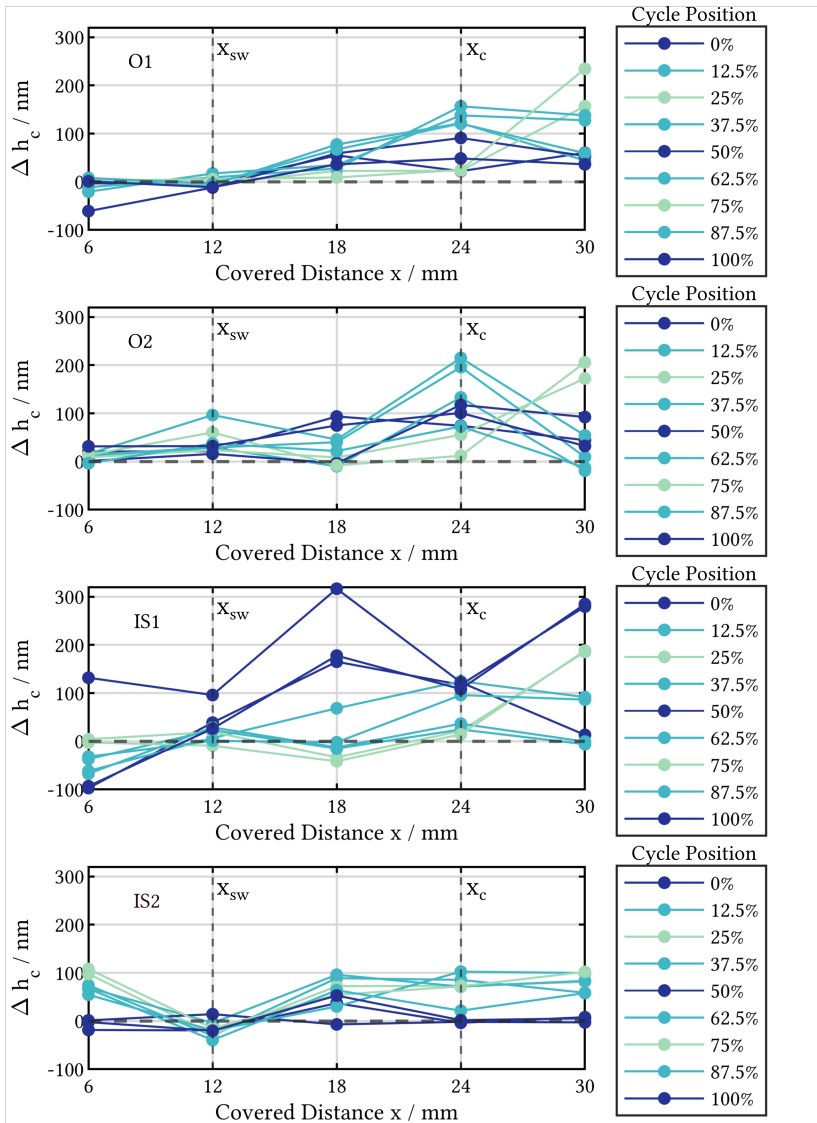
Figure 6.52.: Comparison of the difference in central lubricant film height Δh_c with the use of the cage. The four diagrams display the results for the greases O1, O2, IS1, and IS2.
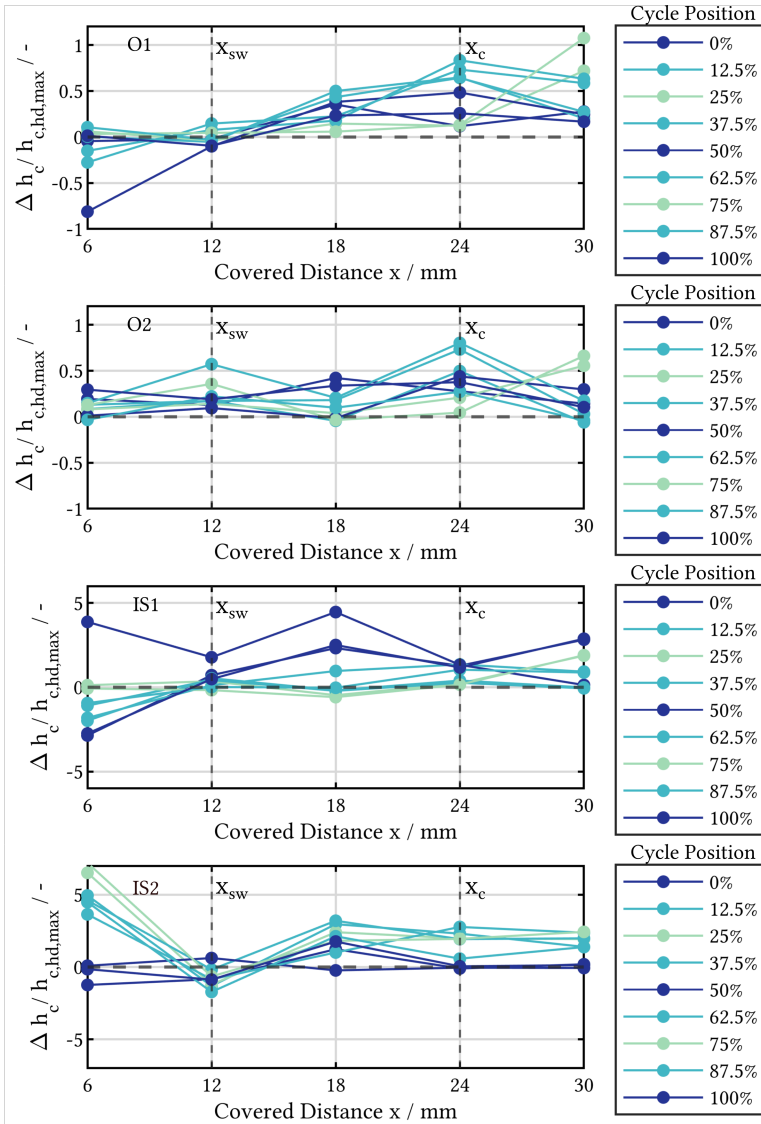
Figure 6.53.: Comparison of the difference in central lubricant film height Δh_c relative to the central film height $h_{c,hd,max}$ at maximum entrainment speed calculated according to HAMROCK. The four diagrams present the results for the greases O1, O2, IS1, and IS2.

6.4. Complementary Investigations

This chapter summarizes additional research that serves to support hypotheses that will later be the basis for the starvation model.

Oil lubrication

Up until now, all conducted experiments have been centered around grease as the chosen lubricant, given its prevalence in numerous applications. To highlight the lubrication effects of pure oil under the specified testing conditions, the trials underlying the CoF mapping utilizing grease IS1, as detailed in Section 6.1.1, are replicated using the well-known reference oil FVA3 [67]. These tests are executed under a maximum contact pressure of $p_{max} = 2$ GPa. Similar to the IS1 experiments, unsealed bearings are employed in the oil tests. In this context, each bearing mounted on the shaft is lubricated with 5 ml of FVA3 through a syringe, ensuring that all rolling elements are immersed in oil. Due to its liquid nature, a substantial portion of the oil does not adhere to the bearings, unlike grease. Consequently, the effective quantity of oil present within the bearing post-mounting is considerably diminished.
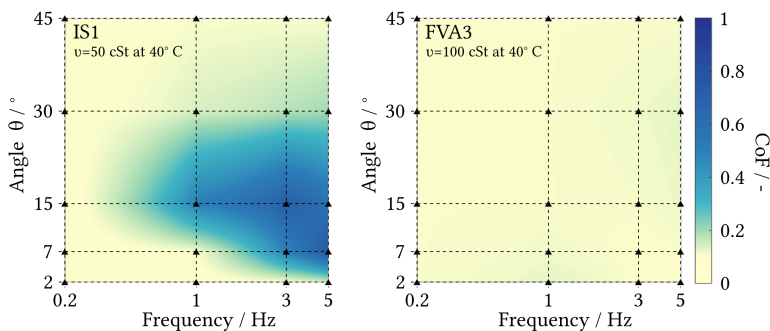
Figure 6.54.: Comparison of the coefficient of friction (CoF) maps after 4 000 oscillation cycles with grease IS1 (left) and oil FVA3 (right) at a constant maximum pressure of 2 GPa.

As evident from the data, the oil-based experiments were exclusively conducted within the frequency range of 0.2-5 Hz and angular displacement

range of 2-30°. This range was particularly relevant as it aligned with the region identified as prone to damage in the grease-based tests. However, it's important to note that unlike the grease tests, all the oil tests were conducted on the same pair of bearings. A minor adjustment was made between the oil tests, involving 20 consecutive revolutions at 10 rpm to facilitate a uniform distribution of the lubricant. Conversely, for the grease tests, a fresh pair of bearings was employed for each distinct test parameter. Upon comparing the CoF-maps of IS1 and FVA3, a distinct observation emerges: in the case of pure oil (FVA3), there is an absence of any region where notably elevated friction values manifest, despite all tests being conducted on the same pair of bearings.

No Lubrication

In addition to the previously presented tests conducted under both grease and oil lubrication, this section introduces two tests performed entirely in the absence of any lubrication. The objective here is to underscore the pivotal role that lubricants play in influencing damage development. Similar to all other tests, the bearings underwent thorough cleaning through an ultrasonic bath of benzine and isopropanol. The test setup employs the operational parameters corresponding to two corner points of the CoF maps, as introduced in Section 6.1.1. Specifically, one test point is located at the lower left corner with $f = 0.2\,\text{Hz}$ and $\theta = 2°$, while the other is positioned at the upper right corner with $f = 5\,\text{Hz}$ and $\theta = 45°$. The maximum contact pressure is maintained at $p_{\max} = 2\,\text{GPa}$ for these tests.
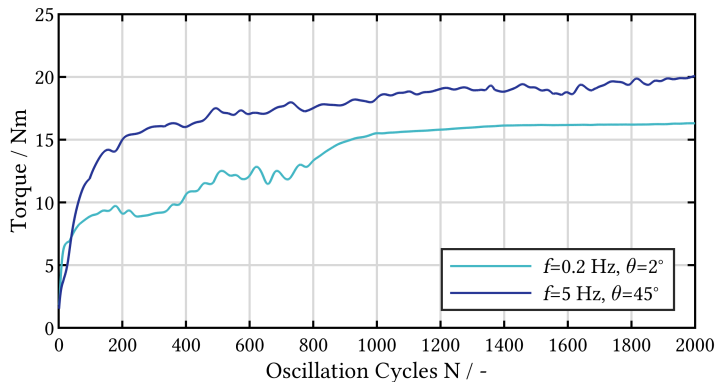
Figure 6.55.: Maximum torque curves without lubrication at a constant maximum pressure of $p_{max} = 2\,\text{GPa}$ and $f = 0.2\,\text{Hz}$ with $\theta = 2°$ (turquoise) and $f = 5\,\text{Hz}$ with $\theta = 45°$ (blue).

The torque profiles of both of these tests exhibit a rapid and pronounced ascent immediately at the beginning of the test. In contrast to the lubricated tests, there is an absence of an initial incubation period during which the torque remains relatively stable. Within less than 200 cycles, these tests reach torque values ranging from 10 to 15 Nm, approximately equivalent to the peak torque reached during damage-prone operating conditions under grease lubrication after approximately 4 000 cycles.

Hybrid bearings

Section 6.1.1 illustrates the developmental stages of false brinelling damage. It has been demonstrated that, particularly during the initial phase of damage, a high wear coefficient is observed, accompanied by a damage pattern characterized by a rough-appearing surface with brownish corrosion products. Considering that the wear behavior of the contact partners is presumed to be influenced by material properties, a test is conducted using rolling elements made of ZrO_2, which possess a Young's modulus nearly identical to that of the 100Cr6 rolling elements.
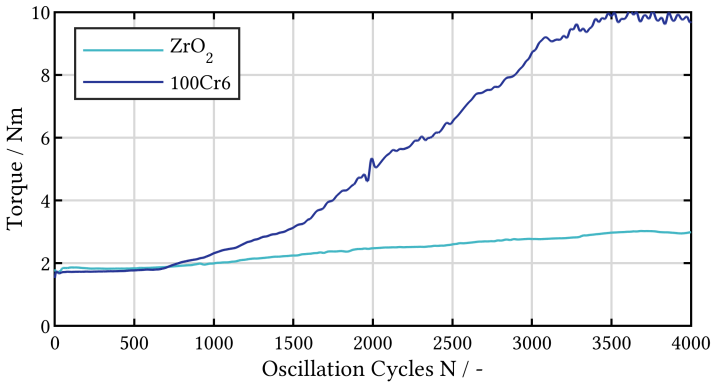
Figure 6.56.: Comparison of the maximum torque curves with 100Cr6 (blue) and ZrO_2 (turquoise) rolling elements at a constant maximum pressure of $p_{max} = 2\,\text{GPa}$, $f = 3\,\text{Hz}$, and $\theta = 15°$.

The torque curves for the tests are depicted in Figure 6.56. The dark blue curve represents the test with 100Cr6 rolling elements, while the turquoise curve corresponds to the test with ZrO_2 rolling elements. An increase in torque is evident in both cases. In both scenarios, the torque begins to rise at approximately cycle number 700. Notably, the rate of torque increase in the test employing 100Cr6 rolling elements is significantly higher, reaching a peak of 10 Nm. The maximum torque reached in the test employing ZrO_2 rolling elements is approximately 3 Nm. In this context, while ceramic rolling elements do not prevent damage initiation, they do substantially mitigate the extent of the damage.

Additives

The greases tested so far have been either unadditivated model greases or fully additivated industrial greases, the exact formulation of which remains undisclosed (see Section 5.4). To show the impact of a common additive package in a grease, a comparative examination is conducted between the unadditivated model grease MS_I1 and the same grease with an addition of 2 wt-% of both liquid and solid additives encompassing ZDDP (Zinc Dialkyl Dithiophosphate) and MoDTC (Molybdenum Dialkyl Dithiocarbamate). For this purpose, a parameter combination of $f = 1\,\text{Hz}$, $\theta = 15°$ and $p_{max} = 2\,\text{GPa}$, which is known to be damage-critical for the unadditivated grease, is selected.

The torque curves for these two tests are depicted in Figure 6.57. The dark blue curve represents the test using the unadditivated grease, while the turquoise curve portrays the test with the added additives.
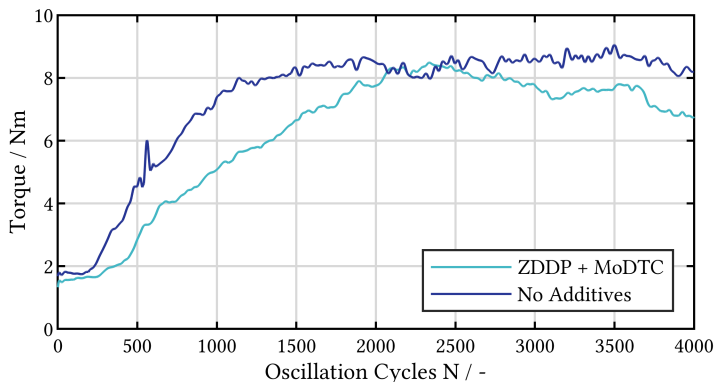
Figure 6.57.: Comparison of the maximum torque curves with the unadditivated grease MS_I1 (blue) and the same grease with added additives (ZDDP, MoDTC) (turquoise) at a constant maximum pressure of $p_{max} = 2\,\text{GPa}$, $f = 1\,\text{Hz}$, and $\theta = 15°$.

The chart reveals a striking resemblance between the two curves. Both exhibit a sharp ascent approximately after 250 cycles and attain a comparable peak torque value between 8 and 9 Nm. It could be noted that the ascent of the curve for the additivated grease starts slightly later and is characterized by a gentler incline. However, as substantiated by the repeat tests outlined in Section 6.1.1, such marginal deviations can manifest even when identical greases are examined under identical experimental conditions. Consequently, the introduction of the additive package does not seem to impart a significant reduction in wear within this context.

7. Analysis, Modelling & Discussion

The research carried out in this thesis highlights the potential for substantial damage to arise on the raceway of oscillating rolling element bearings when subjected to grease lubrication, even after a relatively small number of oscillation cycles. Section 6.1.1 provides a comprehensive examination of the development of false brinelling damage under critical test parameters. The observable manifestation of this damage, along with the torque profiles and the calculated energy wear coefficient, collectively points to the existence of multiple predominant damage mechanisms within the degradation process.

Initially, a consistently low torque profile reminiscent of the expected curves for an undamaged bearing [24] is observed, indicating the establishment of a protective lubricating film between the rolling element and raceway. However, after a small number cycles - which can vary from 10 to several thousand cycles - a steep increase in torque becomes evident. This initial phase, commonly referred to as the incubation phase, sees the displacement of the protective lubricant layer from the contact region, leading to direct metallic contact. Subsequently, damage initiation occurs on the raceway surface, appearing as reddish-brown and black oxide products, along with material chipping. These effects culminate in the formation of micropits.

In this early phase of damage, the energy wear coefficient reaches its peak, indicating a rapid progression of wear. The observed damage patterns and the high wear rate suggest that adhesion and tribo-corrosion are the dominant wear mechanisms during this stage. This observation gains further support from experiments outlined in Section 6.4, where ceramic rolling elements composed of zirconium dioxide (ZrO_2) are used in place of 100Cr6 rolling elements. The use of ceramic rolling elements results in a significantly lower torque increase, and the occurrence of material chipping on the raceway surface, which is seen with 100Cr6 rolling elements, is absent due to the lack of adhesion tendency of the contact partners.

However, the tests presented also underscore that certain test conditions play a crucial role in influencing the likelihood of early damage initiation. Two key parameters, oscillation amplitude and frequency, along with contact pressure and the properties of the lubricating grease, have a significant influence.

To address this, the concept of the starvation number S_N is introduced, as detailed in Equations 7.1 and 7.2. This dimensionless parameter serves to estimate whether the test conditions are conducive to early damage initiation on the raceway surface. A high starvation number indicates conditions that are more likely to lead to early wear initiation, while a low starvation number is preferable to minimize wear. The objective is to establish a critical starvation number that indicates safe operating conditions, regarding early wear initiation. In the following sections, this equation and its connection to the experimental work conducted within this thesis is comprehensively explained.

$$S_N = \begin{cases} S_{N,or} & \text{if } S_{N,ir} < S_{N,or} \\ \\ S_{N,ir} & \text{if } S_{N,ir} \geq S_{N,or} \end{cases} \tag{7.1}$$

Since the local operating conditions at the inner and outer ring contacts differ, they must be individually considered when evaluating the starvation number. For the entire bearing, the operating conditions are considered critical if either the conditions at the outer ring ($S_{N,or}$) or the inner ring ($S_{N,ir}$) are critical. Consequently, a distinction is made for the starvation number S_N, as specified in Equation 7.1.

These starvation numbers consist of the dimensionless terms $D_{1,ir/or}$ and $D_{2,ir/or}$. The term D_1 characterizes the base oil reflow into the contact, while D_2 aims to represent the cage's influence on contact relubrication. For a clearer comprehension of the starvation number's composition, the forthcoming explanations are centered on the inner ring contact's starvation number, detailed in Equations 7.2, 7.3, and 7.4. These principles are equally applicable to the outer ring contact.

$$S_{\mathrm{N,ir}} = \frac{\eta_0 \cdot f_{\mathrm{c}} \cdot a_{\mathrm{ir}}}{\sigma_{\mathrm{s}} \cdot O_{\mathrm{sr}}} \cdot \begin{cases} - & \text{if } x < 2b_{\mathrm{ir}} \\[2mm] \frac{x}{2b_{\mathrm{ir}}} & \text{if } 2b_{\mathrm{ir}} \leq x \leq x_{\mathrm{sw,ir}} \\[2mm] \frac{x_{\mathrm{sw,ir}}}{2b_{\mathrm{ir}}} \cdot \frac{x_{\mathrm{c,ir}}-x}{x_{\mathrm{c,ir}}-x_{\mathrm{sw,ir}}} & \text{if } x_{\mathrm{c,ir}} \geq x > x_{\mathrm{sw,ir}} \\[2mm] 0 & \text{if } x > x_{\mathrm{c,ir}} \end{cases} \tag{7.2}$$

$$D_{1,\mathrm{ir}} = \frac{\eta_0 \cdot a_{\mathrm{ir}} \cdot f_{\mathrm{c}}}{\sigma_{\mathrm{s}} \cdot O_{\mathrm{sr}}} \tag{7.3}$$

$$D_{2,\mathrm{ir}} = \begin{cases} - & \text{if } x < 2b_{\mathrm{ir}} \\[2mm] \frac{x}{2b_{\mathrm{ir}}} & \text{if } 2b_{\mathrm{ir}} \leq x \leq x_{\mathrm{sw,ir}} \\[2mm] \frac{x_{\mathrm{sw,ir}}}{2b_{\mathrm{ir}}} \cdot \frac{x_{\mathrm{c,ir}}-x}{x_{\mathrm{c,ir}}-x_{\mathrm{sw,ir}}} & \text{if } x_{\mathrm{c,ir}} \geq x > x_{\mathrm{sw,ir}} \\[2mm] 0 & \text{if } x > x_{\mathrm{c}} \end{cases} \tag{7.4}$$

Term D_1 (7.3) incorporates lubricating grease parameters, including the dynamic base oil viscosity η_0, the oil separation rate O_{sr}, and the surface tension between the oil and air phases σ_{s}.

Both the base oil viscosity η_0 and the surface tension between the liquid (base oil) and gas phase (air) are critical factors governing fluid spreading in narrow capillaries. When one assumes that inertial and pressure forces can be disregarded in the narrow gap between the rolling element and the raceway, two opposing forces come into play. On one hand, capillary forces arise from the interplay between the surface tension σ_{s} at the liquid-gas interface and the contact angle θ_{s} between the solid (raceway/rolling element) and the tangent at the interface between the liquid and gas phases. In cases where the base oil wets the surfaces optimally, such that $\cos(\theta_{\mathrm{s}}) = 1$, the contact angle can be effectively ignored. The capillary force is countered by the viscous frictional forces of the fluid. Assuming force equilibrium, WASHBURN formulated an equation describing the time-dependent spreading of a fluid in narrow capillaries [113].

$$z^2(t) = \frac{1}{2} \cdot \frac{r_{\text{ch}} \cdot \sigma_{\text{s}} \cdot \cos \theta_{\text{s}}}{\eta_0} \cdot t \tag{7.5}$$

In this equations, z represents the distance the fluid travels within the capillary, r_{ch} denotes a characteristic value for the capillary radius, and t denotes time. Jacod demonstrated that replenishment is driven by capillary forces and derived the following relationship for the change in lubricant film height $\mathrm{d}h$ at the inlet [53]:

$$\mathrm{d}h = \frac{\sigma_{\text{s}} \cdot a}{U \cdot \eta_0 \cdot \theta_{\text{res}}} \cdot \frac{\mathrm{d}V}{\mathrm{d}T} \tag{7.6}$$

a represents the width of the Hertzian contact area perpendicular to the motion direction. U is a dimensionless parameter denoting the rolling speed, while θ_{res} signifies the angle between the boundary of the lubricant reservoir and the direction of motion. The term $\frac{\mathrm{d}V}{\mathrm{d}T}$ is a dimensionless expression capturing the change in fluid volume within the contact inlet over time. It's worth noting that Jacod also assumes total wetting in his analysis.

The term D_1 within the starvation number S_{N} is built upon these considerations and assumptions. The base oil viscosity is placed in the numerator because higher base oil mobility, denoting lower viscosity, reduces the frictional resistance for base oil reflow. Conversely, O_{sr} is in the denominator, as an increased oil separation rate is expected to increase the base oil volume in the contact inlet. A higher surface tension σ_{s} leads to augmented capillary forces, facilitating base oil reflow near the contact region. Additionally, the parameter a, representing half of the Hertzian contact ellipse's major axis perpendicular to the rolling direction, signifies the distance the base oil must traverse from the lateral grease reservoirs to saturate the contact. A greater semi-axis length prolongs the replenishment time. The parameter f_{c} denotes the rollover frequency of a contact track area element, which is twice the oscillation frequency f. When considering the primary replenishment mechanism as the reflow of base oil from adjacent lateral grease reservoirs, the interval between two successive passages of a rolling element serves as a measure of the extent to which base oil can re-enter the contact region. A lower overrolling frequency implies more time for replenishment. This flow competes with the fluid outflow from the contact area and the track due to displacement through the rolling element.

The value of the oil separation rate O_{sr} depends on the test method, which in this study is the bleed test according to the IP121 standard [106]. To obtain a parameter that provides information about the bleeding behavior of a grease and is independent of the test method, Darcy's law can be considered [2]:

$$\vec{u}_f = -\frac{k_p}{\eta_0} \cdot \vec{\nabla} p \qquad (7.7)$$

Here, $\vec{u}_f$ describes the local flow velocity, k represents permeability, and $\vec{\nabla} p$ denotes the pressure gradient. From the IP121 bleed tests [106], the permeability of the fresh grease can be calculated after rearranging the equation:

$$k_p = -\frac{\vec{u}_f \cdot \eta_0}{\vec{\nabla} p} \qquad (7.8)$$

Since the oil separation rate O_{sr} was determined in the same manner for all greases, for this work it is approximately true that $O_{sr} \sim \frac{k}{\eta_0}$, see Figure 7.1.

Minor deviations are attributed to the different densities of the base oils. Thus, the term D_1 can also be expressed as follows:

$$D_{1,ir} = \frac{\eta_0^2 \cdot a_{ir} \cdot f_c}{\sigma_s \cdot k_p} \qquad (7.9)$$

In this study, further analyses will be conducted using the oil separation rate O_{sr}. However, it is recommended that this option be taken into consideration for future research.

The term D_2 encompasses the cage geometry's influence on contact replenishment. This term is divided into four subranges. The first range, where amplitude ratios are $\frac{x}{2b} < 1$, isn't further explored in this study due to other relevant wear phenomena arising from the specific contact kinematics (see Section 3.2). In the second range, with $2b \leq x \leq x_{sw}$, it's assumed the cage has minimal impact on lubrication conditions in the contact. Here, the starvation number increases with growing amplitude ratio $\frac{x}{2b}$. The reason is that the displaced lubricant volume, counteracting the returning lubricant volume due to capillary forces, increases with greater distance traveled x and an elongated contact track. This holds until the angle θ_{sw} or the distance x_{sw} is reached,
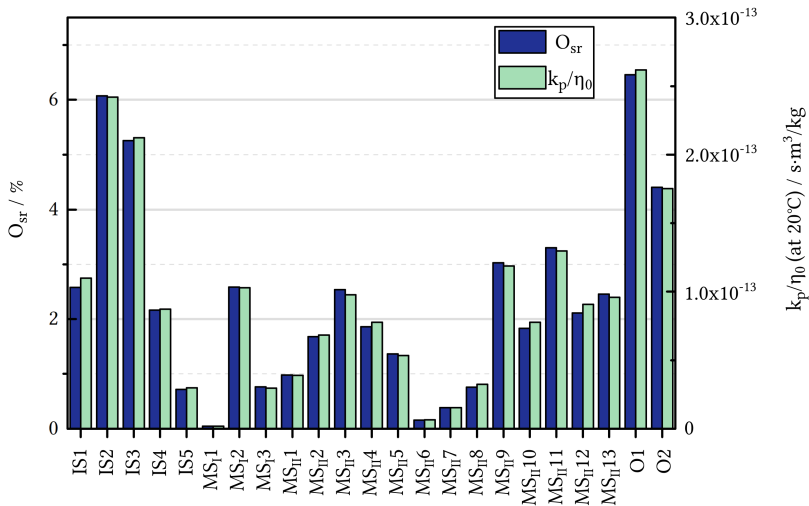
Figure 7.1.: Comparison of the oil separation rates O_{sr} and the permeability values k_p between the different greases at 20°C.

referred to as the starvation-driven wear angle/distance. Beyond this, the contact track interacts with the cage or grease reservoirs trapped on the cage. From this point, it's assumed that the starved contact track length diminishes linearly with increasing distance x. This linear decrease is modeled by the term $\frac{x_c - x}{x_c - x_{sw}}$, up to a limit x_c. The fourth region commences from distance x_c, where the contact track on the rolling element is fully submerged within the cage, thereby preventing early wear initiation.

In Figure 7.2, the different regions and their boundaries are depicted. Each case presents the rolling element track projected onto the drawing plane at various distances x. The contact ellipse at the oscillation's starting point is displayed in the middle of the track with a solid line, while the dashed line indicates the contact ellipse at the reversal points. The cage is shown on both sides of the track. In the top row, the case where $x < 2b$ is depicted in grey, which is not under consideration. The second row illustrates the boundary scenario for $\frac{x}{2b} = 1$. The dark blue area represents the portion of the track that undergoes rolling contact without any interaction with the cage. The yellow
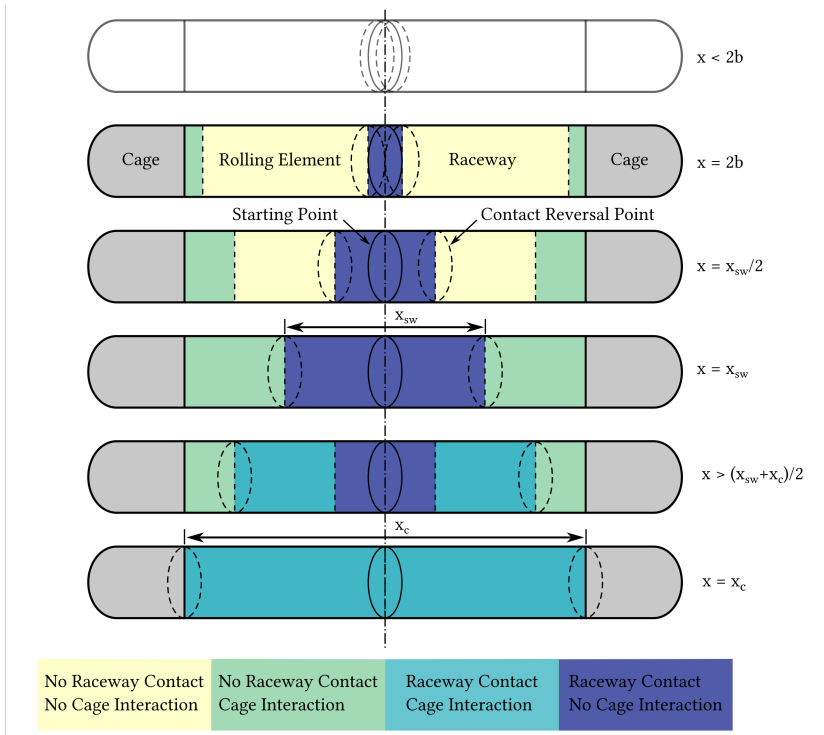
Figure 7.2.: Illustration depicting the interaction between the rolling element track and cage under varying oscillation distances x.

section shows the part of the rolling element that doesn't engage with either the rolling element or the cage. The light green region marks the surface on the rolling element that encounters the cage without experiencing rolling contact. As distance x increases, the dark blue area grows linearly. Line 4 displays the boundary situation for $x = x_{sw}$. In this case, the largest dark blue surface, which experiences rolling contact but no cage interaction, is present. As the angle increases further, sections of the rolling element's track immerse into the cage. Lines 5 and 6 represent this effect with a turquoise area. As a result, the dark blue area within the interval $x_c \geq x > x_{sw}$ decreases linearly

until the limit in line 6 is surpassed. This implies that for $x > x_c$, the entire rolling element track interacts with the cage.

Moving on to Figure 7.3, the left side depicts the Coefficient of Friction (CoF) map of the experiments with Grease IS1. On the right side, the corresponding calculated starvation number $S_{N,0.6}$ is presented. Notably, for this representation, the starvation number was computed assuming a 40 percent reduction in distances x_{sw} and x_c. The reason behind this adjustment will become evident during the ensuing discussion. The map on the right utilizes color coding similar to the CoF map to visually convey the behavior of the starvation number using an example as a reference.
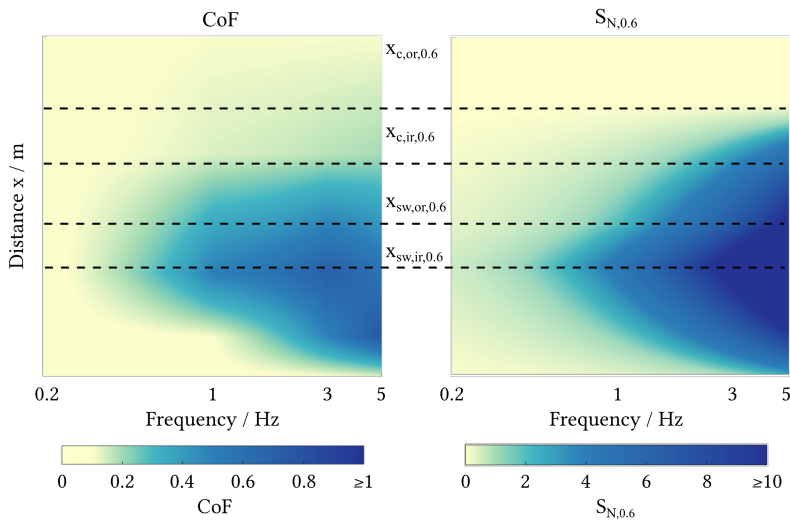
Figure 7.3.: Illustration providing a qualitative comparison of the maximum coefficient of friction (CoF) (left) and calculated Starvation Number $S_{N,0.6}$ (right) for grease IS1.

The hypotheses underpinning the starvation number S_N are explored below, drawing from the experiments conducted within this study. Beginning by examining the term D_1, which characterizes the base oil reflow, and subsequently investigating the term D_2 which characterizes the impact of the cage.

Base Oil Reflow

To establish the critical role of near-contact base oil reflow as a replenishment factor, dedicated tests were conducted on the rolling bearing test rig (Section 6.2.1) and the EHL tribometer (Section 6.2.2). The tests conducted at the component level demonstrate that wear under critical operating conditions can be mitigated or even prevented by implementing regular pauses between oscillation cycles, during which the bearing remains stationary. Even brief pauses of around 5 seconds after every 100 oscillation cycles result in a notable reduction in maximum torque, primarily attributed to base oil reflow. As the ratio of uninterrupted cycles N_u to pause time t_p decreases, the damage to the bearing raceway diminishes.

This behavior of base oil reflow was also visually confirmed on the EHL tribometer. A defined number of oscillation cycles were intermittently interrupted by pauses. The lubricant's behavior around the contact area was observed and quantified before, during, and after these pauses. Quantification was based on the lubricant-wetted areas in the contact's inlet and outlet. Reflow, presumed to be base oil, occurred mainly in the near-contact area during the pauses. No base oil reflow was observed in the track far from the contact. It was demonstrated that the lubricant reservoirs in the contact inlet expand due to these pauses. Experiments using greases from model series II (MS_{II}) illustrated a notable correlation between the size of base oil reservoirs in the contact inlet and the term D_1 adjusted by constant factors a and f_c (as outlined in Section 6.2.2):

$$D_{1,\text{red}} = \frac{\eta_0}{\sigma_s \cdot O_{sr}} \tag{7.10}$$

An attempt was made to establish a correlation between the change in size of the oil reservoirs in the contact inlet before and after pauses and the measured lubricant film height within the contact. However, attempts to correlate the mean value of the average change in central lubricant film height Δh_c with the wetted area in the inlet did not yield conclusive results due to the significant standard deviations in the measured lubricant film heights. These deviations arise from the composite nature of the lubricant film height, which includes both the thickener layer and the base oil film. Particularly at the low entrainment speeds investigated, the base oil film formed is on the order of a few nanometers, possibly smaller than the thickener layer in most cases [15].

Furthermore, deviations arise from manual point selection for film height measurements.

Nevertheless, the obtained results do support the reasonable assertion that base oil reflow plays a pivotal role as a replenishment mechanism in oscillating rolling bearings under grease lubrication. The influence of base oil viscosity and oil separation rate is appropriately encapsulated within the term D_1, aligning with the outcomes of the conducted investigations. However, the influence of surface tension σ_s could not be definitively confirmed based on the performed studies, primarily because the surface tensions of the investigated base oils show minimal variations. At this stage, it is presumed, drawing on the research by Washburn and Jacod, that the parameter σ_s does affect reflow behavior [113, 53]. Nonetheless, due to the lack of comprehensive experimental investigations on this parameter, it is primarily employed to non-dimensionalize the term D_1. Apart from that, the majority of oils exhibit only marginal variations in surface tension [103].

Cage Influence

The parameter study conducted in Section 6.1 revealed an interesting observation: the experimental conditions exhibited reduced sensitivity to early wear initiation above a certain oscillation angle θ_{sw}. This observation contradicts the notion that the track size increases linearly with the distance x, resulting in a higher volume of displaced lubricant per cycle. Hence, it becomes plausible that an alternative replenishment mechanism comes into play beyond a certain angle. It is reasonable to hypothesize that this replenishment mechanism could be related to either the overlapping of adjacent contact areas or the interaction between the rolling element and the cage.

Before delving further, a question emerges: Is replenishment akin to the experiments in Section 6.2, involving the delivery of base oil, or does it entail the transfer of bulk grease into the contact?

To address this, tests were undertaken where oscillations at critical parameter combinations were periodically interrupted by single "lubrication cycles" featuring larger oscillation angles. Remarkably, lubrication cycles with oscillation angles exceeding 50° resulted in negligible damage to the bearing raceway over a test span of more than 20 000 cycles, effectively preventing wear. These lubrication cycles were introduced after every 100 base cycles and were performed at the same frequency as the base cycle of 3 Hz.

The fact that the lubrication cycles were conducted at the same frequency negates the possibility that their effectiveness arose solely from an increased time for replenishment of base oil, similar to observations in Section 6.2.1. Instead, it seems reasonable to infer that beyond a certain angle, grease is reintroduced into the contact, thus resetting the incubation phase and allowing the buildup of a protective lubricating film during subsequent base cycles.

In order to distinguish between whether this relubrication effect originates from the overlapping of neighboring contact areas (occurring around $\theta_{\text{overlap,ir}} = 45°$ on the inner ring and $\theta_{\text{overlap,or}} = 60°$ on the outer ring) or from the cage interaction (where the rolling element track fully immerses around $\theta_{\text{c,ir}} = 45°$ on the inner ring and $\theta_{\text{c,or}} = 60°$ on the outer ring), tests were performed with half the number of rolling elements and without a cage. These experiments showed that the positive effect of the immersion within the cage dominates (see Section 6.3.1).

To validate the hypothesis that immersion of the rolling element track within the cage is a key relubrication mechanism, modified cage designs were tested to reduce the necessary angle for full track immersion from $\theta_{\text{c,ir}} \approx 45°$ on the inner ring and $\theta_{\text{c,or}} \approx 60°$ on the outer ring, to $\theta_{\text{c,ir}} \approx 21°$ on the inner ring and $\theta_{\text{c,or}} \approx 25°$ on the outer ring. The first modification of the cage (KV1), a plastic snap cage, was able to significantly reduce the effective lubrication cycle angle, making $\theta_{\text{l}} = 30°$ remarkably effective. These tests indicated that even with substantially smaller lubrication cycle angles, notable improvements were achieved compared to the original cage design.

However, drawing definite conclusions about the relubrication mechanism from these tests is challenging, as the cage design not only reduced the immersion angle but also resulted in significantly better sealing against the environment compared to the original manufacturer's (OEM) cage. The KV2 and KV3 cage variants increasingly fill the bearing's free volume. KV3 is equipped with additional shields functioning as gap seals. This enhanced sealing effect could further delay the onset of severe damage. With a constant oscillation angle of $\theta = 30°$ and a constant oscillation frequency of $f = 3\,\text{Hz}$, the time until a torque limit of $3\,\text{Nm}$ was exceeded increased by over threefold.

The additional sealing effect seems to be important, and to ascertain whether it alone is responsible for the improved performance, tests were conducted with the original cage supplemented with shields. These bearings were filled

with 10 ml of grease, corresponding to 100% filling according to [62]. While wear initiation began at the same time as in an unsealed bearing, the torque curve flattened considerably after an initial steep increase and in one case remained constant over an extended period. Examination of the damage marks revealed that in the case of the original cage with shielding, the grease initially sagged into the lower region of the bearing due to gravity, fully encasing the lower rolling elements in grease. However, over time, the upper contacts were cleared of grease, similar to the unsealed bearing. This suggests that immersion in lateral grease reservoirs is a highly effective mechanism to prevent wear in oscillating bearings.

An optimally designed cage keeps the grease reservoirs close to the contact area between the rolling element and the raceway for an extended duration. Interestingly, this does not necessitate a large free volume within the bearing; on the contrary, a large free space might prevent grease from being held close to all contacts. A design such as the KV3 variant, which creates relatively narrow gaps between the raceway and rolling element near the contact area while preventing grease escape, appears to be optimal for this application.

In addition, experiments were performed on an EHL tribometer using a simulated rolling bearing cage. These experiments also indicated that the cage positively influences lubricant film height, especially at angles and positions in the oscillation cycle that interact with the cage. The change in lubricant film height exceeded what would be expected for pure base oil, providing further support for the hypothesis that both base oil and bulk grease are transported back into the contact by the cage.

These experimental findings form the basis for the term D_2 in the starvation number. As mentioned earlier, this term is divided into four regions, with the boundary of the first region calculable from the provided load and geometry. The second, third, and fourth regions are dependent on distances x_{sw} and x_c. Beyond the distance x_c, as determined by experimental investigations on the cage's influence, operating conditions are no longer critical for early wear initiation on the bearing raceway, and $S_N = 0$ applies. At the distance x_{sw}, operating conditions within S_N are most critical. From the conducted tests and theoretical considerations, the assumption $x_{sw} = \frac{x_c}{2}$ seems reasonable.

With the explanation of the terms D_1 and D_2 in greater detail, all component tests conducted under constant oscillation angle and frequency can now be classified based on their starvation numbers. Figure 7.4 depicts the starvation number $S_N + 10^{-3}$ against the dimensionless parameter D_1 on the x-axis and

the dimensionless parameter D_2 on the y-axis. The term 10^{-3} is added to enable logarithmic representation without zero values. Tests are color-coded based on their maximum coefficient of friction (CoF) values. To distinguish between damaged and undamaged bearings, a friction coefficient limit of $CoF_{\text{lim}} = 0.2$ is set. Tests with a friction coefficient $CoF \geq 0.2$ are denoted by dark blue triangles, while tests with a friction coefficient $CoF < 0.2$ are indicated by light yellow triangles. The friction coefficient values are computed using the method outlined in Section 3.2.4. With this approach, it becomes theoretically feasible to categorize bearing tests with varying geometries and under different loads according to their respective starvation numbers.

The upper diagram in Figure 7.4 displays results for S_N and distances $x_{c,\text{ir}}$ and $x_{c,\text{or}}$ calculated from the cage geometry. The lower diagram presents classification for $S_{N,0.6}$ under the assumption of a 40% smaller critical distance on the inner and outer rings, $x_{c,\text{ir},0.6}$ and $x_{c,\text{or},0.6}$, respectively.

Figure 7.5 offers a side view of the diagrams, illustrating the starvation number S_N+10^{-3} or $S_{N,0.6}+10^{-3}$ against the term D_1, characteristic of base oil reflow. A boundary around $S_N \approx 1$ is evident in both diagrams, beyond which damaged bearings become increasingly prevalent. In the lower diagram for $S_{N,0.6}$, a more distinct boundary between damaged and undamaged tests is observed. The primary discrepancy arises from the chosen value of the critical distance x_c, which is smaller in the lower diagram. Consequently, all tests with an oscillation angle of $\theta \geq 45°$ yield $S_N = 0$ in the lower diagram, whereas only tests with $\theta \geq 60°$ result in $S_{N,c} = 0$ in the upper diagram.

Figure 7.6 offers another side view, depicting the starvation number $S_N + 10^{-3}$ or $S_{N,0.6} + 10^{-3}$ against the term D_2 or $D_{2,0.6}$, indicative of cage influence. Notably, some tests with high starvation numbers (S_N) and $D_2 \approx 8$ exhibit no damage, yet these tests have an elevated risk based on $S_{N,0.6}$. The starvation number $S_{N,0.6}$, assuming a reduced critical angle, appears better suited to predict whether tests should be categorized as damaged or undamaged.

Figure 7.4.: Illustration of all tests conducted at a constant oscillation angle and frequency with a cycle number of 4 000, plotted in the space defined by S_N or $S_{N,0.6}$ and D1, as well as D2 or $D2_{0.6}$. The individual tests are represented by colored triangles. Tests marked in light yellow have reached a maximum torque resulting in a $CoF < 0.2$, while trials with a $CoF \geq 0.2$ are depicted in dark blue.

Figure 7.5.: Illustration of all tests conducted at a constant oscillation angle and frequency with a cycle number of 4 000, plotted in a diagram defined by S_N or $S_\text{N,0.6}$ and D1. The individual tests are indicated by colored triangles. Tests highlighted in light yellow have reached a maximum torque resulting in a $CoF < 0.2$, while tests with a $CoF \geq 0.2$ are represented in dark blue.
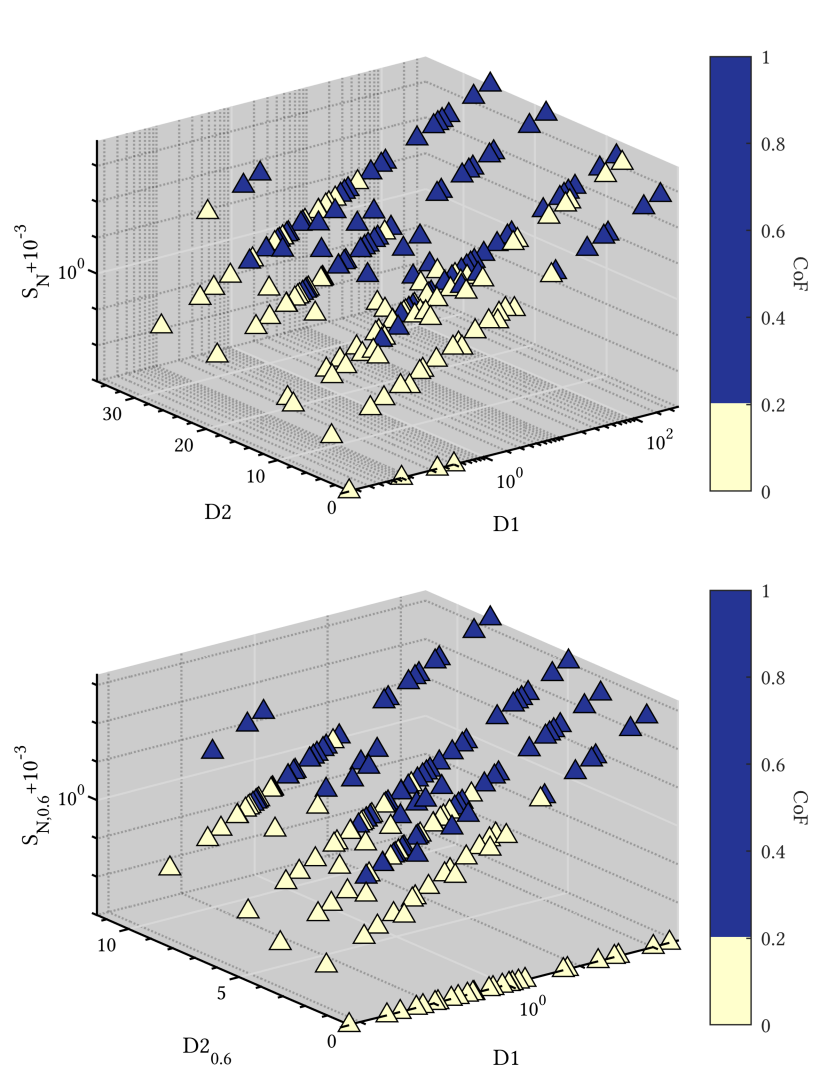
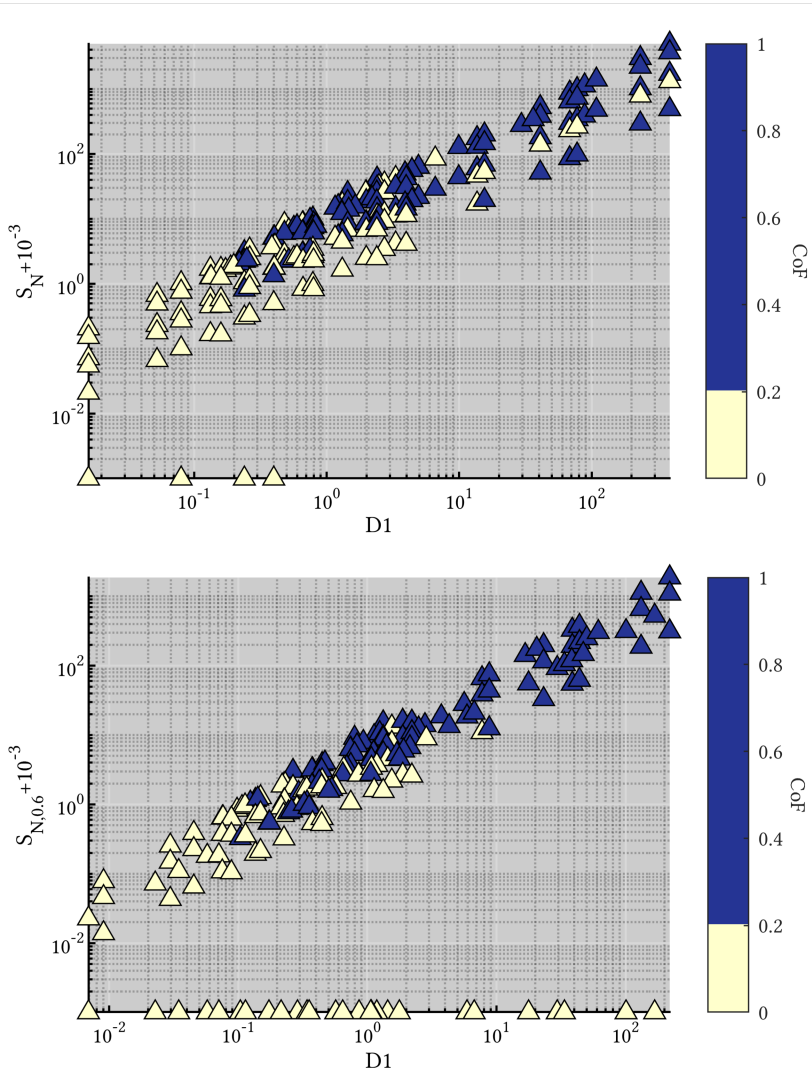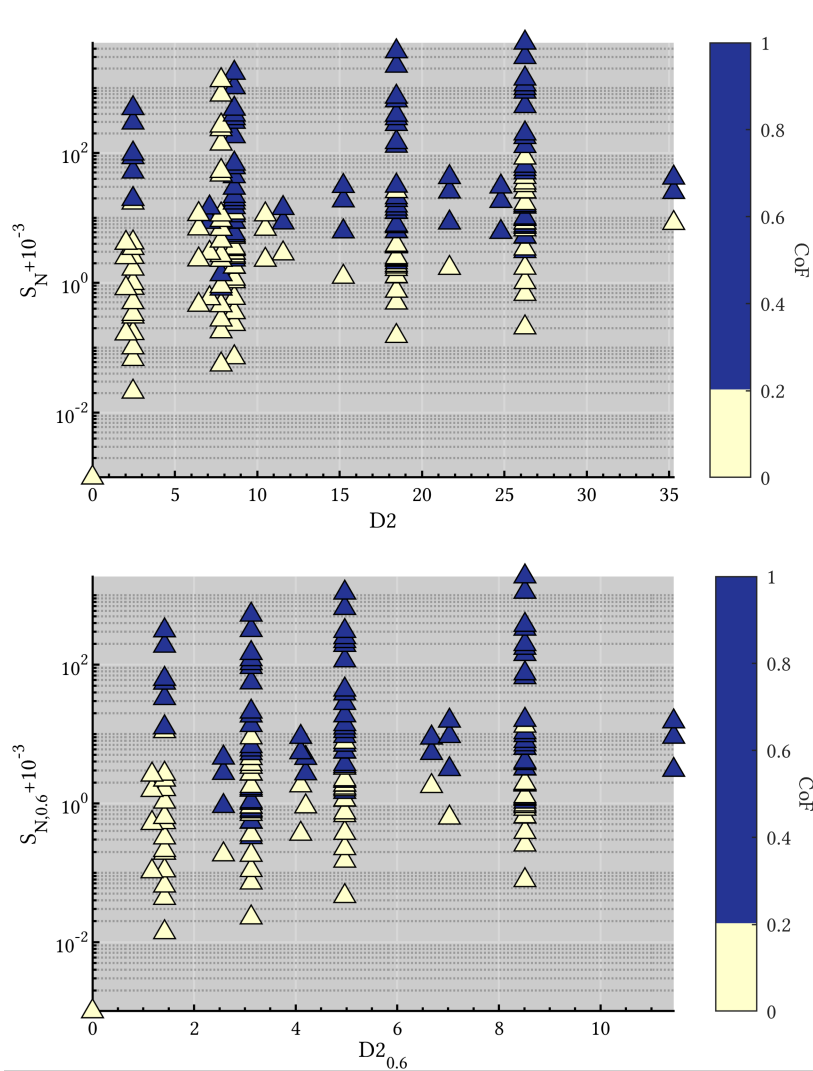**Figure 7.6.:** Illustration of all tests conducted at a constant oscillation angle and frequency with a cycle number of 4 000, depicted in a diagram defined by S_N or $S_{N,0.6}$ and D2 or $D2_{0.6}$. The individual tests are represented by colored triangles. Tests labeled in light yellow have reached a maximum torque leading to a $CoF < 0.2$, while trials resulting in a $CoF \geq 0.2$ are displayed in dark blue.

To verify this hypothesis, a binary logistic regression is conducted, utilizing the starvation numbers S_N and $S_{N,0.6}$ as predictors [58]. The experiments are categorized into two classes: 'undamaged (1)' and 'damaged (0)', based on the maximum CoF observed during the experimental period. Specifically, if $CoF \leq 0.2$, the test is classified as undamaged (1), and if $CoF > 0.2$, the test is classified as damaged (0). The regression outcomes are depicted in the plots in Figure 7.7. The upper plot showcases the logit regression function and the individual test results for S_N, while the lower plot does the same for $S_{N,0.6}$. The left ordinate axis represents the binary classifiers 0 and 1, whereas the right ordinate axis indicates the probability of occurrence. The abscissa displays the starvation number as the predictor. A horizontal line is inserted at the chosen separation value, i.e., a probability of 0.5. The point at which this line intersects the regression curve is marked by a vertical line, illustrating the starvation number at the separation value $S_{N,sep}$. The corresponding confusion matrices can be found in Table 7.2 and Table 7.1. These matrices include significant metrics calculated from them, such as the χ^2 and associated p values, which indicate a significant relationship between the selected starvation numbers and the 'damaged'/'undamaged' classification [83]. When comparing the characteristics of the regression models, it becomes evident that $S_{N,0.6}$ performs significantly better for classifying the results. For this model, the optimal separation of the 'damaged (0)' and 'undamaged (1)' classes occurs at a separation value of $S_{N,sep} = 3.684$. Figure 7.8 presents the χ^2 values as a function of the selected critical angle θ_c. The relative critical angle is plotted on the x-axis, and it's clear that the maximum χ^2 values occur around 0.6 times the critical angle.

In Figure 7.9, a comparison between the model and experimental results for grease IS1 is displayed. The map on the left depicts the linearly interpolated maximum CoF values, with a binary color separation at a friction value of $CoF_{lim} = 0.2$. Values with $CoF \geq 0.2$ are shown in blue. On the right, the starvation number $S_{N,0.6}$ is shown, with color separation at the value $S_{N,0.6,sep} = 3.864$ determined from the logistic regression. Experiments conducted at the points marked with triangles are classified based on whether they exceed the limit values CoF_{lim} or $S_{N,0.6,sep}$ (blue) or not (yellow). The agreement between the classification of experiments and the model for grease IS1 is evident in all points, with a single exception. The experiment at $f = 5$ Hz and $\theta = 30°$ falls just short of the limit CoF_{lim} in the experiments ($CoF = 0.19$), classifying it as non-critical, while the starvation number with $S_{N,0.6} = 4.48$ slightly exceeds the limit $S_{N,0.6,sep}$, categorizing it as critical.

Figure 7.7.: Comparison of regression curves for the logistic regression model with the predictor S_N (top) and the predictor $S_{N,0.6}$ (bottom).

		Prediction	
		Damaged (0)	Undamaged (1)
Outcome	Damaged	28	73
	Undamaged	5	108
Correct Predictions	0.636	F1-Score	0.735
Precision	0.597	χ^2	22.403
Specificity	0.277	p	$2.211 \cdot 10^{-6}$
Sensitivity	0.956	$S_{\text{N,sep}}$	110.652

Table 7.1.: Confusion matrix for the logistic regression model applied to the starvation number S_{N}.
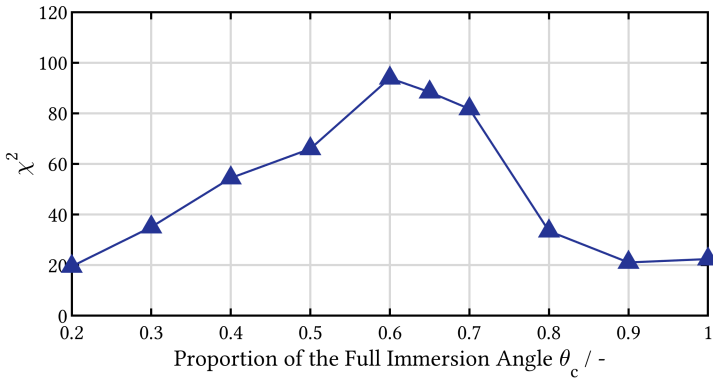
Figure 7.8.: Variation of χ^2 values as a function of the calculated critical angle proportion θ_{c}.

		Prediction	
		Damaged (0)	Undamaged (1)
Outcome	Damaged	69	32
	Undamaged	6	107
Correct Predictions	0.822	F1-Score	0.849
Precision	0.77	χ^2	93.876
Specificity	0.683	p	0
Sensitivity	0.947	$S_{N,0.6,sep}$	3.684

Table 7.2.: Confusion matrix for the logistic regression model applied to the starvation number $S_{N,0.6}$.
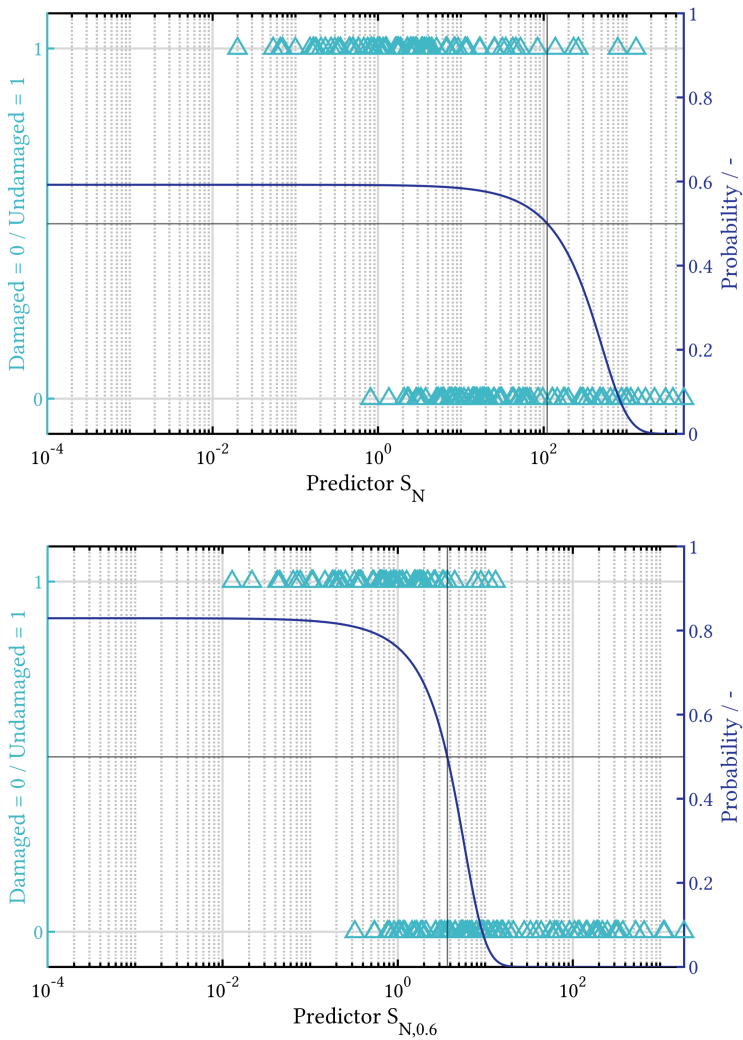

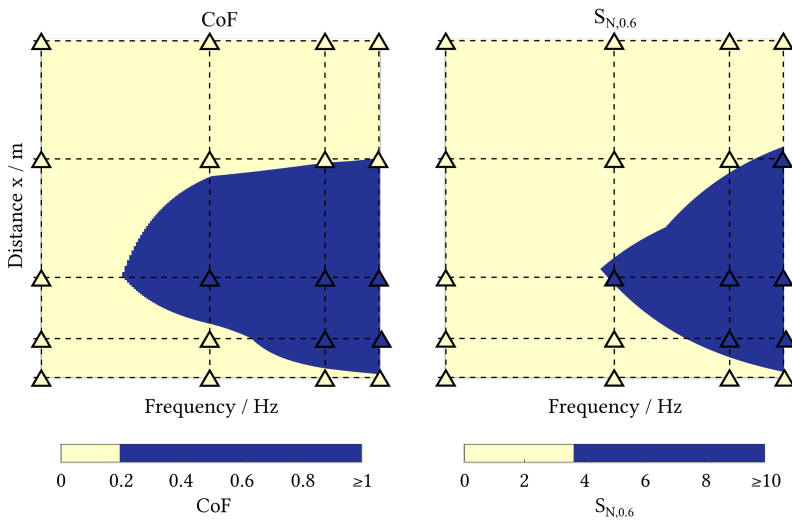**Figure 7.9.:** Comparison of regression curves for the logistic regression model using the predictor S_N (top) and the predictor $S_{N,0.6}$ (bottom).

However, if we assume the hypothesis that false brinelling damage is initiated only when the rolling element track does not fully enter the cage, a

comprehensive assessment for the entire bearing would logically consider the largest distance x_c as the critical one. This raises the question of why the model performs better when assuming a smaller critical distance $x_{c,0.6}$.

The discrepancy could be attributed to two factors. One factor, which hasn't been adequately considered thus far and therefore isn't yet factored into the starvation number, is the influence of the number of oscillation cycles. A definitive classification of tests into the 'undamaged (0)' and 'damaged (1)' classes can only be achieved if the test duration is sufficiently long to ensure that the specific type of damage being studied won't occur during the bearing's service life. However, to accommodate a wide range of tests with varying oscillation and grease parameters, the tests included in this classification were limited to a duration of 4 000 cycles.

Extended tests conducted at specific parameter combinations with a 10-fold increase in test duration have revealed that wear initiation can also occur at higher cycle counts. Figure 7.10 displays torque curves from the extended tests conducted at different frequencies and oscillation angles: $f = 3\,\mathrm{Hz}$ and $\theta = 2°$, $f = 0.2\,\mathrm{Hz}$ and $\theta = 15°$, $f = 3\,\mathrm{Hz}$ and $\theta = 30°$, $f = 3\,\mathrm{Hz}$ and $\theta = 45°$, and $f = 3\,\mathrm{Hz}$ and $\theta = 60°$. These curves fall within the non-damage-critical regions on the CoF map for grease IS1 at 4 000 cycles, as shown in the upper map in Figure 7.10.

Upon examining the curves of the extended tests, a few observations become apparent:

- Tests at $f = 3\,\mathrm{Hz}$ and $\theta = 2°$ (a)) and at $f = 0.2\,\mathrm{Hz}$ and $\theta = 15°$ (b)) exhibit no torque increase during the 40 000-cycle test duration and can be classified as undamaged.

- The test at $f = 3\,\mathrm{Hz}$ and $\theta = 60°$ shows no torque increase. In this case, the oscillation angle equals the angle θ_c calculated from the cage geometry.

- A slight increase in torque is detected after 30 000 cycles in the test at $f = 3\,\mathrm{Hz}$ and $\theta = 45°$.

- However, a significant increase in torque occurs around 8 000 cycles for the test at $f = 3\,Hz$ and $\theta = 30°$.

This suggests that, within the range of higher frequencies and oscillation angles between $30°$ and $\theta < 60°$, an extended test duration should be considered. Consequently, it's reasonable to contemplate a larger critical distance x_c for

the starvation model, even if this might not be the optimal representation for tests conducted at a fixed cycle number of 4 000 cycles.

The reason the model for the critical angle of $\theta_c = 60°$ doesn't correlate as well with the results is because angles between $\theta = 30°$ and $\theta < 60°$ are evaluated as damage-critical by the starvation number, even though they aren't during the short test period. If the overall test duration were substantially increased, it's plausible that the starvation model with a critical angle of $\theta_c = 60°$ would yield better results.
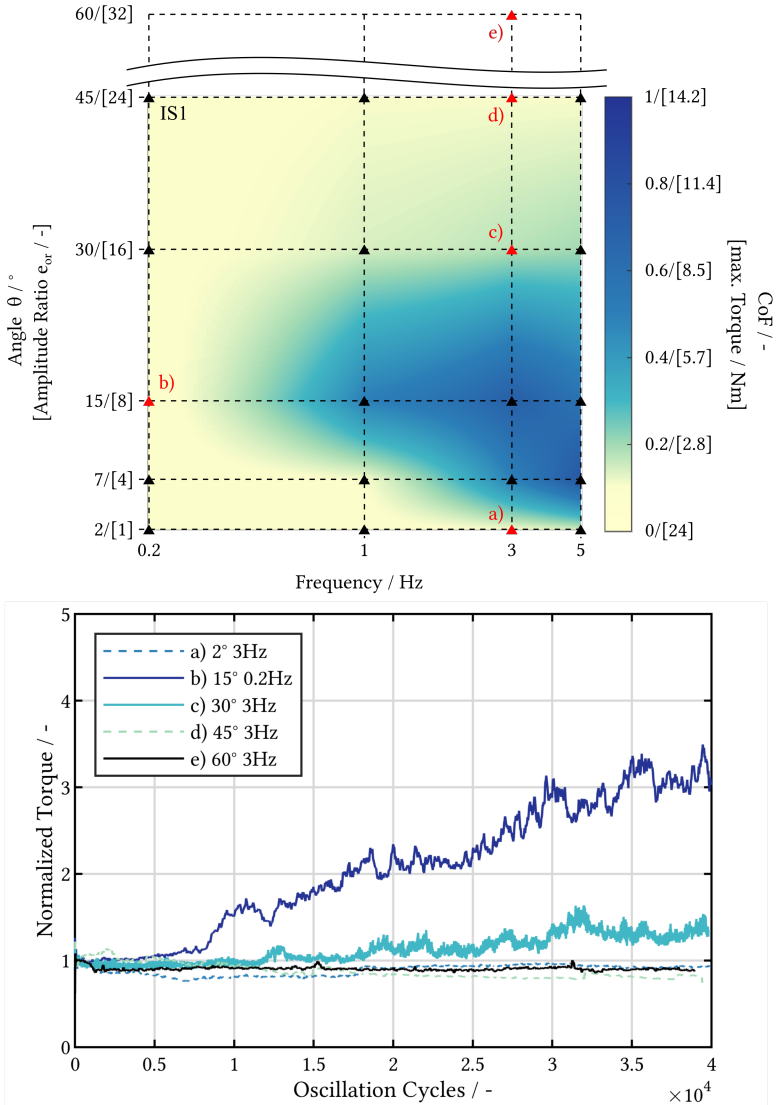
Figure 7.10.: Extended tests for 40 000 oscillation cycles that appear to be uncritical for 4 000 cycles. a) $f = 3\,\text{Hz}$, $\theta = 2°$; b) $f = 0.2\,\text{Hz}$, $\theta = 15°$; c) $f = 3\,\text{Hz}$, $\theta = 30°$; d) $f = 3\,\text{Hz}$, $\theta = 45°$; e) $f = 3\,\text{Hz}$, $\theta = 60°$.

Another hypothesis to explain why a critical angle $\theta_c \leq 60°$ could lead to a relubrication effect, or at least a delay in damage initiation, involves the presence of grease reservoirs settling on the cage. These reservoirs could potentially reduce the required oscillation angle for track relubrication. This idea is illustrated in Figure 7.11. During the course of the test, these reservoirs might change based on the properties of the lubricant. For instance, they could decrease as the number of cycles increases, potentially delaying damage initiation. Based on the current tests, it appears plausible that the grease reservoirs degrade over time in unsealed bearings, causing the critical angle θ_c to increase with extended test duration.

In addition to relubrication by grease reservoirs on the cage, there's the possibility that contact between the cage and rolling element could also lead to relubrication of the track. If grease buildup on the sides of the rolling element contact track comes into direct contact with the cage, it could be redistributed and pushed back into the rolling contact area. This same effect might also occur between the raceway track and the cage. With the geometry of the OEM cage, the distances between the track and the cage are relatively large, potentially minimizing the significance of this effect. However, in the case of the cage variants KV1-KV3 presented in Section 6.43, which substantially reduce this distance, this effect could play a more significant role.

In certain tests, an interesting observation was made where grease migrated to the bottom of the bearing over an extended test period due to the force of gravity. As a result, the grease reservoirs for the rolling elements on the lower side of the bearing grew larger, while the reservoirs for the rolling elements on the upper side became smaller. This phenomenon was particularly evident in experiments involving shielded bearings, as detailed in Section 6.3.2. The tests conducted with the OEM cage and additional shields revealed that the grease accumulated on the bottom side of the bearing, leading to undamaged contact areas at the bottom even after a high number of oscillation cycles. However, the upper contact areas experienced damage within a shorter test duration, making the initial torque curves nearly indistinguishable from those of the unshielded bearings. For the shielded bearings, the torque curves showed an increase up to a lower torque level, after which they remained relatively constant. This behavior can be attributed to fewer contact areas being damaged that are located exclusively in upper segment of the bearing . The absence of damage in the lower areas of the sealed bearing indicates that a rolling element completely surrounded by grease benefits from the
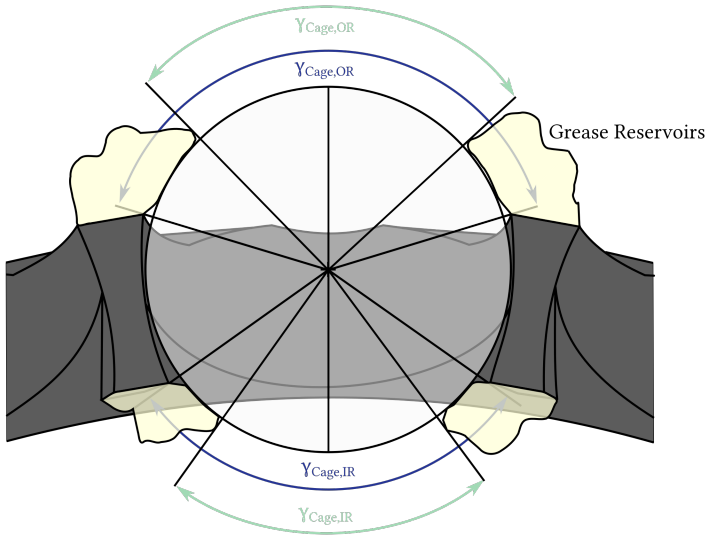
Figure 7.11.: Alteration of the critical oscillation angle θ_c resulting from the presence of grease reservoirs on the cage.

relubrication provided by the surrounding grease reservoirs, thus preventing damage.

Based on these observations, it can be inferred that if the bearings were filled with grease to 100% capacity and sealed to the extent that no grease leakage could occur, they would likely be well-protected against false brinelling damage. However, it's important to note that in the tests presented in Section 6.3.2 (Figure 6.47), there was some partial leakage of grease from the seal during both the mounting process and the test run. This implies that the filling level of grease during the tests was likely not at 100%. Notably, in one of the tests, the leakage was more significant, leading to higher torque curve values compared to the other curve.

Temperature Influence

Temperature plays a crucial role in the context of the starvation number, particularly in relation to the lubricant parameters within the dimensionless term D_1.

$$D_1(\vartheta) = \frac{\eta_0(\vartheta) \cdot a_{\text{ir}} \cdot f_{\text{c}}}{\sigma_{\text{s}}(\vartheta) \cdot O_{\text{sr}}(\vartheta)} \tag{7.11}$$

This term is known to be temperature-dependent. While the specific influence of temperature on surface tension (σ_{s}) was not explored extensively within the scope of this study, available literature values indicate that the change in surface tension is relatively minor within a realistic temperature range for practical applications [103]. MARQUES, for instance, suggests that the relative change in surface tension for various PAO oils, given a temperature difference of $\Delta\vartheta = 20\,\text{K}$, falls within the range of approximately 5% ($\frac{\sigma_{\text{s}}(20°C)}{\sigma_{\text{s}}(40°C)} \approx 1.05$). However, it is worth noting that the impact on the contact angle is substantially more significant [103].

When it comes to viscosity and oil separation rate, the effects of temperature are much more pronounced. The values of η_0 and O_{sr} for the greases at 20°C and 40°C are detailed in Section 5.4. In both cases, a two to three-fold change is realistic with the same temperature difference.

Figure 7.12 depicts the relative change of the terms D_1 resulting from a shift in temperature from 40°C to 20°C, as indicated by the ratio $\frac{D_1(20°C)}{D_1(40°C)}$. As temperature decreases, two key effects emerge: an increase in viscosity and a decrease in oil separation rate. These changes lead to an overall increase in the value of the term D_1 and subsequently amplify the value of the starvation number S_{N}. While the alteration in surface tension does partially counteract these effects, it is insufficient to fully offset them. Consequently, a temperature shift of 20 K within the considered range results in a five to sixfold alteration of the starvation number.
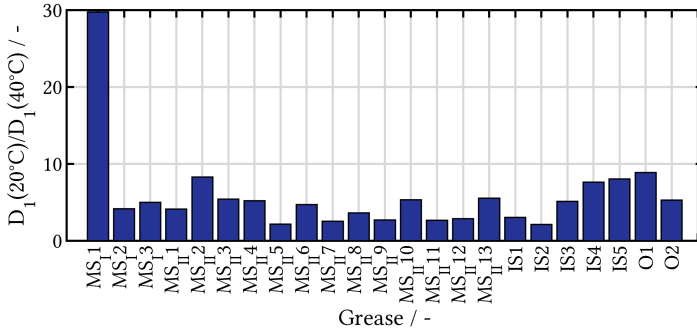
Figure 7.12.: Relative change of term D_1 for all tested greases due to a temperature decrease of $\Delta\vartheta = 20\,\mathrm{K}$.

Although the influence of temperature was not experimentally explored within this study, it is reasonable to assume that elevated temperatures substantially reduce the range of operating conditions that are prone to wear. Conversely, lower temperatures can be particularly detrimental to the performance of oscillating bearings in terms of wear and lubrication-related effects.

8.   Conclusion & Outlook

The present study has demonstrated that under oscillating motion with amplitude ratios of $\frac{x}{2b} > 1$, significant damage can occur on the raceway of rolling bearings within a short period of time. Whether damage occurs depends on the operating and the lubricant parameters. Crucial operational parameters include the oscillation frequency and amplitude. Based on the test results, it can be inferred that higher oscillation frequencies are particularly detrimental, as they reduce the time for reflow of base oil and may result in severe lubricant starvation. Concerning the oscillation amplitude, four distinct regions can be identified, three of which fall within the considered parameter range of amplitude ratios of $\frac{x}{2b} > 1$. Thereby, very small amplitude ratios are rather harmless, which can be attributed to the fact that only a small track is formed, which can easily be supplied by a small amount of base oil. As the oscillation amplitude increases, the operating conditions become progressively critical until reaching an angle denoted as θ_{sw}. This angle can be calculated based on the bearing's kinematics and cage geometry, representing half of the critical angle, i.e., $\theta_{sw} = \frac{\theta_c}{2}$. Further enlargement of the oscillation angle leads to less critical conditions with respect to wear initiation, which is attributed to an additional re-lubrication mechanism resulting from the interaction of the rolling element, the cage and the surrounding grease reservoirs. This study provides empirical evidence supporting the hypotheses of re-lubrication via base oil reflow and cage interaction. Consequently, the study proposes the utilization of a starvation number S_N to evaluate the risk of premature damage due to starvation in oscillating bearings, taking into account operational and lubricant parameters, as well as contact geometry and cage characteristics. The starvation model has been validated through numerous component tests, displaying its efficacy in predicting the occurrence of starvation for the specific bearing type under investigation. Future research will focus on assessing the scalability of the starvation model to different bearing sizes and its applicability to other bearing types. Successful attempts have already been

made to apply the model to different bearing sizes, as well as to cylindrical roller bearings [9].

Bibliography

[1] Svenska Kullagerfabriken (SKF). *SKF rolling bearings catalogue*. 2008.

[2] A. Akchurin, D. van den Ende, and P. M. Lugt. "Modeling impact of grease mechanical ageing on bleed and permeability in rolling bearings". In: *Tribology International* 170 (2022), p. 107507.

[3] J. O. Almen. "Lubricants and false brinelling of ball and roller bearings". In: *Mechanical Engineering* 59.6 (1937), pp. 415–422.

[4] American Society for Testing and Materials. *ASTM D1403 : Standard Test Methods for Cone Penetration of Lubricating Grease Using One-Quarter and One-Half Scale Cone Equipment*. 2020. DOI: 10.1520/D1403-20B.

[5] American Society for Testing and Materials. *ASTM D217 : Standard Test Methods for Cone Penetration of Lubricating Grease*. 2021. DOI: 10.1520/D0217-21A.

[6] American Society for Testing and Materials. *ASTM D4170 : 2016 - Standard Test Method for Fretting Wear Protection by Lubricating Greases*. 2016. DOI: 10.1520/D4170-16.

[7] American Society for Testing and Materials. *ASTM D445 : Standard Test Method for Kinematic Viscosity of Transparent and Opaque Liquids (and Calculation of Dynamic Viscosity)*. 2022. DOI: 10.1520/D0445-21E02.

[8] H. Baly. "Reibung fettgeschmierter Wälzlager". PhD thesis. University Hanover, 2005.

[9] G. Bayer et al. "Experimental Investigations on Wear in Oscillating Grease-Lubricated Rolling Element Bearings of Different Size and Type". In: *Lubricants* 11.3 (2023), p. 120.

[10] E. E. Bisson and W. J. Anderson. *Advanced bearing technology*. Vol. 38. National Aeronautics and Space Administration, Washington, D. C., 1964.

[11]   J. J. Bohner and P. L. Conley. "On the torque and wear behavior of selected thin film MOS2 lubricated gimbal bearings". In: *NASA. Langley Research Center, The 22nd Aerospace Mechanisms Symposium.* 1988.

[12]   Ervin A Bossanyi. "Individual blade pitch control for load reduction". In: *Wind Energy: An International Journal for Progress and Applications in Wind Power Conversion Technology* 6.2 (2003), pp. 119–128.

[13]   J. Brändlein. *Die Wälzlagerpraxis. Handbuch für die Berechnung und Gestaltung von Lagerungen.* Vereinigte Fachverlage, Mainz, Germany, 1995.

[14]   D. E. Brewe and B. J. Hamrock. "Simplified solution for elliptical-contact deformation between two elastic solids". In: *Journal of Lubrication Technology* 99(4) (1977), pp. 485–487.

[15]   P. M. Cann. "Grease lubrication of rolling element bearings—role of the grease thickener". In: *Lubrication Science* 19.3 (2007), pp. 183–196.

[16]   P. M. Cann, B. Damiens, and A. A. Lubrecht. "The transition between fully flooded and starved regimes in EHL". In: *Tribology International* 37.10 (2004), pp. 859–864.

[17]   P. M. Cann et al. "Grease degradation in R0F bearing tests". In: *Tribology Transactions* 50.2 (2007), pp. 187–197.

[18]   P. M. Cann et al. "Grease degradation in rolling element bearings". In: *Tribology Transactions* 44.3 (2001), pp. 399–404.

[19]   H. Cen and P. M. Lugt. "Effect of start-stop motion on contact replenishment in a grease lubricated deep groove ball bearing". In: *Tribology international* 157 (2021), p. 106882.

[20]   H. Cen and P. M. Lugt. "Film thickness in a grease lubricated ball bearing". In: *Tribology international* 134 (2019), pp. 26–35.

[21]   H. Cen and P. M. Lugt. "Replenishment of the EHL contacts in a grease lubricated ball bearing". In: *Tribology international* 146 (2020), p. 106064.

[22]   F. Chevalier et al. "Starvation phenomena in EHL point contacts: Influence of inlet flow distribution." In: *Tribology Series* 31 (1996), pp. 213–223.

[23]   Y. P. Chiu. "An analysis and prediction of lubricant film starvation in rolling contact systems". In: *ASLE transactions* 17.1 (1974), pp. 22–35.

[24] P. Dahl. *A solid friction model*. Tech. rep. The Aerospace Corporation, California, USA, 1968.

[25] B. Damiens, A. A. Lubrecht, and P. M. Cann. "Influence of cage clearance on bearing lubrication". In: *Tribology Transactions* 47.1 (2004), pp. 2–6.

[26] A. M. Ertel. "Hydrodynamic lubrication based on new principles". In: *Akad. Nauk SSSR Prikadnaya Mathematica i Mekhanika* 3.2 (1939), pp. 41–52.

[27] S. Fouvry et al. "An energy description of wear mechanisms and its applications to oscillating sliding contacts". In: *Wear* 255.1-6 (2003), pp. 287–298.

[28] Normalisation Francaise. *NFT 60-199 - Aptitude à résister au faux effet Brinell*. 1995.

[29] German Institute for Standardization. *DIN 51563 : 2011-04 - Testing of Mineral Oils and Related Materials - Determination of Viscosity Temperature Relation - Slope m*. 2011.

[30] German Institute for Standardization. *DIN 51825 : 2004-06 - Lubricants - Lubricating greases K - Classification and requirements*. 2004.

[31] L. Gershuni, M. G. Larson, and P. M. Lugt. "Lubricant replenishment in rolling bearing contacts". In: *Tribology Transactions* 51.5 (2008), pp. 643–651.

[32] J. Gerstenberger and G. Poll. "Rolling bearing lubrication with grease at low temperatures". In: *Tribology Series*. Vol. 39. Elsevier, 2001, pp. 303–312.

[33] D. Godfrey. "Fretting Corrosion or False Brinelling?" In: *Tribology & Lubrication Technology* 59.12 (2003), pp. 28–29.

[34] D. Godfrey. *Investigation of fretting corrosion by microscopic observation*. Tech. rep. 2039. National Advisory Committee for Aeronautics, 1950.

[35] R. Gohar. *Elastohydrodynamics*. Ellis Horwood, Ltd., 1988.

[36] M. Grebe. "False Brinelling - Standstill marks at roller bearings". PhD thesis. Bratislava: Slovak University of Technology, 2012.

[37] A. N. Grubin. "Fundamentals of the hydrodynamic theory of lubrication of heavily loaded cylindrical surfaces". In: *Investigation of the Contact Machine Componets* 2 (1949).

[38]   F. Guo and P. L. Wong. "A multi-beam intensity-based approach for lubricant film measurements in non-conformal contacts". In: *Proceedings of the Institution of Mechanical Engineers, Part J: Journal of Engineering Tribology* 216.5 (2002), pp. 281–291.

[39]   B. J. Hamrock. *Fundamentals of fluid lubrication.* Vol. 2. National Aeronautics and Space Administration, Washington, D. C., 1991.

[40]   B. J. Hamrock and D. Dowson. *Ball bearing lubrication: the elastohydrodynamics of elliptical contacts.* John Wiley & Sons, 1981.

[41]   B. J. Hamrock and D. Dowson. "Elastohydrodynamic lubrication of elliptical contacts for materials of low elastic modulus I—fully flooded conjunction". In: *Journal of Lubrication Technology* 100(2) (1978), pp. 236–245.

[42]   B. J. Hamrock and D. Dowson. "Isothermal elastohydrodynamic lubrication of point contacts: Part 1—Theoretical formulation". In: *Journal of Lubrication Technology* 98(2) (1976), pp. 223–228.

[43]   B. J. Hamrock and D. Dowson. "Isothermal elastohydrodynamic lubrication of point contacts: Part IV—starvation results". In: *Journal of Lubrication Technology* 99(1) (1977), pp. 15–23.

[44]   B. J. Hamrock and D. Dowson. *Minimum film thickness in elliptical contacts for different regimes of fluid-film lubrication.* Tech. rep. NASA Lewis Research Center Cleveland, OH, USA, 1978.

[45]   T. Harris, J. H. Rumbarger, and C. P. Butterfield. *Wind turbine design guideline DG03: yaw and pitch rolling bearing life.* Tech. rep. National Renewable Energy Lab. (NREL), Golden, CO, USA, 2009.

[46]   T. A. Harris and M. N. Kotzalas. *Rolling bearing analysis—essential concepts of bearing technology.* Taylor and Francis, 2007.

[47]   H. L. Heathcote. "The ball bearing: in the making, under test and on service". In: *Proceedings of the Institution of Automobile Engineers* 15.1 (1920), pp. 569–702.

[48]   E. Herbek and R. Strohecker. "Effect of Lubricants in Minimizing Fretting Corrosion". In: *Symposium on Fretting Corrosion.* ASTM International. 1952.

[49]   H. Hertz. "Ueber die Berührung fester elastischer Körper." In: *Journal für die reine und angewandte Mathematik* 92 (1882), pp. 156–171.

[50] L. Houpert. "Bearing life calculation in oscillatory applications". In: *Tribology transactions* 42.1 (1999), pp. 136–143.

[51] J. Hutton. *NLGI lubricating grease guide*. 1987.

[52] J. Hwang and G. Poll. "A new approach for the prediction of fatigue life in rolling bearings based on damage accumulation theory considering residual stresses". In: *Frontiers in Manufacturing Technology* 2 (2022).

[53] B. Jacod et al. "An analysis of track replenishment mechanisms in the starved regime". In: 36 (1999), pp. 483–492.

[54] E. M. Johnson. *The Effect of Lubrication on Fretting Corrosion*. Tech. rep. Technical Report 540031. SAE International, 1954.

[55] K. Johnson. "Regimes of elastohydrodynamic lubrication". In: *Journal of Mechanical Engineering Science* 12.1 (1970), pp. 9–16.

[56] K. L. Johnson. *Contact mechanics*. Cambridge university press, 1985.

[57] A. B. Jones. *The Mathematical Theory of Rolling-Element Bearings*. MCGraw-Hill, New York, 1956.

[58] M. Kalisch et al. *Das logistische Regressionsmodell*. Springer Spektrum, Wiesbaden, 2021, pp. 13–29.

[59] M. Kato and T. Sato. "The development of low friction and anti-fretting corrosion greases for CVJ and wheel bearing applications". In: *SAE Transactions* (1987), pp. 1244–1250.

[60] S. Kien et al. "Influences of Lubricants and Surface Topographies on Marangoni Phenomena". In: *Technische Akademi Esslingen International Tribology Colloquium Proceedings*. Vol. 16. 2008.

[61] T. Kita and Y. Yamamoto. "Fretting wear performance of lithium 12-hydroxystearate greases for thrust ball bearing in reciprocation motion". In: *Japanese Journal of Tribology* 42.6 (1997), pp. 782–783.

[62] Klueber Lubrication München KG. *Das Geheimnis des Rundlaufs: Tipps und Tricks zur Schmierung von Wälzlagern*. 2011.

[63] S. Komatsuzakl, T. Uematsu, and Y. Kobayashl. "Change of grease characteristics to the end of lubricating life". In: *NLGI spokesman* 63.12 (2000), pp. 22–29.

[64] J. Kuhlmann. "Tribology of bearing lubrication greases under steady low temperature conditions". PhD thesis. Leibniz University Hanover, 2009.

[65] E. Larsson et al. "Unraveling the lubrication mechanisms of lithium complex (LiX)-and polypropylene (PP)-thickened greases in fretting–Part I: Fretting experiments and surface analysis". In: *Wear* 490 (2022), p. 204192.

[66] E. Larsson et al. "Unraveling the lubrication mechanisms of lithium complex (LiX)-and polypropylene (PP)-thickened greases in fretting–Part II: Lubrication model". In: *Wear* 506 (2022), p. 204470.

[67] E. Laukotka and D. Arnold. *FVA-Heft 660 Referenzölkatalog Abschlussbericht.* Tech. rep. Forschungsvereinigung Antriebstechnik eV, 2007.

[68] J. R. Lince. "Effective Application of Solid Lubricants in Spacecraft Mechanisms". In: *Lubricants* 8.7 (2020), p. 74.

[69] H. C. Liu et al. "A dichromatic interference intensity modulation approach to measurement of lubricating film thickness". In: *Tribology Letters* 58.1 (2015), pp. 1–11.

[70] S. H. Loewenthal. "Two Gimbal Bearing Case Studies: Lessons Learned". In: *Proceedings of the 22nd Aerospace Mechanisms Symposium, NASA. Langley Research Center* (1988).

[71] A. A. Lubrecht. "The Numerical Solution of the Elastohydrodynamically Lubricated Line-and Point Contact Problem Using Multigrid Techniqes". PhD thesis. Luleå tekniska universitet, 1987.

[72] P. M. Lugt. "A review on grease lubrication in rolling bearings". In: *Tribology Transactions* 52.4 (2009), pp. 470–480.

[73] P. M. Lugt. *Grease lubrication in rolling bearings.* John Wiley & Sons, 2012.

[74] P. M. Lugt and G. E. Morales-Espejel. "A review of elasto-hydrodynamic lubrication theory". In: *Tribology transactions* 54.3 (2011), pp. 470–496.

[75] T. Maruyama and T. Saitoh. "Oil film behavior under minute vibrating conditions in EHL point contacts". In: *Tribology International* 43.8 (2010), pp. 1279–1286.

[76] T. Maruyama, T. Saitou, and A. Yokouchi. "Differences in Mechanisms for Fretting Wear Reduction between Oil and Grease Lubrication". In: *Tribology Transactions* 60.3 (2016), pp. 497–505.

[77] O. Menck. "The Finite Segment Method A numerical rolling contact fatigue life model for bearings subjected to stochastic operating conditions". In: *Journal of Tribology* (2022), pp. 1–11.

[78] J. S. Mérieux et al. "Shear-degradation of grease and base oil availability in starved EHL lubrication". In: 38 (2000), pp. 581–588.

[79] R. D. Mindlin. "Compliance of Elastic Bodies in Contact". In: *Journal of Applied Mechanics* (1949), pp. 259–268.

[80] G. E. Morales-Espejel et al. "Film thickness in grease lubricated slow rotating rolling bearings". In: *Tribology International* 74 (2014), pp. 7–19.

[81] H. T. Morton. "Friction Oxidation". In: *Scientific Paper of the Fafnir Bearing Co., New Britain* (1946).

[82] D. N. Olaru and M. D. Gafitanu. "Starvation in ball bearings". In: *Wear* 170.2 (1993), pp. 219–234.

[83] N. Pandis. "The chi-square test". In: *American journal of orthodontics and dentofacial orthopedics* 150.5 (2016), pp. 898–899.

[84] F. Pape and G. Poll. "Investigations on graphene platelets as dry lubricant and as grease additive for sliding contacts and rolling bearing application". In: *Lubricants* 8.1 (2020), p. 3.

[85] M. Pasdari and C. R. Gentle. "Effect of lubricant starvation on the minimum load condition in a thrust-loaded ball bearing". In: *ASLE transactions* 30.3 (1987), pp. 355–359.

[86] M. Phaner-Goutorbe et al. "Scanning tunneling microscopy study of wear induced by false brinelling on rolling bearings". In: *Applied Surface Science* 1008 (1997), pp. 45–51.

[87] D. D. Phinney, C. L. Pollard, and J. T. Hinricks. "Experience with duplex bearings in narrow angle oscillating applications". In: *Proceedings of the 22nd aerospace mechanisms symposium*. 1988, pp. 211–216.

[88] H. Pittroff. "Riffelbildung bei Wälzlagern infolge Stillstandserschütterungen: (Der Einfluss fremderregter Schwingungen auf stillstehende Wälzlager)." PhD thesis. Technische Hochschule München, 1961.

[89] Román de la Presilla, Johan Leckner, and Sergei Glavatskih. "Grease lubricity in the fretting contact: Are ionic liquids the solution?" In: *Tribology International* 185 (2023), p. 108509.

[90] Román de la Presilla et al. "Oscillating rolling element bearings: A review of tribotesting and analysis approaches". In: *Tribology International* (2023), p. 108805.

[91]   Ladislao Reti. "Leonardo on bearings and gears". In: *Scientific American* 224.2 (1971), pp. 100–111.

[92]   O. Reynolds. "IV. On the theory of lubrication and its application to Mr. Beauchamp tower's experiments, including an experimental determination of the viscosity of olive oil". In: *Philosophical transactions of the Royal Society of London* 177 (1886), pp. 157–234.

[93]   T. G. Roehner and E. L. Armstrong. "Fretting Corrosion Studies with a Modified Fafnir Machine". In: *a meeting of the National Lubricating Grease Institute, Chicago*. Vol. 111. 1952, pp. 29–31.

[94]   A. Saatchi. "The Effect of Grease Composition on Fretting Wear". PhD thesis. University of Akron, 2019.

[95]   K. R. Sathwik Chatra and P. M. Lugt. "The process of churning in a grease lubricated rolling bearing: Channeling and clearing". In: *Tribology international* 153 (2021), p. 106661.

[96]   C. Schadow. "Stillstehende fettgeschmierte Wälzlager unter dynamischer Beanspruchung". PhD thesis. Otto von Guericke University, Magdeburg, Germany, 2016.

[97]   C. Schadow and L. Deters. "Abschlussbericht Forschungsvorhaben Nr. 540 II: Stillstehende fettgeschmierte Wälzlager unter dynamischer Belastung". In: *FVA-Forschungsheft 1268, 2018, Arbeitskreis Schmierstoffe und Tribologie* 1268 (2018), p. 145.

[98]   H. Schmidt and J. Schwartz. "Energy-Efficient Minimal Quantity Lubrication for High-Speed Spindles". In: *SKF-Evolution* (2014).

[99]   F. Schwack, F. Prigge, and G. Poll. "Finite element simulation and experimental analysis of false brinelling and fretting corrosion". In: *Tribology International* 126 (2018), pp. 352–362.

[100]   Fabian Schwack. "Investigations Regarding the Operating Performance of Oscillating Bearings using the Example of Wind Turbine Pitch Bearings". PhD thesis. Leibniz University Hanover, 2020.

[101]   T. W. Selby. "The non-Newtonian characteristics of lubricating oils". In: *ASLE transactions* 1.1 (1958), pp. 68–81.

[102]   U. Sielaff. *Dynamic analysis of a crank-rocker mechanism*. Tech. rep. Kansas State University, 1966.

[103]   M. A. C. de Sousa Marques et al. "Heat capacity, density, surface tension, and contact angle for polyalphaolefins and ester lubricants". In: *Thermochimica Acta* 703 (2021), p. 178994.

[104]   T. Steinert. "Das Reibmoment von Kugellagern mit bordgeführtem Käfig, Diss". PhD thesis. RWTH Aachen University, 1995.

[105]   J. Sugimura, W. R. Jones, and H. A. Spikes. "EHD film thickness in non-steady state contacts". In: *Journal of Tribology* 120(3) (1998), pp. 442–452.

[106]   The Institute of Petroleum. *IP 121: Determination of oil separation from lubricating grease - Pressure filtration method.* 2000.

[107]   M. J. Todd and K. L. Johnson. "A model for coulomb torque hysteresis in ball bearings". In: *International journal of mechanical sciences* 29.5 (1987), pp. 339–354.

[108]   G. A. Tomlinson. "The rusting of steel surfaces in contact". In: *Proceedings of the Royal Society of London. Series A, Containing Papers of a Mathematical and Physical Character* (1927), pp. 472–483.

[109]   O. Vingsbo and S. Söderberg. "On fretting maps". In: *Wear* 126.2 (1988), pp. 131–147.

[110]   S. Wandel et al. "Starvation and Re-lubrication in Oscillating Bearings: Influence of Grease Parameters". In: *Tribology Letters* 70.4 (2022), pp. 1–14.

[111]   S. Wandel et al. "Starvation and relubrication mechanisms in grease lubricated oscillating bearings". In: *Tribology International* 165 (2022), p. 107276.

[112]   S. Wandel et al. "Wear Development in Oscillating Rolling Element Bearings". In: *Lubricants* 11.3 (2023), p. 117.

[113]   E. W. Washburn. "The dynamics of capillary flow". In: *Physical review* 17.3 (1921), p. 273.

[114]   L. D. Wedeven, D. Evans, and A. Cameron. "Optical analysis of ball bearing starvation". In: *Jounral of Lubrication Technology* 93(3) (1971), pp. 349–361.

[115]   V. Wikström. "Rolling bearing lubrication at low temperature". PhD thesis. Luleå tekniska universitet, 1996.

[116]   V. Wikström and B. Jacobson. "Loss of lubricant from oil-lubricated near-starved spherical roller bearings". In: *Proceedings of the Institution of Mechanical Engineers, Part J: Journal of Engineering Tribology* 211.1 (1997), pp. 51–66.

[117]   W. Winn. *Introduction to Understandable Physics: Modern and Frontier Physics*. AuthorHouse, 2010.

[118]   K. H. Wright. "An investigation of fretting corrosion". In: *Proceedings of the Institution of Mechanical Engineers* 167.1b (1953), pp. 556–574.

[119]   A. Yano et al. "Evaluation of fretting protection property of lubricating grease applied to thrust ball bearing-Comparison between ASTM D4170 test and impact fretting test". In: *Tribology Online* 5.1 (2010), pp. 52–59.

A. Publications

A.1. Journal Papers

- Schwack, F., Schneider, V., Wandel, S., de la Presilla, R. J., Poll, G., & Glavatskih, S. (2021). On the critical amplitude in oscillating rolling element bearings. Tribology International, 163, 107154.

- Wandel, S., Bader, N., Schwack, F., Glodowski, J., Lehnhardt, B., & Poll, G. (2022). Starvation and relubrication mechanisms in grease lubricated oscillating bearings. Tribology International, 165, 107276.

- Wandel, S., Bader, N., Glodowski, J., Lehnhardt, B., Leckner, J., Schwack, F., & Poll, G. (2022). Starvation and Re-lubrication in Oscillating Bearings: Influence of Grease Parameters. Tribology Letters, 70(4), 114.

- Wandel, S., Bartschat, A., Glodowski, J., Bader, N., & Poll, G. (2023). Wear Development in Oscillating Rolling Element Bearings. Lubricants, 11(3), 117.

- Bayer, G., Bartschat, A., Wandel, S., Baust, S., & Poll, G. (2023). Experimental Investigations on Wear in Oscillating Grease-Lubricated Rolling Element Bearings of Different Size and Type. Lubricants, 11(3), 120.

- Presilla, R., Wandel, S., Stammler, M., Grebe, M., Poll, G., Glavatskih, S. (2023). Oscillating Rolling Element Bearings: A Review of Tribotesting and Analysis Approaches. Tribology International, 108805.

A.2. Presentations

- Wandel, S., Schwack, F. & Poll, G. (2019). Oszillierende Wälzlager in Windenergieanlagen - Abgrenzung der Schadensmechanismen. 13. VDI-Fachtagung Gleit- und Wälzlagerungen, June 05-06, Schweinfurt (Germany).

- Wandel, S., Bartschat, A. & Poll, G. (2021). Wear Development due to Oscillating Movement Operating Conditions as Employed in Rotor Blade Bearings in Wind Turbines. Virtual Annual Meeting & Exhibition (STLE 2021), May 17-20, Virtual

- Wandel, S., Schönemeier, P., Kelley, J., Hwang, J. & Poll, G. (2021). Starvation in Oscillating Bearings Using the Example of Rotor Blade Bearings. Wind Energy Science Conference 2021 (WESC 2021), May 25-28, Hannover (Germany)

- Wandel, S., Bartling, F. & Poll, G. (2022). The Role of the cage for Track Replenishment in Oscillating Rolling Element Bearings. STLE 76th Annual Meeting, May 15-19, Orlando, Florida (USA).

- Wandel, S., Bartling, F. & Poll, G. (2022). The Role of the cage for Track Replenishment in Oscillating Rolling Element Bearings. 17. Arnold Tross Kolloquium, June 10, Hamburg (Germany).

- Wandel, S., Bayer, G. & Poll, G. (2023). Starvation and Wear Prediction in Rotor Blade Bearings. Wind Trubine Bearings, June 20-22, Bremen (Germany).

- Wandel, S., Lehnhardt, B., Bayer, G. & Poll, G. (2023). Wear Prevention in Rotor Blade Bearings. NAWEA/WindTech, October 30 - November 1, Denver, Colorado (USA).

A.3. Conference Papers

- Wandel, S., Schwack, F., & Poll, G. (2019) Oszillierende Wälzlager in Windenergieanlagen - Abgrenzung der Schadensmechanismen. 13. VDI-Fachtagung Gleit- und Wälzlagerungen 2019, p.221-232, Schweinfurt, Germany

A.4. Posters

- Wandel, S. et al. (2019) Highly Loaded Slewing Bearings. Conference for Wind Power Drives, CWD 2019, Aachen (Germany)

B. Student Work

- Schwarz, N. (2019). Oszillierende Wälzlager in Windenergieanlagen - Abgrenzung der Schadensmechanismen. Leibniz University Hannover, Student research project.

- Reinhardt, A. (2019). Entwicklung, Auslegung und Konstruktion eines Prüfkopfes zur Untersuchung von Wälzlagern unter skalierten Betriebsbedingungen von Windenergieanlagen. Leibniz University Hannover, Bachelor thesis.

- Koc, S. (2020). Beurteilung von Fetten für die Anwendung in Rotorblattlagern von Windenergieanlagen. Leibniz University Hannover, Bachelor thesis.

- Glodowski, J. (2020). Experimentelle Untersuchungen und Analysemethoden zum Verschleißverhalten von Rotorblattlagern. Leibniz University Hannover, Student research project.

- Lehnhardt, B. (2020). Einfluss der Betriebsparameter auf das Verschleißverhalten oszillierender Wälzlager. Leibniz University Hannover, Student research project.

- Glodowski, J. (2021). Einfluss von Schmierfettparametern auf das Verschleißverhalten oszillierender Wälzlager. Leibniz University Hannover, Master thesis.

- Bartling, F. (2021). Einfluss von Schmierzyklen auf das Verschleißverhalten oszillierender Wälzlager. Leibniz University Hannover, Student research project.

- Amdouni, M., A. (2021). Mangelschmierung eines fettgeschmierten, oszillierenden Wälzkontaktes im Modellversuch. Leibniz University Hannover, Bachelor thesis.

- Luo, B. (2021). Einfluss von Einlauf- und Fettalterungsprozessen auf das Verschleißverhalten oszillierender Wälzlager. Leibniz University Hannover, Master thesis.

- Lehnhardt, B. (2022). Untersuchungen zur Mangelschmierung oszillierender Wälzkontakte. Leibniz University Hannover, Master thesis.

- Bartling. F. (2022). Entwicklung eines Wälzlagerkäfigs mit integriertem Nachschmiersystem für die Anwendung in oszillierenden Wälzlagern. Leibniz University Hannover, Master thesis.

- Zhuoyu, L. (2022). Einfluss von Schmierfettparametern speziell angefertigter Modellfette auf das Verschleißverhalten oszillierender Wälzlager. Leibniz University Hannover, Student research project.

- Qiongdan, H. (2022). Validierung eines FE-Modells zur Berechnung der Reibenergie im oszillierenden Wälzkontakt. Leibniz University Hannover, Master thesis.

- Amdouni, M., A. (2022). Einfluss des Käfigs auf die Rückschmiernug eines Wälzkontaktes im Modellversuch. Leibniz University Hannover, Student research project.

C.   Curriculum Vitae

Sebastian Wandel
Born 20th November 1992 in Nürtingen, Germany.

Career path

09/2018-Today	Research Assistant Leibniz University Hannover
06/2016-03/2018	Student Assistant Steinbeis Transferzentrum Tribologie
11/2014-07/2015	Intern/ Bachelors Volkswagen Group
07/2011-09/2011	Intern Zahoransky AG

Education

10/2016-07/2018	Master of Science, Mechanical Engineering Karlsruhe Institute of Technology, Germany
10/2011-07/2016	Bachelor of Science, Mechanical Engineering Karlsruhe Institute of Technology, Germany
09/2003-07/2011	General Matriculation Standard (Allgemeine Hochschulreife) Marie-Curie-Gymnasium Kirchzarten, Germany